Monthly Notices of the ROYAL ASTRONOMICAL SOCIETY

MNRAS **539,** 501–541 (2025) https://doi.org/10.1093/mnras/staf424
Advance Access publication 2025 March 13

Flares in the changing look AGN Mrk 590 – II. Deep X-ray observations reveal a Comptonizing inner accretion flow

D. Lawther [1]★ M. Vestergaard,[1,2] S. Raimundo [2,3] X. Fan[1] and J. Y. Koay[4,5]

[1]*Steward Observatory, University of Arizona, 933 N. Cherry Avenue, 85721 Tucson, AZ, USA*
[2]*DARK, Niels Bohr Institute, University of Copenhagen,Blegdamsvej 17, 2100 Copenhagen,Denmark*
[3]*University of Southampton, University Road, SO17 1BJ Southampton, UK*
[4]*Graduate School of Science and Technology, Niigata University , 8050 Ikarashi-nino-cho, Nishi-ku, Niigata 950-2181, Japan*
[5]*Institute of Astronomy and Astrophysics, Academia Sinica, Roosevelt Road, Taipei 10617, Taiwan R.O.C.*

Accepted 2025 March 11. Received 2025 March 7; in original form 2024 October 17

ABSTRACT

Mrk 590 is a changing look active galactic nucleus (AGN) currently in an unusual repeat X-ray and UV flaring state. Here, we report on deep X-ray observations with *XMM–Newton*, *NuSTAR*, and *NICER*, obtained at a range of X-ray flux levels. We detect a prominent soft excess below 2 keV; its flux is tightly correlated with that of both the X-ray and UV continuum, and it persists at the lowest flux levels captured. Our Bayesian model comparison strongly favours inverse Comptonization as the origin of this soft excess, instead of blurred reflection. We find only weak reflection features, with $R \lesssim 0.4$ assuming Compton-thick reflection. Most of this reprocessing occurs at least ∼800 gravitational radii (roughly three light-days) from the continuum source. Relativistically broadened emission is weak or absent, suggesting the lack of a standard 'thin disc' at small radii. We confirm that the predicted broad-band emission due to Comptonization is roughly consistent with the observed UV–optical photometry. This implies an optically thick, warm ($kT_e \sim 0.3$ keV) scattering region that extends to at least $\sim 10^3$ gravitational radii, reprocessing any UV thermal emission. The lack of a standard 'thin disc' may also explain the puzzling ∼ 3-d X-ray to UV delay previously measured for Mrk 590. Overall, we find that the X-ray spectral changes in Mrk 590 are minimal, despite substantial luminosity changes. Other well-studied changing look AGN display more dramatic spectral evolution, e.g. disappearing continuum or soft excess. This suggests that a diversity of physical mechanisms in the inner accretion flow may produce a UV–optical changing-look event.

Key words: galaxies: active – galaxies: Seyfert – accretion, accretion discs.

1 INTRODUCTION

Active galactic nuclei (AGN) emit copiously over the entire electromagnetic spectrum (e.g. Sanders et al. 1989; Elvis et al. 1994; Richards et al. 2006). They are powered by the release of gravitational energy as gas from their host galaxy forms an accretion flow and feeds the central supermassive black hole (e.g. Shields 1978; Malkan & Sargent 1982; Malkan 1983; Storchi-Bergmann & Schnorr-Müller 2019). The standard theory of accretion on to black holes is presented in the seminal works of Shakura & Sunyaev (1973) and Novikov & Thorne (1973), hereafter referred to as 'thin-disc models'. The observed UV–optical AGN continuum ('big blue bump', e.g. Shields 1978; Malkan & Sargent 1982; Sanders et al. 1989; Siemiginowska et al. 1995; Grupe et al. 1998; Scott & Stewart 2014) is often attributed to emission from a thermal disc. However, the applicability of thin-disc models to AGN is debated, as they fail to predict the observed variability time-scales and spectral turnovers (Antonucci 2015; Lawrence 2018).

Typically, AGN display stochastic UV–optical flux variations of order ∼ 10 per cent on rest-frame time-scales of days to months (e.g. Vanden Berk et al. 2004; Kelly, Bechtold & Siemiginowska 2009; Rumbaugh et al. 2018; Chanchaiworawit & Sarajedini 2024). This level of variability may be due to thermal instabilities in the disc (e.g. Kelly et al. 2009), plus a high-frequency contribution from reprocessing of intrinsic X-ray variability (the 'lamp-post model', e.g. Cackett, Horne & Winkler 2007; Edelson et al. 2019; Guo, Barth & Wang 2022). In recent years, a class of changing look AGN (CLAGN) has been identified, displaying more extreme variability behaviour. In CLAGN, the UV–optical continuum and broad emission lines (dis)appear on time-scales of months to years (e.g. Penston & Perez 1984; Denney et al. 2014; Shappee et al. 2014; LaMassa et al. 2015; MacLeod et al. 2016; Runnoe et al. 2016; LaMassa, Yaqoob & Kilgard 2017; Rumbaugh et al. 2018; MacLeod et al. 2019). In broad terms, this behaviour may be due to variable *obscuration* of the central engine, or to strong variability of the ionizing continuum. Ricci & Trakhtenbrot (2023) classify these types as *changing-obscuration* and *changing-state* AGN, respectively. Analytical thin-disc models predict significant continuum variability on long time-scales, $\sim 10^3$–10^5 yr (e.g. LaMassa et al. 2015; MacLeod

★ E-mail: unclellama@gmail.com

et al. 2016; Lawrence 2018; Noda & Done 2018), inconsistent with the changing-state sources. Some numerical simulations of accretion discs may capture additional variability mechanisms; Jiang et al. (2018) and Jiang & Blaes (2020) find strong variability on time-scales of a few years, consistent with observations. Alternatively, the accretion state of the disc may transition out of the 'thin-disc' mode and into a radiatively inefficient, advective state (e.g. Narayan & Yi 1994; Yuan & Narayan 2014), when the Eddington luminosity ratio drops below ~ 1 per cent (e.g. Noda & Done 2018; Veronese et al. 2024). However, the mechanism driving such a state transition (and thus, the predicted time-scale) is largely unknown. Clearly, 'changing-state' CLAGN are important case studies to advance our understanding of AGN accretion.

Many CLAGN display extreme X-ray variability (e.g. Denney et al. 2014; Noda & Done 2018; Ricci et al. 2020; Kollatschny et al. 2023; Lawther et al. 2023; Saha et al. 2023), presumably linked to processes very near the central black hole and inner accretion flow. In this work, to harness the potential of X-ray observations to probe the inner accretion flow, we study a series of deep X-ray observations of the CLAGN Mrk 590 ($z = 0.026385$) obtained since 2002. A *bona fide* AGN in the 1980s–1990s, this target 'turned off' around year 2010 (Denney et al. 2014) and regained its broad emission lines during 2017 (Raimundo et al. 2019). Since then, it displays X-ray and UV–optical flare-ups once or twice a year, during which the X-ray flux increases by a factor of$\sim$ 5–10 for a few weeks. Lawther et al. (2023) (hereafter, Paper 1) find that the X-rays lead the UV variability by ~ 3 d during these flares. This is much longer than the predicted X-ray to UV delay for a 'thin disc' with a central X-ray source. In this work, we further investigate the X-ray emission that drives this flaring activity. Our primary goals are as follows: (1) to document variability in the X-ray emission features, and determine their relationship to continuum variability; (2) to find the most likely physical model of the X-ray emission in Mrk 590, and infer the accretion flow properties based thereon. To provide context for this study, we now briefly outline the typical X-ray emission features in AGN.

Primary continuum: AGN display a power law-like X-ray continuum extending from ~ 0.2 keV or below, with a high-energy cut-off around 200 keV (Zdziarski et al. 1995; Tortosa et al. 2018). The predicted emission from a 'thin disc' does not extend to such high energies. Instead, the X-ray continuum is thought to be due to inverse Compton scattering of UV seed photons in a hot ($kT \sim 100$ keV), optically thin plasma (Sunyaev & Titarchuk 1980; Haardt & Maraschi 1993; Zdziarski et al. 1994, 1995; Zdziarski, Johnson & Magdziarz 1996). The required seed photons may originate in a 'thin disc' or other thermal source in the accretion flow. The size of this region – the so-called hot corona – is constrained to a few gravitational radii, due to its rapid coherent variability (e.g. Guilbert, Fabian & Rees 1983; Barr & Mushotzky 1986; Fabian et al. 2015). The geometry of the hot corona is largely unknown (e.g. Tortosa et al. 2018), although X-ray polarimetry results favour deviations from spherical symmetry (Gianolli et al. 2023; Ingram et al. 2023).

Soft excess: An excess of soft X-rays below rest-frame 2 keV, relative to the primary continuum, is detected in around 80 per cent of low-obscuration AGN, and may be intrinsically near-ubiquitous (Bianchi et al. 2009). The soft excess is not consistent with thermal 'thin disc' emission (e.g. Laor et al. 1997; Leighly 1999; Done et al. 2012). Instead, two production mechanisms are typically considered: (1) the inverse Compton scattering of a thermal distribution of UV seed photons in a warm ($kT \sim 0.2$ keV), optically thick medium (e.g. Czerny & Elvis 1987; Magdziarz et al. 1998; Petrucci et al. 2004; Done et al. 2012; Middei et al. 2020). We refer to this type of soft excess as 'warm-Comptonized emission' throughout. Petrucci et al. (2018) present one possible physical model, where the warm Comptonizing region is a moderately optically thick atmosphere 'sandwiching' a cool disc; the atmosphere is heated by direct dissipation of accretion energy, e.g. via the magnetic dynamo mechanism (Begelman, Armitage & Reynolds 2015). (2) Alternatively, relativistically blurred atomic-line reprocessing ('reflection') can produce a featureless soft excess feature; this mechanism requires a dense accretion flow extending to small radii, such that the individual lines are rotationally blurred out (e.g. Ross & Fabian 2005; Crummy et al. 2006; Walton et al. 2013; Dauser et al. 2014). Thus, in either case, study of the soft excess can probe the nature of the inner accretion flow.

Reflection features: Most AGN display some evidence of iron K-shell emission (Miller 2007; Nandra et al. 2007). These fluorescent lines are due to X-ray illumination of atomic gas. If a 'thin disc' extends to the innermost stable orbit, a relativistically broadened component is expected (e.g. Fabian et al. 1989; Meyer-Hofmeister & Meyer 2011). Broad Fe K is challenging to confirm observationally, but is detected in some local AGN (e.g. Tanaka et al. 1995; Turner et al. 2002; Mason et al. 2003; Porquet & Reeves 2003; Nandra et al. 2007; Bhayani & Nandra 2011). X-ray illumination also produces soft X-ray line emission, along with a broad Compton hump peaking at $\sim$25 keV (e.g. Reynolds 1999; Fabian et al. 2009). Collectively, these are the most prominent features of the so-called reflection spectrum. The full reflection spectrum can be simulated self-consistently, for a given geometry, by several different reflection models (e.g. García et al. 2014; Baloković et al. 2018; Dauser et al. 2022).

Outline of this work In Section 2, we describe the *XMM–Newton*, *NuSTAR*, and *NICER* observations used in this work, along with our basic data-processing procedures. There, we also present *Swift* X-ray light curves to document new flaring activity since June 2021. In Section 3, we describe our analysis of the X-ray data, including a variability study (Section 3.2), and physical modelling in low- and high-flux states (Section 3.3). We discuss our results in Section 4 and conclude in Section 5.

2 OBSERVATIONS AND DATA PROCESSING

2.1 *Swift*

The Neil Gehrels *Swift* Observatory (Burrows et al. 2005) has been monitoring Mrk 590 since 2013 (Paper 1). In this work, we include new *Swift* XRT observations obtained between 2021 June and 2024 September (Swift Cycle 18, Programme 1821134, PI: Lawther; VLBA/Swift Joint Proposal, Programme VLBA/22A-217, PI: Vestergaard; Swift Cycle 19, Programme 1922187, PI: Lawther; VLBA/Swift Joint Proposal, Programme VLBA/24A-374, PI: Vestergaard). These new data are processed and analysed following the same methods as Paper 1; we use version 6.32.1 of the HEASoft pipeline. We present the *Swift* XRT light curve since 2015 June, including the new data collected since 2021, in Fig. 1. Based on the most recent data (Programmes 1 922 187 and VLBA/24A-374), we report that Mrk 590 entered a new, prolonged bright state in Summer 2024, which we will address in future work (Lawther et al. in preparation). Based on the *Swift* monitoring, we obtained several observations with *XMM–Newton* (Section 2.2), *NuSTAR* (Section 2.3), and *NICER* (Section 2.4), aiming to capture the X-ray spectrum

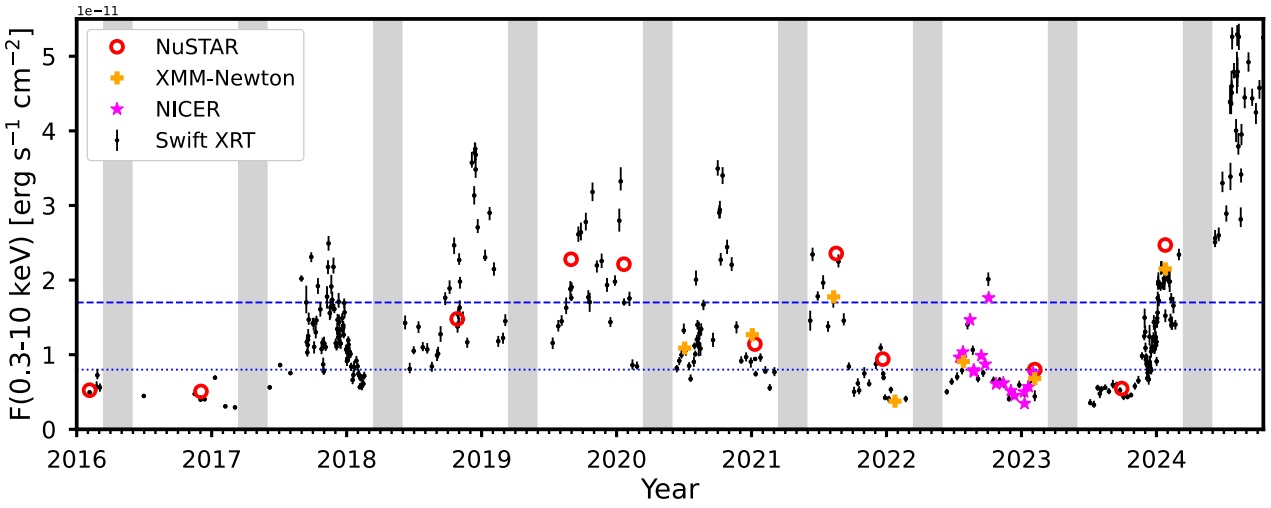

Figure 1. *Swift* XRT 0.3–10 keV light curve (points with error bars) for Mrk 590 since June 2015. Crosses indicate the 0.3–10 keV flux measured with *XMM–Newton*; open circles represent extrapolations of the *NuSTAR* observations (3–79 keV) to the 0.3–10 keV regime. Star symbols indicate *NICER* observations with usable data (Section 2). All fluxes are extracted using a power-law model with Galactic absorption. The dotted and dashed horizontal lines indicate the maximum flux level for inclusion in the 'low state' joint data set, and the minimum for inclusion in the 'high state' (Section 3.3), respectively. Mrk 590 is behind the Sun during early March – mid-June (shaded regions). Data obtained since June 2021 are not included in Paper 1. The prolonged, powerful high-flux state during Summer 2024 will be addressed in future work (Lawther et al. in preparation).

at a range of flux levels. We indicate the observing dates and flux levels of these observations in Fig. 1.

2.2 *XMM–Newton*

2.2.1 Observations

Prior to the discovery of its changing-look behaviour, Mrk 590 was observed by the *XMM–Newton* space telescope (Strüder et al. 2001; Turner et al. 2001) in 2002 (PI: Mason) and 2004 (PI: Santos-Lleo). Thereafter, it was observed during *XMM–Newton* Programmes 86 547 (PI: Miniutti) and 87 084 (PI: Vestergaard), and as part of joint observations during NuSTAR Programme 8233 (PI: Lawther). All observations were performed using the thin optical blocking filter. Fig. 1 illustrates the timing of the observations since 2020, relative to the *Swift* XRT light curve. The individual observation IDs and exposure times are listed in Table 1.

2.2.2 Data processing

XMM–Newton MOS and *pn* data are provided by the Science Archive.[1] We reprocess all *XMM–Newton* data locally using the Science Analysis Software, version 20, by running the *'xmmextractor'* task with its standard parameter settings. This reprocessing ensures that appropriate response matrix files for the source detector location are generated. The observation starting 2021 August 11 was split over two orbits for scheduling reasons; for each instrument (MOS1, MOS2, *pn*) we stack the resulting two spectra using the task *'epicspeccombine'*, and treat them as a single observation. Due to the faintness of the source during our observations, we do not find the high-resolution RGS spectra scientifically useful. We do not need the Optical Monitor data for the analyses described here.

[1]URL: http://nxsa.esac.esa.int/nxsa-web/

2.3 *NuSTAR*

2.3.1 Observations

The *NuSTAR* observatory (Harrison et al. 2013) consists of two identical Wolter X-ray telescopes. The two focal-plane detectors, FPMA and FPMB, are sensitive to energies 3–79 keV. *NuSTAR* observed Mrk 590 during 2016 February as part of the *NuSTAR* Extragalactic Surveys (Harrison et al. 2016). Thereafter, Mrk 590 was observed via a DDT request during 2016, and as part of the following programmes: joint *Swift/NuSTAR* Program 1 417 159 (PI: Vestergaard), *NuSTAR* Cycle 5 Program 5252 (PI: Vestergaard), *NuSTAR* Cycle 6 Programme 6238 (PI: Vestergaard), *NuSTAR* Cycle 7 Programme 7610 (PI: Koss), and *NuSTAR* Cycle 8 Programme 8233 (PI: Lawther). The individual observation IDs and exposure times are listed in Table 1. Fig. 1 indicates the timing of these *NuSTAR* observations relative to the X-ray variability recorded by *Swift*.

2.3.2 Data processing

We process the *NuSTAR* observations using the standard pipeline processing (HEASOFT v. 6.32.1, NUSTARDAS v. 1.9.7). We extract the source and background spectra for each *NuSTAR* detector (FPMA and FPMB) using the *'nuproducts'* task, which also generates appropriate Auxiliary Response Files for the observations. We use a circular source extraction region of radius 60 arcmin centred on the source PSF centroid. For the background extraction, we use a circular region of radius 67 arcmin offset and non-overlapping with the source region, but positioned on the same detector quadrant. We ensure that neither the source nor background extraction regions include the additional soft X-ray source detected in XRT imaging (Paper 1). We use Algorithm 2 of the *'nucalcsaa'* task, with an 'optimized' South Atlantic Anomaly (SAA) cut and including the parameter *'tentacle = yes'*, to filter out the anomalous countrates

Table 1. X-ray observation log, and 0.3–10 keV fluxes.

Telescope	Observation date	Observation ID	Exposure time (s)	$F_{0.3-10}$ (10^{-12} erg cm^{-2} s^{-1})	Joint data set
(1)	(2)	(3)	(4)	(5)	(6)
XMM–Newton	2002-01-01	0109130301	11349	8.6	
	2004-07-04	0201020201	112674	11.3	
	2020-07-04	0865470201	27000	10.8	
	2021-01-03	0865470301	27000	12.6	J21
	2021-08-11	0870840101, 0870840401	17998	18.8	HF
	2022-01-24	0870840201	25800	3.8	LF
	2022-07-28	0912400101	27000	9.3	
	2023-02-06	0870840301	38000	6.8	LF; F23
	2024-01-25	0912400201	27000	21.5	HF
NuSTAR	2016-02-05	60160095002	21205	4.9	LF
	2016-12-02	90201043002	51001	5.0	LF
	2018-10-27	80402610002	21069	14.8	
	2019-08-31	80502630002	68123	21.8	HF
	2020-01-21	80502630004	50168	20.9	HF
	2021-01-10	80502630006	41517	10.9	J21
	2021-08-18	60761012002	18649	22.1	HF
	2021-12-22	80602604002	53311	8.4	
	2023-02-06	80602604004	40977	8.0	F23
	2023-09-29	80802652002	20825	5.5	LF
	2024-01-25	80802652004	62046	24.7	HF
NICER	2022-07-16	5667010401	1743	9.6	
	2022-07-26	5667010501	3371	10.4	
	2022-08-15	5667010702	2052	14.7	
	2022-08-24	5667010801	1015	8.0	
	2022-08-25	5667010802	2043	7.7	
	2022-09-14	5667011001	2636	9.9	
	2022-09-25	5667011101	2522	8.7	
	2022-10-04	5667011201	1786	17.6	
	2022-10-24	5667011401	1917	6.1	
	2022-11-12	5667011601	1815	6.2	
	2022-12-03	5667011801	1505	5.2	
	2023-01-08	5667012101	3498	5.0	

Note. All parameter uncertainties are quoted at the 90th percentile confidence interval. (1) Telescope name. (2) Date of observation start, YYYY-MM-DD. (3) Observation identifier in the *HEASarc* archive. (4) On-source integration time. This is measured before event screening. (5) Integrated 0.3–10 keV model flux, determined using the phenomenological model (Section 3.2). As *NuSTAR* is not sensitive below 3 keV, the best-fitting model is extrapolated, to facilitate comparison with the other telescopes. (6) Data set(s) that this observation is included in for the joint analysis described in Section 3.3.

before and after the SAA passage. This preserves $>$ 95 per cent of the on-source exposure time.

2.4 NICER

2.4.1 Observations

The Neutron star Interior Composition Explorer (NICER; Gendreau et al. 2016) observed Mrk 590 for 27 visits between 2022 June and 2023 February, for typical exposure times of 1.5–2.5 ks per visit (GO Programme 5667, PI: Lawther). We retrieve all observations with durations $>$ 1 ks from the HEAsarc NICER catalogue (Gendreau et al. 2016),[2] resulting in 23 data sets. NICER is a non-imaging telescope, with a variable instrumental background which depends strongly on spacecraft orbital characteristics. The background features of most concern for our study include (1) a low-energy noise peak which can extend beyond $\sim$ 300 eV for observations with high 'optical loading' (i.e. UV-optical stray light causing spurious X-ray events; Fig. 2), and (2) electron precipitation events that can exceed the source signal at $\gtrsim$ 2 keV. We use the SCORPEON background model[3] to evaluate the strength of these background features. Based thereon, we exclude 11 observations from further analysis. The 12 remaining observations are listed in Table 1. We present examples of acceptable and excluded *NICER* observations in Fig. 2.

2.4.2 Data processing

We process the *NICER* spectra using HEASoft v.6.32, which includes updated per-detector filtering for noisy time intervals. We use the *'nicerl2'* tool to extract event files with appropriate good-time intervals. We apply the standard processing settings apart from excluding detectors FPM 14 and 34, which are known to respond strongly to optical loading (e.g. Remillard et al. 2022); after excluding these detectors, we indeed found fewer observations

[2]NICER Master Catalog: https://heasarc.gsfc.nasa.gov/W3Browse/nicer/nicermastr.html.

[3]SCORPEON model documentation: https://heasarc.gsfc.nasa.gov/docs/nicer/analysis_threads/scorpeon-overview/

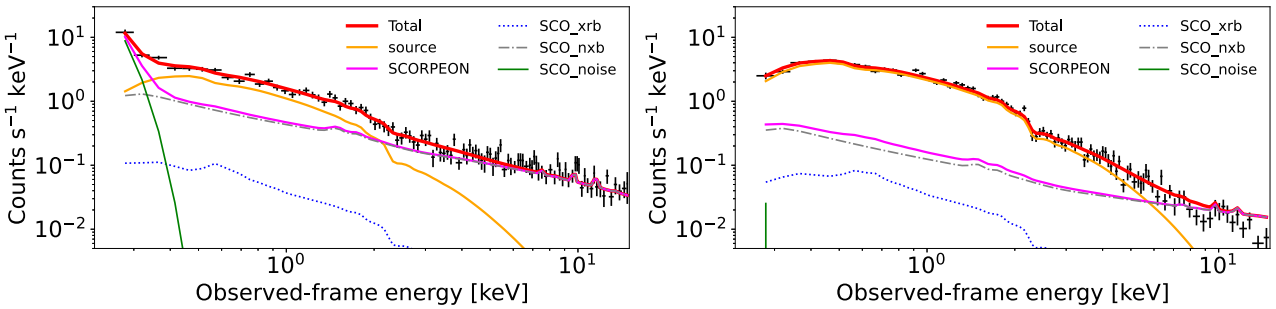

Figure 2. Examples of NICER spectra with unacceptable (left panel; observation ID 5667010101) and acceptable (right panel; observation ID 5667010401) background levels. To assess the background contribution in each NICER observation, we simultaneously fit a power-law source model and a SCORPEON background model; the latter consists of three components that are varied separately during the model fit. In the left panel, the source model (yellow curve) is fainter than the SCORPEON detector noise peak component (green curve) in the soft X-rays below ∼0.35 keV. Above ∼ 2.5 keV, the source is fainter than the non-X-ray background component (dot–dashed curve). We exclude observation ID 5667010101, and ten other observations with similarly high background levels, from our analyses.

to be affected by the 'noise peak' background feature. We extract the spectra, and the corresponding response matrices and Auxiliary Response Files required to analyse each observation, using *'nicerl3-spect'*.

3 X-RAY ANALYSIS

Here, we present an analysis of the *NuSTAR*, *XMM–Newton,* and *NICER* data for Mrk 590. We first describe our XSPEC modelling set-up, and present the observed spectra (Section 3.1). Next, we study the strength and variability of individual emission components, based on a phenomenological model (3.2). Finally, we perform in-depth modelling of combined data sets in low- and high-flux states, to probe the emission physics and reflection geometry (Section 3.3).

3.1 Modelling methodology and data presentation

We model the X-ray data using the *PYXSPEC* (v2.1.1) implementation of the XSPEC (v12.13.0) X-ray analysis package (Arnaud 1996). We optimize the Cash statistic with Poissonian background (W-stat, e.g. Humphrey, Liu & Buote 2009), as implemented in XSPEC. We include energies between 0.25–12 keV for *XMM–Newton* data, 3–79 keV for *NuSTAR*, and 0.22–15 keV for *NICER*. For *XMM–Newton* and *NuSTAR*, we bin each individual spectrum to have at least five *background* counts per energy bin, using the HEASOFT task '*ftgrouppha*'. This binning minimizes a bias when minimizing W-stat at faint background levels, as demonstrated computationally by Giacomo Vianello,[4] and discussed by Buchner & Boorman (2023). We include multiplicative flux scaling terms $C_{\rm inst}$ for *NuSTAR* FPMB relative to FPMA, and for the *XMM–Newton* MOS1 and MOS2 detectors relative to *pn*. For data obtained simultaneously with different detectors on the same telescope, these inter-calibration offsets are in all cases <5 per cent. Throughout this work, quoted model parameter uncertainties represent 90 per cent confidence intervals as obtained using the XSPEC *'error'* task.

3.1.1 Background modelling for NICER

As a non-imaging instrument, *NICER* data do not allow for extraction of separate background spectra. To address this, we include the SCORPEON background model (Markwardt et al. 2024) in each of our *NICER* model fits. SCORPEON consists of six different physical components, governed by 26 parameters in total. The *nicerl3-spect* tool suggests constraints for these parameters, based on geomagnetic and orbital conditions, which we adopt. We fit between five and six SCORPEON parameters simultaneously with the source model; the remainder are held constant at default values. As recommended,[5] we model the entire *NICER* spectrum between 0.22 and 15 keV, even though the detector is only sensitive to astronomical flux between ∼ 0.3 and 10 keV.

3.1.2 Presentation of individual observations

To illustrate their salient features and overall data quality, we display each individual *XMM–Newton* and *NuSTAR* observation in Appendix A, as a data/model ratio against a power-law modified by Galactic absorption (defined in XSPEC as TBABS × POWERLAW). Here, we exclude the spectral regions below 2, 5.5–7, and 12.5–30 keV, to avoid fitting to the expected soft excess and reflection features. We use the appropriate Galactic absorption column density for Mrk 590, $n_{\rm H} = 2.77 \times 10^{20}$ cm^{-2} (HI4PI Collaboration et al. 2016). We note the robust detection of soft X-ray excess below ∼ 2 keV in *all* our *XMM–Newton* observations. Most of our spectra also show excess emission near 6.4 keV. This feature appears rather weak in the 2021 August *XMM–Newton* data, and is not immediately apparent in all *NuSTAR* spectra, probably due to inadequate statistics in individual visits (e.g. 2016 February; 20 ks observed).

For presentation purposes, throughout this work we only display data from a single detector per telescope, choosing *XMM–Newton pn* and *NuSTAR* FPMA. Furthermore, we bin the displayed spectra such that each energy bin is detected at least the 3σ level above the background. We emphasize that these choices only affect the figures, and not the underlying spectral modelling, which is performed using minimally binned data and including all X-ray detectors.

3.2 Modelling of individual observations

To study the variability of the continuum, soft excess and Fe K line emission features in our individual observations, we now

[4]URL: https://giacomov.github.io/Bias-in-profile-poisson-likelihood/

[5]SCORPEON modelling best practices: https://heasarc.gsfc.nasa.gov/docs/nicer/analysis_threads/scorpeon-xspec/.

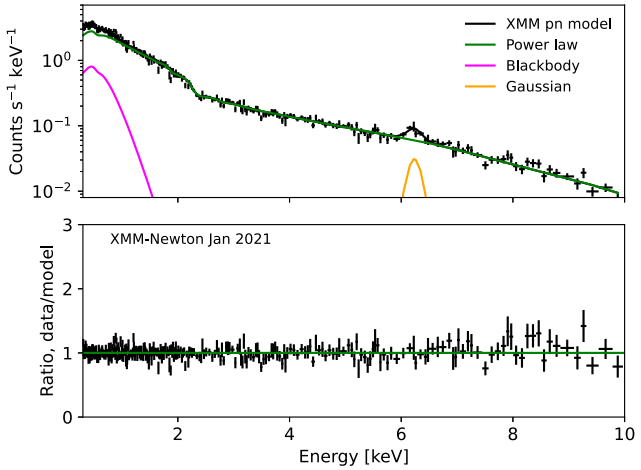

Figure 3. Top panel: Count-rate spectra and best-fitting folded model components for our phenomenological model (Section 3.2), consisting of a power-law continuum, blackbody component, and Gaussian emission line (solid curves), for the 2021 January *XMM–Newton* data (points with error bars). Bottom panel: the data/model counts ratio indicates that this model captures, to first order, the excess emission below 2 keV and near 6.4 keV.

define a simple phenomenological model. We represent the soft excess with a single-temperature blackbody component, and include a single Gaussian emission line with its centroid fixed to rest-frame 6.4 keV. The resulting model is TBABS × (POWERLAW + ZBBODY + ZGAUSS). Its free parameters are: the blackbody temperature $kT_{\rm BB}$, the Gaussian width $\sigma_{\rm line}$, the continuum photon index Γ, and the separate normalizations of the three additive components. For the *NuSTAR* observations, which do not sample the soft X-rays, we simplify the model to TBABS×(POWERLAW + ZGAUSS). We present an example of our phenomenological model in Fig. 3, and list the best-fitting parameters for each observation in Table 2. Below, we explore the derived properties of the continuum, soft excess, and 6.4 keV line.

3.2.1 Primary continuum

For comparison purposes, we report the continuum flux between 0.3 and 10 keV, $F_{0.3-10}$, throughout this work; we extrapolate the best-fitting power-law component below 3 keV for *NuSTAR*. $F_{0.3-10}$ varies by a factor of ~ 5.5 for the observations presented in this work, spanning a similar dynamic range for *XMM–Newton* and *NuSTAR*. For the continuum slope, we find an uncertainty-weighted average $\overline{\Gamma} = 1.70 \pm 0.01$, with a standard deviation of 0.04, for the nine individual *XMM–Newton* spectra (Fig. 4). For *NuSTAR* (11 spectra), we measure $\overline{\Gamma} = 1.66 \pm 0.01$, with a standard deviation of 0.05. *Chandra* observed Mrk 590 twice shortly after the 'turn-off' event (Denney et al. 2014; Mathur et al. 2018); their reported Γ values are rather uncertain, and fully consistent with our findings at $F_{0.3-10} \lesssim 1.5 \times 10^{-11}$ erg cm^{-2} s^{-1}. We see a possible trend of increasing Γ (i.e. spectral softening) with increasing flux. However, this is primarily driven by the two highest flux *XMM–Newton* observations. A Kendall rank correlation test yields a p-value of 0.03 for the null hypothesis of no correlation between continuum flux and Γ. Given the rather small sample size, and that Γ appears less variable for the *NuSTAR* spectra, we do not regard this as conclusive evidence that the underlying continuum slope changes.

For the *NICER* observations, as the detector sensitivity reduces steeply above ~3 keV, we found that Γ is rather poorly constrained, and typically significantly softer than that measured for near-contemporaneous *XMM–Newton* or *NuSTAR* visits. For this reason, we impose $\Gamma = 1.68$ (the average value measured by *XMM–Newton*) when modelling the *NICER* spectra. This allows us to more efficiently use these data to constrain the soft excess, as described below.

3.2.2 Soft excess

Our models consistently converge on a non-zero blackbody flux $F_{\rm BB}$ for the *XMM–Newton* data. We find that $F_{\rm BB}$ displays a tight proportionality to $F_{0.3-10}$ for the seven *XMM–Newton* observations (Fig. 5, left panel). The *NICER* data appear to follow the same trend, albeit with more scatter. For the *NICER* observation dated 2023-01-08, at a rather faint $F_{0.3-10}$ level, we find $F_{\rm BB}$ consistent with zero; all other *NICER* spectra require a non-zero blackbody flux. To extend this investigation to lower $F_{0.3-10}$, we include the results presented by Mathur et al. (2018) for their 2014 *Chandra* observation. These authors applied a similar phenomenological model to that used here.[6] Including the *XMM–Newton*, *NICER* and *Chandra* measurements, a Kendall rank correlation test yields $p = 3 \times 10^{-5}$ for 22 data points, indicating a statistically significant dependence. A linear least-squares fit yields

$$F_{\rm BB} = 0.07(\pm 0.01) F_{0.3-10} + 0.02(\pm 0.09)\,{\rm erg\,s^{-1}cm^{-2}}.$$

The intercept term is consistent with zero, indicating a proportionality. We note that Denney et al. (2014) report no evidence of deviations from a pure power-law model, for their 2013 *Chandra* observation taken at $F_{0.3-10} = 1.1 \times 10^{-12}$ erg cm^{-2} s^{-1}. We re-analysed those data and are unable to obtain useful constraints on a blackbody soft excess component, given the rather short (30 ks) exposure time and faint source flux. We therefore exclude the 2013 data from this analysis. We conclude that $F_{\rm BB}$ is proportional to $F_{0.3-10}$ down to at least $F_{0.3-10} \sim 2 \times 10^{-12}$ erg cm^{-2} s^{-1}.

We see a similar trend of increasing $F_{\rm BB}$ with UV flux, albeit with a larger scatter (Fig. 5, right panel). Here, we compare with the nearest in time *Swift UW2* observation. We find $p = 0.02$ for the null hypothesis, now considering only 18 data points as we lack UV photometry in 2002–2004. To quantify the $F_{\rm UV}$–$F_{\rm BB}$ relationship, we first subtract a constant host galaxy contribution of 2.1×10^{-16} erg cm^{-2} s^{-1} Å^{-1} from each UVOT measurement. We base this estimate on a flux variability gradient analysis (Lawther et al. in preparation), following the method of Gianniotis, Pozo Nuñez & Polsterer (2022). A linear fit to the host-subtracted data yields

$$10^{-2} F_{\rm BB} = 0.6(\pm 0.1) F_{\rm UV} \times 1\text{Å} - 1.9(\pm 1.4)\,{\rm erg\,s^{-1}cm^{-2}}.$$

This relationship displays a non-zero intersect, but only at the $\sim 1.3\sigma$ level. As the exact value of this intersect is sensitive to the assumed host galaxy contribution, we find it premature to claim that the soft excess component 'turns off' at the faintest UV flux levels, based on available data.

For our *XMM–Newton* spectra, the blackbody temperature $kT_{\rm BB} \sim 138$ eV is roughly constant, with no dependence on $F_{0.3-10}$ (Fig. 6). We note that the *NICER* spectra yield a systemati-

[6]Their approach differed only in the inclusion of an additional, ionized Fe K line at 6.7 keV. While a narrow feature at 6.7 keV is visible in some of our *XMM–Newton* spectra, we do not include it in our phenomenological model, due to the varying signal to noise ratios for our individual observations. Its omission is unlikely to affect the measured flux of the continuum or soft excess components.

Table 2. Phenomenological modelling of soft excess and Iron emission in individual spectra.

Telescope	Observation date	Γ	$F_{\rm BB}$ (10^{-13}erg cm^{-2}s^{-1})	$kT_{\rm BB}$ (keV)	$\sigma_{\rm line}$ (eV)	EW (eV)	$F_{\rm line}$ (10^{-13} erg cm^{-2}s^{-1})
(1)	(2)	(3)	(4)	(5)	(6)	(7)	(8)
XMM–Newton	2002-01-01	1.71 ± 0.03	$5.5^{+1.7}_{-1.6}$	147^{+13}_{-14}	–	586^{+298}_{-202}	$3.2^{+0.9}_{-1.2}$
	2004-07-04	1.67 ± 0.02	7.2 ± 0.8	139^{+5}_{-6}	< 68	116^{+34}_{-32}	0.9 ± 0.2
	2020-07-04	1.69 ± 0.02	7.1 ± 1.1	147 ± 8	< 115	140^{+47}_{-44}	$1.0^{+0.4}_{-0.3}$
	2021-01-03	1.69 ± 0.02	8.4 ± 1.2	140^{+6}_{-7}	< 141	152 ± 46	$1.4^{+0.4}_{-0.4}$
	2021-08-11	1.78 ± 0.02	$14.1^{+2.3}_{-2.5}$	133 ± 7	< 75	62^{+44}_{-48}	$0.8^{+1.7}_{-0.5}$
	2022-01-24	1.67 ± 0.04	2.8 ± 0.6	129^{+12}_{-13}	187^{+115}_{-64}	496^{+148}_{-141}	$1.4^{+0.4}_{-0.3}$
	2022-07-28	1.65 ± 0.02	6.1 ± 1.0	147 ± 8	< 203	111^{+50}_{-51}	$0.7^{+0.5}_{-0.3}$
	2023-02-06	1.64 ± 0.02	5.1 ± 0.7	141 ± 7	129^{+59}_{-48}	241^{+61}_{-64}	1.2 ± 0.3
	2024-01-25	1.77 ± 0.02	$12.2^{+1.8}_{-1.5}$	124 ± 6	–	195^{+106}_{-71}	2.7 ± 0.9
NuSTAR	2016-02-05	$1.59^{+0.08}_{-0.07}$	–	–	< 756	216^{+182}_{-199}	$0.8^{+0.7}_{-0.8}$
	2016-12-02	1.61 ± 0.05	–	–	398^{+205}_{-192}	357^{+154}_{-138}	$1.3^{+0.5}_{-0.5}$
	2018-10-27	1.61 ± 0.04	–	–	< 434	300^{+273}_{-237}	$3.4^{+1.8}_{-2.1}$
	2019-08-31	1.66 ± 0.02	–	–	< 201	101^{+35}_{-32}	$1.7^{+0.6}_{-0.5}$
	2020-01-21	1.67 ± 0.02	–	–	377^{+186}_{-200}	194^{+61}_{-68}	$2.5^{+1.2}_{-0.9}$
	2021-01-10	1.67 ± 0.04	–	–	< 360	190^{+82}_{-78}	$1.5^{+0.7}_{-0.6}$
	2021-08-18	1.69 ± 0.03	–	–	< 488	165 ± 64	$2.8^{+1.5}_{-1.1}$
	2021-12-22	1.65 ± 0.03	–	–	< 437	186^{+64}_{-63}	$1.2^{+0.5}_{-0.4}$
	2023-02-06	1.66 ± 0.04	–	–	< 444	215^{+142}_{-82}	$1.2^{+0.6}_{-0.4}$
	2023-09-29	1.68 ± 0.07	–	–	< 416	176^{+316}_{-113}	$0.7^{+0.7}_{-0.6}$
	2024-01-25	1.72 ± 0.02	–	–	–	79^{+5}_{-39}	$1.0^{+0.8}_{-0.3}$
NICER	2022-07-16	–	$3.6^{+2.2}_{-1.9}$	208^{+86}_{-74}	–	–	–
	2022-07-26	–	$6.7^{+1.8}_{-1.7}$	209^{+24}_{-27}	–	–	–
	2022-08-15	–	$11.0^{+1.9}_{-1.7}$	155^{+17}_{-16}	–	–	–
	2022-08-24	–	$5.2^{+2.1}_{-2.0}$	169^{+43}_{-39}	–	–	–
	2022-08-25	–	$6.5^{+1.7}_{-1.6}$	193^{+32}_{-28}	–	–	–
	2022-09-14	–	$3.2^{+1.1}_{-1.4}$	143^{+28}_{-29}	–	–	–
	2022-09-25	–	$4.0^{+1.7}_{-1.5}$	182^{+33}_{-31}	–	–	–
	2022-10-04	–	$5.3^{+3.2}_{-3.2}$	234^{+59}_{-67}	–	–	–
	2022-10-24	–	$4.1^{+1.9}_{-1.7}$	200^{+32}_{-35}	–	–	–
	2022-11-12	–	$1.5^{+1.3}_{-1.0}$	139^{+69}_{-44}	–	–	–
	2022-12-03	–	$2.2^{+2.0}_{-1.6}$	216^{+61}_{-68}	–	–	–
	2023-01-08	–	< 2.1	–	–	–	–

Note. Here, we list best-fitting parameters for the phenomenological model TBABS*(POWERLAW + ZGAUSS + ZBBODY) (Section 3.2). All parameter uncertainties are quoted at the 90th percentile confidence interval. (1) Telescope name. (2) Date of observation start, YYYY-MM-DD. (3) Continuum photon index. As the model is fitted to the full instrumental energy range, the spectral slope may vary systematically between instruments, even if it is not time-variant. We find that *NICER* cannot robustly recover Γ for these short individual exposures (Section 3.2) (4) Integrated flux of the blackbody component; this is only included for *XMM–Newton* and *NICER* spectra. (5) Temperature of the blackbody component. (6) Line width of the 6.4 keV Gaussian emission component. Most of these are upper limits at the 90 per cent confidence interval; the nominal energy resolutions near the Fe K line are 400 eV for *NuSTAR* and 150 eV for *XMM–Newton pn*. Thus, the emission lines are largely unresolved. (7) Equivalent width of the Gaussian component. (8) Integrated flux of the Gaussian component.

cally higher blackbody temperature, $kT_{\rm BB} \sim 187$ eV, with much larger uncertainties. This is to some extent due to the lower signal-to-noise ratio in the short *NICER* observations. We also suspect that the 'noise ringer' feature in the *NICER* background (Fig. 2, green curve), modelled with SCORPEON, may be somewhat degenerate with the soft excess component, potentially biasing the $kT_{\rm BB}$ measurements towards higher energies.

3.2.3 6.4 keV emission line

For the 6.4 keV Gaussian component, we find a non-zero equivalent width (EW) in all *XMM–Newton* observations, and all but one *NuSTAR* observation. The 2016 February *NuSTAR* observation displays $EW \sim 0$, likely due to a low signal-to-noise ratio. The individual *NuSTAR* spectra typically provide poor constraints on EW, except at the highest flux levels. The line fluxes are roughly constant as

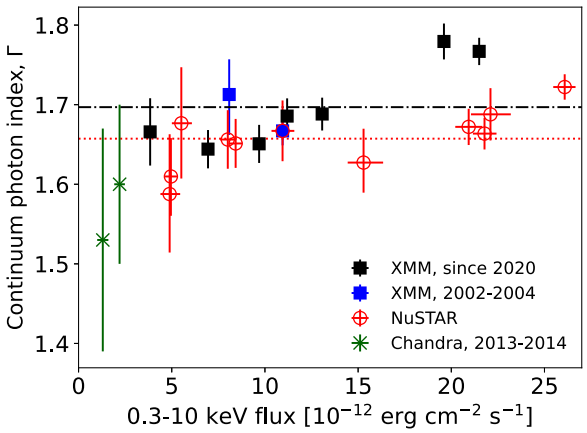

Figure 4. The 0.3–10 keV continuum photon index, measured using our phenomenological models (Section 3.2), as a function of 0.3–10 keV flux, for each individual observation. The dotted and dash–dotted lines illustrate the uncertainty-weighted mean photon indices for *NuSTAR*, $\overline{\Gamma} = 1.66$, and for *XMM–Newton*, $\overline{\Gamma} = 1.70$, respectively. For comparison, we include published results for two *Chandra* observations obtained shortly after the 'turn-off' event (Denney et al. 2014; Mathur et al. 2018).

a function of continuum flux, leading to a modest increase in line equivalent width at the lowest continuum flux levels observed (Fig. 7). The latter trend, sometimes referred to as an 'X-ray Baldwin effect', is well-known from statistical samples of AGN (Iwasawa & Taniguchi 1993; Nandra et al. 1997; Ricci et al. 2014). The line width of the Gaussian component is at best marginally resolved. In most cases, we obtain an upper limit, of order $\sigma_{\rm line} < 160$ eV for *XMM–Newton* spectra (Table 2). This is consistent with Keplerian rotation around the central black hole at a distance of order 800 gravitational radii, which corresponds to roughly three light-days. Thus, we cannot exclude that the main X-ray reprocessing is co-spatial with the primary UV reprocessing region, also located around three light-days from the X-ray source (Paper 1). However, we caution that the distance inferred via the Fe K linewidth is only a lower limit.

Several of our *XMM–Newton* observations (e.g. January 2022, Fig. A1) show additional narrow excess features at energies above 6.4 keV, perhaps due to Fe Kβ (7.06 keV) and/or ionized He-like Kα (6.7 keV). We do not attempt to model these for individual observations, as they are in many cases only marginally detected.

3.3 Modelling of combined 0.3–79 keV data sets

Here, we construct combined data sets using both *XMM–Newton* and *NuSTAR*, to exploit the full 0.3–79 keV energy range and improve the photon counting statistics (Section 3.3.1). This facilitates an in-depth model comparison (Section 3.3.2) to determine the most likely emission mechanisms (Section 3.3.3).

3.3.1 Construction of combined data sets

According to our analysis of the individual spectra (Section 3.2), the overall continuum flux level appears to be the main driver of X-ray spectral shape changes. For this reason, we elect to combine data taken at similar flux levels. We select all observations with $F_{0.3-10} < 7 \times 10^{-12}$ erg cm^{-2} s^{-1} to construct a 'low-flux' joint data set (hereafter, LF). Similarly, we include all observations with $F_{0.3-10} > 18 \times 10^{-12}$ erg cm^{-2} s^{-1} in our 'high-flux' data set (HF). These flux cut-offs are fairly arbitrary: our aim is to separate the brightest and faintest states captured in our observations, while achieving sufficiently long exposure times to distinguish between competing emission models. We list the observations included in each data set in Table 1.

We stack all spectra from a given instrument, in each data set, using the HEASOFT task '*addspec*' for *NuSTAR* instruments, and the SAS task '*epicspeccombine*' for *XMM–Newton*. We include cross-calibration constants $C_{\rm inst}$ in our modelling, for each instrument, relative to EPIC *pn* (so, $C_{\rm PN} \equiv 1$). The flux offsets reach ± 18 per cent between *XMM–Newton* and *NuSTAR* instruments. This is partially due to our use of non-contemporaneous *XMM–Newton* and *NuSTAR* observations; however, flux offsets between *XMM–Newton* and *NuSTAR* reach ~ 10 per cent even for contemporaneous data (Tsujimoto et al. 2011). To test whether the stacking biases our results, we define two additional data sets using near-contemporaneous *XMM–Newton* and *NuSTAR* observations. The first of these occurred in January 2021 (hereafter, J21), at an intermediate flux state, $F_{0.3-10} \sim 1.2 \times 10^{-11}$ erg s^{-1} cm^{-2}. The second occurred in 2023 February (hereafter, F23), at $F_{0.3-10} \sim 6 \times 10^{-12}$ erg s^{-1} cm^{-2}.

To demonstrate the overall data quality and the prominent features in these data sets, we present power-law model fits to the LF and HF spectra in Fig. 8. Both data sets display an obvious soft excess below ~ 2 keV, and some Fe K emission; the latter appears stronger (relative to the continuum) for the LF data. We also note hints of spectral curvature at $\sim$30–60 keV, although the statistics are rather poor at those energies, even for the combined *NuSTAR* data.

3.3.2 Bayesian model comparison

To determine which emission models can describe – and are warranted by – our joint data sets, we apply a Bayesian model comparison approach (e.g. Kass & Raftery 1995). This approach compares the evidences Z for a series of models, integrated over their respective parameter spaces. Advantages of the Bayes factor approach for model selection in astronomy are discussed by, e.g. Mukherjee, Parkinson & Liddle (2006); Trotta (2007). Notably, it is valid for both non-nested and nested model comparison, and, unlike null hypothesis testing, can indicate a preference for either model. It penalizes models that are *non-predictive* (i.e. flexible) over the parameter space defined by the prior probabilities.

We describe this model selection procedure in detail, and define each model tested, in Appendix B. Briefly, for each data set (LF, HF, J21, and F23), we use the Bayesian X-ray Analysis package (Buchner et al. 2014; Buchner 2016) to calculate the evidences Z for a series of models. This results in a unique 'best' model with evidence $Z_{\rm best}$ for each data set, and a range of 'acceptable' models satisfying a limiting Bayes factor, $\log(Z_{\rm best}) - \log(Z_{\rm model}) < 3$, relative to the best model. We justify our choice of limiting Bayes factor in Appendix B, and tabulate the Bayes factors $\log(Z_{\rm best}) - \log(Z_{\rm model})$ for each model in Table B2.

The key results of our model comparison are (1) *inverse Compton scattering in a warm medium is formally required* to produce the observed soft excess, for all four data sets. Models not including warm-Comptonized emission are disfavoured by very large Bayes factors. We note that we tested against the state-of-the-art relativistic reflection model RELXILLLPCP (Dauser et al. 2022), which allows for higher density discs, as favoured for black hole masses of $\sim 10^7$ M$_\odot$ and below (Jiang et al. 2018; Mallick et al. 2022) and is required to produce very strong soft excess via reflection (Madathil-Pottayil

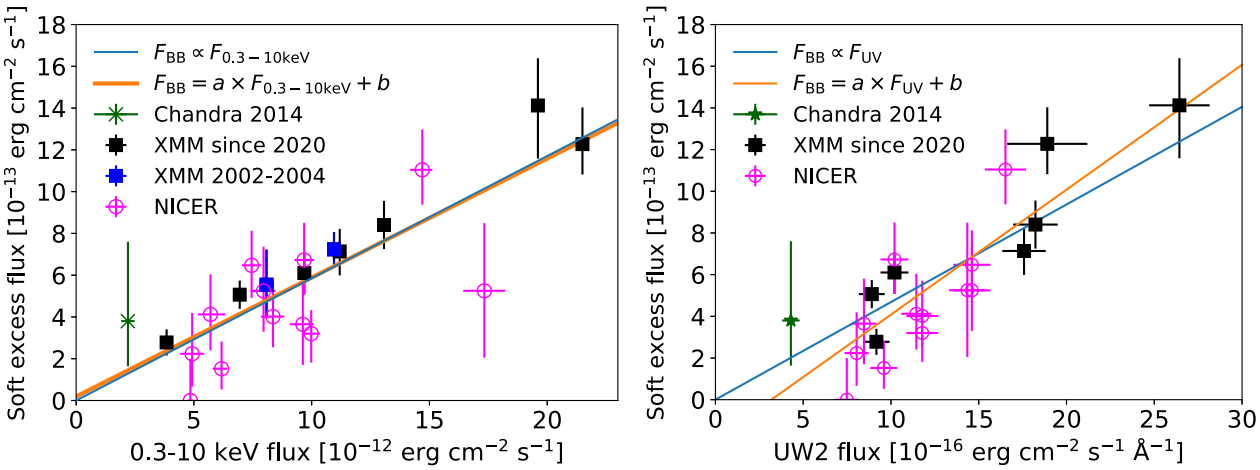

Figure 5. The flux F_{BB} of the blackbody component, integrated over 0.3–10 keV, versus that of the power-law continuum component $F_{0.3-10}$ *(left panel)*, and versus the host galaxy-subtracted *Swift* UVOT *UW2* flux density *(right panel)*. Both F_{BB} and $F_{0.3-10}$ are derived from our phenomenological model (Section 3.2). The straight lines depict the best-fitting zero-offset proportionality and linear relationship, fitted to the N*ICER* (circles), *XMM–Newton* (squares; blue squares for spectra taken in 2002–2004), and *Chandra* (asterisk; Mathur et al. 2018) measurements. The early *XMM–Newton* measurements are not included for the UV flux–F_{BB} relationship, as no UV photometry is available.

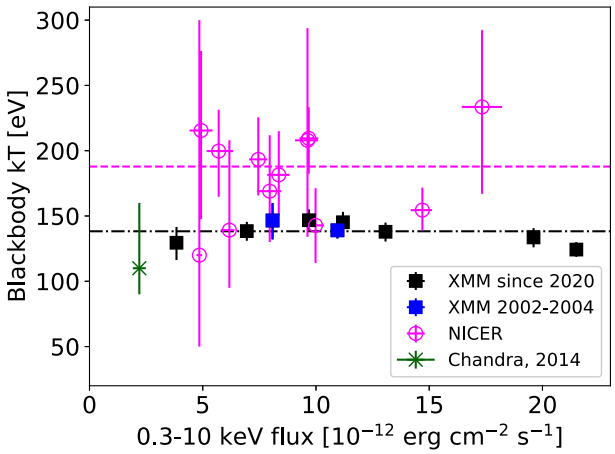

Figure 6. The temperature kT of the blackbody component, for the phenomenological model described in Section 3.2. The *XMM–Newton* data points (squares) show negligible scatter around the average value $\overline{kT} = 138 \pm 1$ eV (dash–dotted line). The *NICER* kT values (open circles) are poorly constrained, at a higher average temperature $\overline{kT} = 187 \pm 3$ eV (dashed line). For the *Chandra* observation, we adopt the blackbody temperature presented by Mathur et al. (2018).

et al. 2024). Nevertheless, models including warm-Comptonized emission are better able to reproduce the observed spectra. (2) Distant reflection is required, due to the dominant narrow Fe K line (e.g. Fig. 8); models including *only* disc reflection features are disfavoured by very large Bayes factors, as they produce insufficient narrow emission at 6.4 keV. (3) A contribution from disc reflection is formally acceptable, but not required. Models with both distant and relativistic reflection produce a marginally higher Bayesian evidence for both LF and HF, while the simpler distant reflection-only models are marginally preferred for the J21 and F23 data sets, perhaps due to poorer statistics.

For the primary X-ray continuum, we find that an exponential high-energy cut-off is preferred (relative to a power law with no cut-off) for all data sets. Surprisingly, replacing the cut-off power-law component with a more realistic hot-Comptonized emission model (NTHCOMP) is disfavoured, even though this mechanism is typically assumed for the coronal emission (Section 1). We return to this puzzle in Section 4.3. Finally, we find that both neutral and ionized intrinsic absorption is in all cases strongly disfavoured; the X-ray emission is thus largely unabsorbed at any observed flux level.

3.3.3 *Definitions of our preferred models*

Here, we define the two models that are formally acceptable for all four 0.3–79 keV data sets. These are labelled as Models C2 and G in Appendix B.

Warm-Comptonized emission and distant reflection This model consists of a power-law continuum with an exponential cut-off, warm-Comptonized emission, and a non-rotating reflection component. In XSPEC modelling parlance, this model is defined as CONST×TBABS(ZCUTOFFPL+NTHCOMP + PEXMON). Here, the CONST component represents a multiplicative scaling between different instruments, while TBABS represents Galactic absorption.
The NTHCOMP component (Zdziarski et al. 1996; Życki, Done & Smith 1999) models inverse Compton scattering, assuming a seed photon temperature of 10 eV (i.e. UV seed photons), and a single electron temperature kT_e. The PEXMON component (Nandra et al. 1997) represents reflection in a slab of stationary material. It is parametrized by a reflection strength R, an inclination angle i, a metallicity Z and an iron abundance A_{Fe}, where the latter is treated separately due to the importance of iron emission in observed AGN spectra. We tie the incident-continuum photon index and cut-off energy of the PEXMON component to those of the primary continuum component.

Warm-Comptonized emission with dual reflection regions This model includes an additional relativistic reflection component. It is defined as CONST × TBABS (ZCUTOFFPL + NTHCOMP + PEXMON + RELXILLLP). The component RELXILLLP (Dauser et al. 2014; García et al. 2018) represents reprocessing of a point-source X-ray

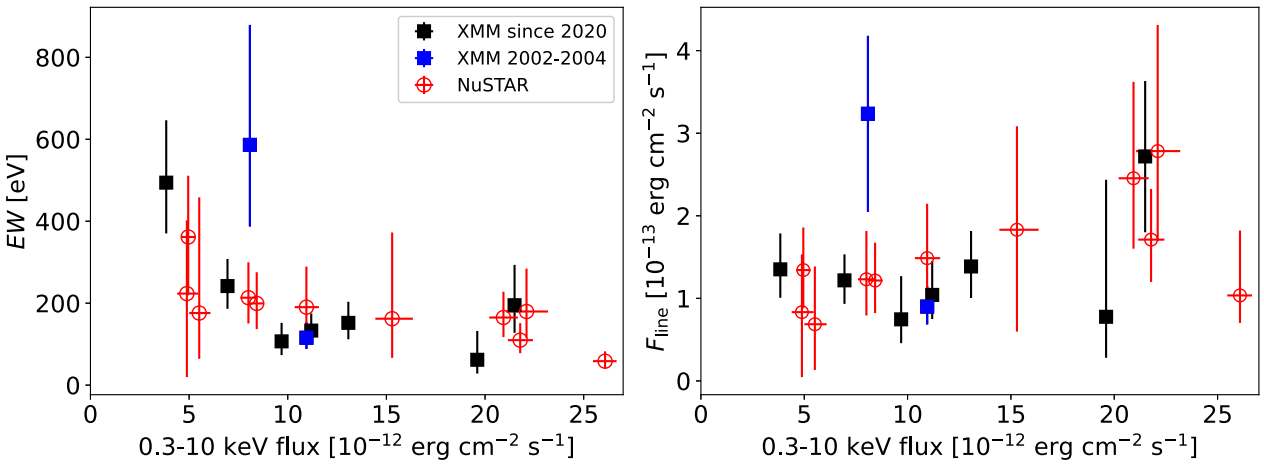

Figure 7. The equivalent width (left panel) and integrated line flux (right panel) of a single Gaussian emission line with centroid fixed to 6.4 keV, versus the X-ray continuum flux. The linewidth is allowed to vary freely during the model fit.

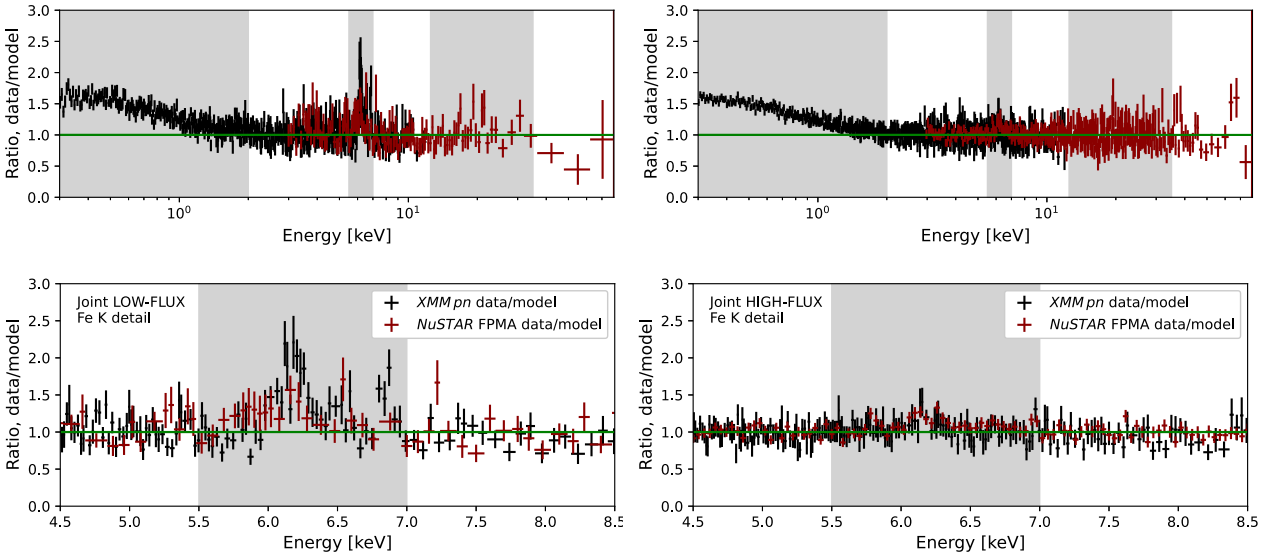

Figure 8. Joint data sets modelled against a power law with Galactic absorption, excluding the grey shaded regions from the model fit (following Section 3.1). The low-flux (LF) data is shown in the left panels, while the right panels show the HF data set. The top panels show the data/model ratios for the entire 0.3–79 keV range. A detailed view of the Fe K emission complex is shown in the bottom panels.

continuum in a 'thin disc' extending to the innermost circular stable orbit, with appropriate rotational blurring applied. We assume that the two reflection regions represent inner and outer regions of the same bulk accretion flow. Thus, we tie the RELXILLLP inclination angle $i_{\rm rel}$ and iron abundance $A_{\rm Fe,rel}$ to those of the PEXMON component. For consistency, we tie the incident photon indices and high-energy cut-offs of both reflection components to that of the primary continuum. As the RELXILLLP component represents reflection in the inner accretion flow, the reprocessing material may be highly ionized. This is parameterized in the model as $\xi_{\rm rel}$, the ionization parameter at the inner edge of the disc; the ionization throughout the disc is then scaled according to the thin-disc prescription. The height of the continuum source is set to 10 gravitational radii above the disc, while its outflow velocity is set to zero. The relativistic reflection is rather faint in both LF and HF, as discussed below; thus, the values of these parameters do not strongly affect the total model spectrum, and are not constrained by the data.

3.3.4 Properties of our preferred models

To explore the behaviour of these two models, we perform *C-stat* minimization to each data set. We present the best-fitting model parameters in Table 3. We present the model spectra in Figs 9 and 10 (LF), and Figs 11 and 12 (HF). We display these preferred models as $E^2 f(E)$ spectra, unfolded from the instrumental response (e.g. Gunderson & Huenemoerder 2025), to illustrate the energy output at a given photon energy. In the following, we comment on notable features of the best-fitting models, and on significant differences between the LF and HF states.

Continuum: The measured primary continuum properties are insensitive to whether relativistic reflection is included. We

Table 3. Best-fitting parameters for our preferred models.

Row	Parameter	LF	HF	J21	F23
(1)	$N_{\rm H,Gal}$	2.77×10^{20}	2.77×10^{20}	2.77×10^{20}	2.77×10^{20}
(2)	Z	1	1	1	1
(3)	i	$38^\circ \pm 7^\circ$	38°	38°	38°
(4)	$A_{\rm Fe}$	$6.9^{+9.0}_{-3.3}$	6.9	6.9	6.9
(5)	z	0.026385	0.026385	0.026385	0.026385
	Distant reflector only, CONST×TBABS(ZCUTOFFPL+NTHCOMP + PEXMON)				
	Continuum				
(6)	$\rm N_{cont}$	$7.5(\pm0.2)\times10^{-4}$	$3.0(\pm0.4)\times10^{-3}$	$1.7(\pm0.1)\times10^{-3}$	$9.2(\pm0.4)\times10^{-4}$
(7)	Γ	$1.57^{+0.02}_{-0.03}$	1.66 ± 0.01	$1.59^{+0.04}_{-0.05}$	$1.58^{+0.04}_{-0.05}$
(8)	$E_{\rm cut}$	142 ± 43	>255	85^{+56}_{-26}	84^{+50}_{-26}
	Soft excess				
(9)	$\rm N_{warm}$	$1.7(\pm0.2)\times10^{-4}$	$5.9(\pm0.4)\times10^{-4}$	$4.6(\pm0.9)\times10^{-4}$	$2.0(\pm0.4)\times10^{-4}$
(10)	kT_e	0.21 ± 0.03	0.28 ± 0.03	$0.24^{+0.05}_{-0.04}$	$0.20^{+0.04}_{-0.02}$
(11)	$\Gamma_{\rm warm}$	$1.90^{+0.14}_{-0.17}$	2.23 ± 0.08	$2.01^{+0.17}_{-0.23}$	1.83 ± 0.23
	Distant refl.				
(12)	R	$-0.38^{+0.09}_{-0.12}$	-0.14 ± 0.02	-0.25 ± 0.05	-0.34 ± 0.06
	Instrumental				
(13)	$C_{\rm MOS1}$	1.03 ± 0.01	1.05 ± 0.01	0.98 ± 0.01	1.01 ± 0.01
(14)	$C_{\rm MOS2}$	1.04 ± 0.01	1.03 ± 0.01	0.97 ± 0.01	1.03 ± 0.01
(15)	$C_{\rm FPMA}$	0.87 ± 0.01	1.15 ± 0.01	0.84 ± 0.01	1.13 ± 0.01
(16)	$C_{\rm FPMB}$	0.88 ± 0.01	1.19 ± 0.01	0.87 ± 0.01	1.16 ± 0.01
	Dual reflectors, CONST×TBABS(ZCUTOFFPL+NTHCOMP+PEXMON + RELXILLLP)				
	Continuum				
	$\rm N_{cont}$	$7.3(\pm0.2)\times10^{-4}$	$2.9(\pm0.1)\times10^{-3}$	$1.7(\pm0.1)\times10^{-3}$	$9.2(\pm0.4)\times10^{-4}$
	Γ	1.57 ± 0.03	1.66 ± 0.02	1.59 ± 0.04	$1.59^{+0.04}_{-0.05}$
	$E_{\rm cut}$	166^{+154}_{-57}	>242	80^{+50}_{-23}	79^{+47}_{-24}
	Soft excess				
	$\rm N_{warm}$	$1.1(\pm0.3)\times10^{-4}$	$5.4(\pm0.6)\times10^{-4}$	$4.1(\pm0.9)\times10^{-4}$	$1.9(\pm0.5)\times10^{-4}$
	kT_e	0.20 ± 0.04	0.26 ± 0.02	$0.24^{+0.06}_{-0.04}$	$0.21^{+0.05}_{-0.03}$
	$\Gamma_{\rm warm}$	$1.98^{+0.20}_{-0.25}$	$2.27^{+0.11}_{-0.10}$	$2.02^{+0.19}_{-0.22}$	1.91 ± 0.24
	Distant refl.				
	R	-0.34 ± 0.05	-0.12 ± 0.02	-0.24 ± 0.04	-0.30 ± 0.06
	Rel. refl.				
(17)	$N_{\rm rel}$	$7.2(\pm6.4)\times10^{-6}$	$6.4(\pm4.0)\times10^{-6}$	$4.2(^{+10.1}_{-4.2})\times10^{-6}$	1.7 ± 0.8
(18)	$R_{\rm rel}$	1	1	1	1
(19)	$\log(\xi)_{\rm rel}$	2.8 ± 0.3	3.2 ± 0.2	$2.3^{+0.4}_{-2.3}$	$1.7^{+1.1}_{-1.4}$
(20)	$h_{\rm rel}$	10	10	10	10
(21)	$\beta_{\rm rel}$	0	0	0	0
	Instrumental				
	$C_{\rm MOS1}$	1.03 ± 0.01	1.05 ± 0.01	0.98 ± 0.01	1.01 ± 0.01
	$C_{\rm MOS2}$	1.02 ± 0.01	1.02 ± 0.01	1.00 ± 0.01	1.01 ± 0.01
	$C_{\rm FPMA}$	0.87 ± 0.01	1.15 ± 0.01	0.84 ± 0.02	1.13 ± 0.02
	$C_{\rm FPMB}$	0.89 ± 0.01	1.19 ± 0.01	0.87 ± 0.02	1.16 ± 0.02

Note. Best-fitting model parameters for our preferred models (Section 3.3.4), for the low-flux (LF), high-flux (HF), 2021 January (J21), and 2023 February (F23) data sets. The uncertainties correspond to 90 per cent confidence intervals. Parameters listed in grey are held constant during the model fit procedure. In particular, the reflection component iron abundance $A_{\rm Fe}$ and inclination i are only constrained for LF; we use the best-fitting LF values for all other models. (1) Column density for Galactic absorption, units of $\rm cm^{-2}$. (2) Metallicity relative to Solar. (3) Inclination angle of reflection slab relative to line of sight; for the dual-reflector model, the same inclination is used for both reflection components. (4) Iron abundance relative to Solar. (5) Source redshift. (6) Normalization at 1 keV for cut-off power-law continuum. (7) Continuum photon index. (8) Continuum cut-off energy in keV. (9) Normalization for warm Comptonization component. (10) Electron temperature of Comptonizing region in keV. (11) Photon index of warm Comptonization component. (12) Reflection fraction for distant reflection, where $R = 1$ corresponds to an infinite Compton-thick slab. (13–16) Cross-calibration constants for the MOS1, MOS2, FPMA, and FPMB detectors, relative to EPIC *pn*. (17) Normalization of the relativistic reflection component, as defined by Dauser et al. (2022). (18) Reflection strength of the relativistic reflection, as defined by Dauser et al. (2022); we hold this constant and allow the normalization to vary. (19) Ionization parameter at the innermost stable circular orbit for the relativistic reflection component. (20) X-ray continuum height above the disc, in gravitational radii. (21) X-ray continuum source velocity, relative to the disc; we assume a stationary continuum source.

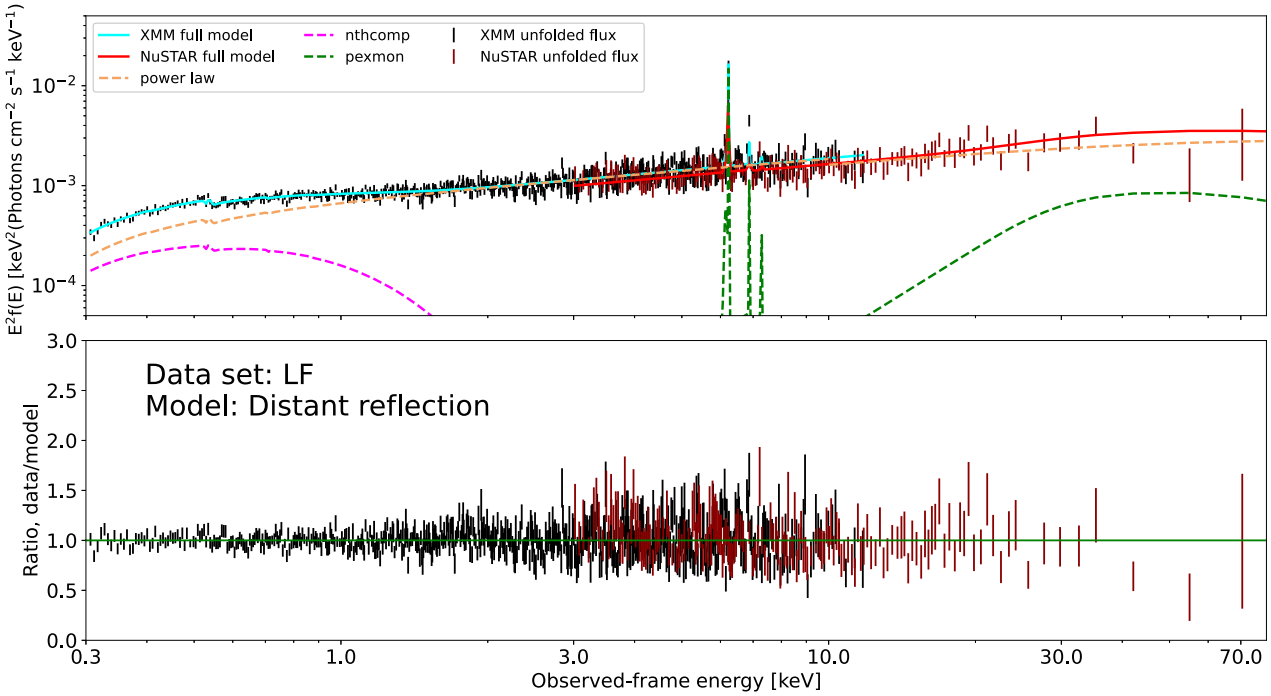

Figure 9. Best-fitting distant reflector-only model for the LF data. The top panel shows the unfolded flux spectrum for *XMM–Newton* (black error bars) and *NuSTAR* (red error bars), along with the total model and its individual additive components; the bottom panels show the data to model ratio. The upper panel y-axis displays $E^2 f(E)$, where E is photon energy in units of keV, and $f(E)$ is the photon flux density; it is analogous to νF_ν as commonly used to present AGN UV–optical spectral energy distributions. The best-fitting reflection fraction is $R \sim 0.4$, where $R = 1$ is expected for a slab reflector extending to large radii. The warm-Comptonized emission (magenta dashed curve) contributes substantially to the total model below ~ 1 keV.

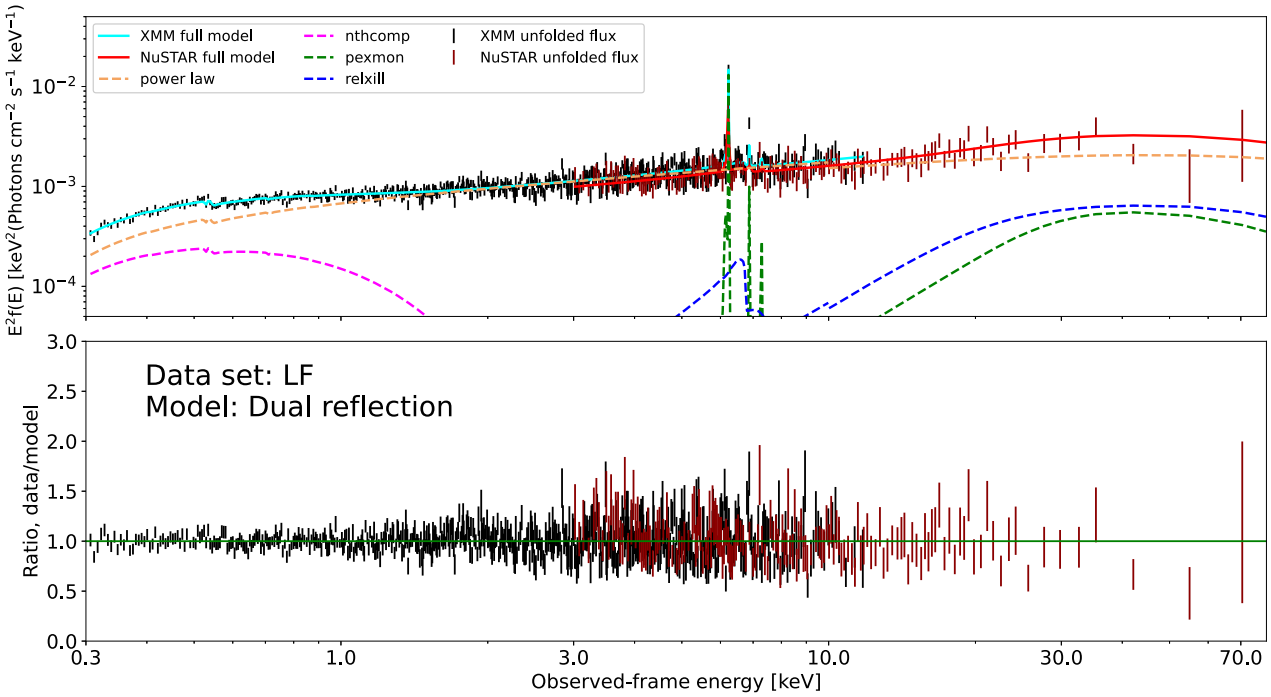

Figure 10. Best-fitting model including an additional, relativistic reflection component (*relxill*; seen here as the broad line component near 6.4 keV and as an additional high-energy Compton hump), for the LF data. Due to the faintness of the relativistic component, the full model (solid curves) is near-indistinguishable from the distant reflection-only case.

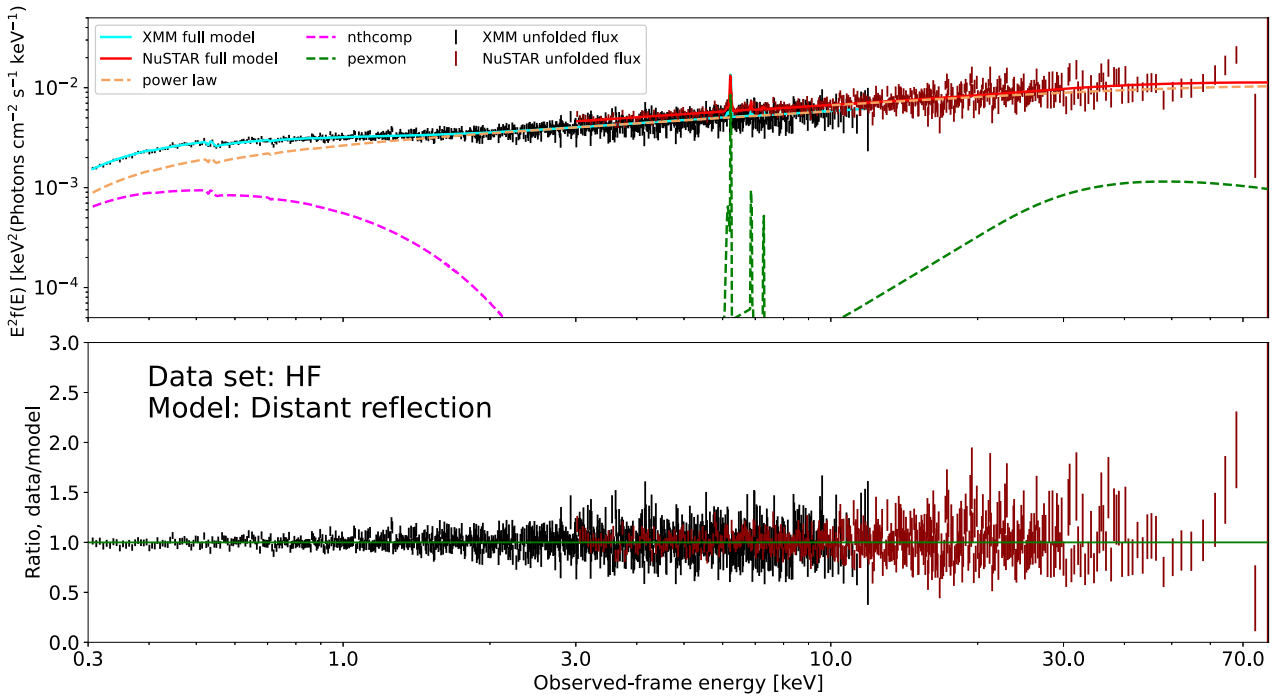

Figure 11. Best-fitting distant reflector-only model for the HF data. Here, any reflection is exceedingly weak ($R \sim 0.1$); this is consistent with a distant reflector that responds only slowly to continuum flares.

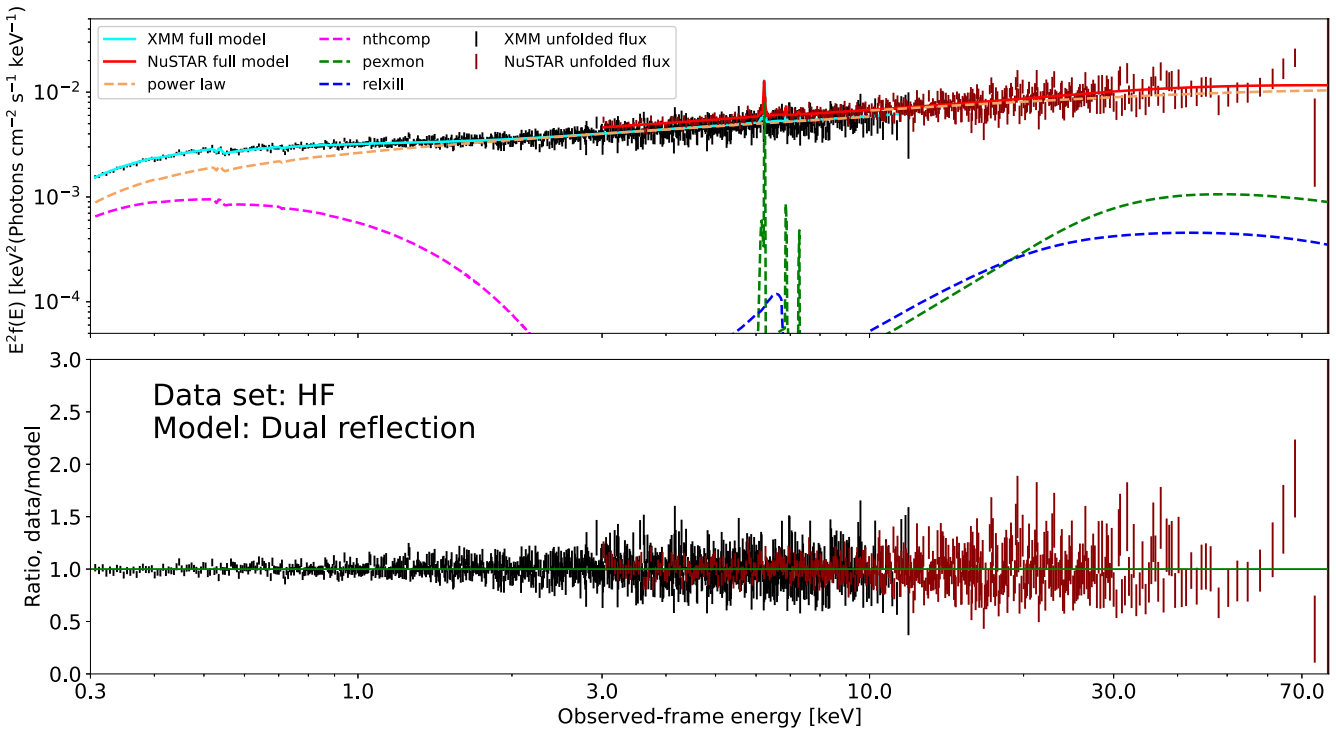

Figure 12. Best-fitting model including an additional, relativistic reflection component, for the HF data. While the data allow for some soft X-ray contribution from relativistic reflection, it is clear that this cannot account for the observed soft excess flux without severely overestimating the broad iron emission.

find that the continuum is significantly harder ($\Gamma \approx 1.56 \pm 0.02$) for the LF data, relative to the HF ($\Gamma = 1.67 \pm 0.02$). This is broadly consistent with the trend found for our individual XMM observations (Section 3.2). The high-energy cut-off is at least

a factor ~ 2 higher in the HF data ($E_{\rm cut} > 250$ keV) compared to LF ($E_{\rm cut} \approx 150$ keV).

Warm-Comptonized emission: The soft excess component is a factor ~ 4 brighter in the HF data, relative to LF; this is consistent with the flux dependence found for individual observations (Section 3.2). The photon index $\Gamma_{\rm warm}$ parametrizes the underlying optical depth and scattering geometry of the warm region. For these models fitted to X-ray data only, we find $\Gamma_{\rm warm} \approx 1.9$ for the LF data set, increasing to $\Gamma_{\rm warm} \approx 2.2$ for the HF data. However, if we also consider the UV emission, we find $\Gamma_{\rm warm} \sim 2.3$ in both cases, assuming a single warm Comptonizing region; we discuss this further in Section 4.2. The inferred temperature for the warm Comptonizing region is $kT_{\rm e} \sim 0.2$–0.3 keV, corresponding to roughly $\sim 3 \times 10^6$ K, for all data sets.

Reflection regions: We are only able to obtain useful constraints on the reflection inclination angle i and iron abundance $A_{\rm Fe}$ for the LF data set; we obtain $i = 38^\circ \pm 8^\circ$ and $A_{\rm Fe} = 6.9^{+9.0}_{-3.4}$. As neither of these parameters are likely to change on timescales of a few years, we impose these values for the other data sets. Regarding $A_{\rm Fe}$, we note that the best-fitting value is poorly constrained but significantly super-Solar. High iron abundances are commonly found when modelling reflection in AGN (Fabian et al. 2009; Reynolds et al. 2012; García et al. 2015; Kara et al. 2015). They may be due to high particle densities in the accretion discs (García et al. 2018), or due to additional iron reflection in a Compton-thin broad line region (Patrick et al. 2012). In our models, $A_{\rm Fe}$ is most usefully regarded as a degree of freedom governing the relative strengths of the Fe K line and Compton hump. These are otherwise set by the assumption of a Compton-thick, low-density reflection medium; we cannot infer the real iron abundance independently of that assumption. The black hole spin, which affects the relativistic reflection profile, is unconstrained for all data sets; we set it to $a_* \equiv 0$. We confirm that setting the maximal value of $a_* = 0.998$ does not meaningfully alter the total model.

Considering the distant reflection-only model, we obtain reflection factors of $R = 0.38^{+0.09}_{-0.12}$ for LF and $R = 0.14 \pm 0.02$ for HF. This is weaker than the $R = 1$ expected for a Compton-thick slab extending to large radii, indicating that the reflection geometry may be truncated, patchy, and/or Compton-thin. Given that our HF observations capture Mrk 590 during short, sharp X-ray outbursts, the lower reflection fraction for HF likely indicates a delayed response of the distant reflection region. For the dual reflection model, the *distant* reflection factors fall only negligibly, to $R = 0.34 \pm 0.05$ and $R = 0.12 \pm 0.02$, respectively; this supports that the reflection spectrum is dominated by distant reprocessing. The relativistic reflection component contributes only weakly to the overall emission spectrum (Figs 10 and 12, blue curves). It displays a smooth, near-featureless profile. This necessitates a high ionization of the (putative) disc reflection surface; we find $\log(\xi) \sim 3$ for both the LF and HF data sets. In summary, these model fits support the conclusions of our model comparison study (Appendix B): weak, highly ionized relativistic reflection may be present, but is not required to explain these spectra.

4 DISCUSSION

4.1 A variable yet persistent soft X-ray excess

We detect a soft X-ray excess in Mrk 590 at all observed flux levels. Its emission strength is highly correlated with both the X-ray and the UV continuum variability (Section 3.2). While we only have two *XMM–Newton* observations obtained prior to the initial 'turn-off' event, the soft excess level in those data is fully consistent with the overall trend (Fig. 5). This is at odds with results for Mrk 590 presented by Ghosh et al. (2022). These authors claim, based on rather short *Swift* XRT observations, that the soft excess disappeared during 2016, and that it is uncorrelated with the UV emission. In particular, for *Swift* XRT data taken just seven days after our January 2021 *XMM–Newton* observation, they find a soft excess flux $F_{\rm BB} < 0.8 \times 10^{-13}$ erg cm^{-2} s^{-1}. This upper limit is a factor ~ 8 lower than our measured $F_{\rm BB}$ for January 2021. We investigate this discrepancy in Appendix C, and find that it is due to (a) the larger modelling uncertainties when using short *Swift* XRT observations instead of deep *XMM–Newton* data, and (b) a possible systematic lack of soft X-ray counts in the XRT spectra. We therefore believe that our soft excess detections with *XMM–Newton* (and supported by the *NICER* data) are robust.

A positive correlation between the soft excess and the UV continuum flux (i.e. the disc emission) supports inverse Comptonization of disc seed photons as a production mechanism for the soft excess (Mehdipour et al. 2015, 2023). Conversely, a correlation between the soft excess and the X-ray continuum flux, without any $F_{\rm BB}$–$F_{\rm UV}$ correlation, might support an origin in relativistic reflection (Barua et al. 2023). As the soft excess strength in Mrk 590 correlates with *both* the X-ray and the UV continuum levels, we cannot make similar arguments based on variability data alone. However, our model comparison (Section 3.3) strongly favours models with warm-Comptonized emission over those without. Thus, we argue that most of the observed soft excess in Mrk 590 is warm-Comptonized emission.

The location of the warm Comptonizing region is not constrained by these analyses. Its source of UV seed photons is often assumed to be produced in the inner accretion disc. However, in Mrk 590, the strongest UV response appears to be located ~ 3 light-days from the X-ray source (Paper 1). If the UV source and soft excess regions are co-located, the tight correlations between the UV and X-ray continua and the soft excess flux can be explained by X-ray irradiation producing additional UV seed photons. In that case, we would expect a similar ~ 3-day delay between X-ray continuum and soft excess fluctuations. Alternatively, the warm Comptonizing region may occur physically closer to the X-ray source than the primary UV response; we discuss one possible physical scenario in Section 4.5. Dedicated X-ray timing experiments are needed to test these scenarios.

4.2 Warm-Comptonized emission in the UV

A strong contribution from warm-Comptonized emission will unavoidably affect the shape of the observed UV–optical spectrum. In particular, compared to an initial 'thin disc' seed photon distribution, it flattens the spectral energy distribution by reducing the UV peak luminosity and shifting the emission peak towards higher energies. While we defer a full study of the broad-band spectral energy distribution to future work (Lawther et al. in preparation), it is important to test whether the UV emission is consistent with our X-ray modelling. In particular, while multiple mechanisms may in principle contribute to the UV–optical emission, our model would be ruled out if it *overpredicts* the UV luminosity. We now investigate this using available *Swift* UVOT data.

4.2.1 UVOT data and host galaxy subtraction

We extract sky background-subtracted photometry for individual UVOT observations as detailed in Paper 1. These data contain a substantial contribution from host galaxy starlight, for all epochs presented in this work. We construct an approximate model of the host galaxy emission as follows. Bentz et al. (2009) present a 2D

decomposition of the stellar and AGN emission for Mrk 590, based on high-resolution *Hubble* Space Telescope imaging. They represent the *V*-band stellar emission as three separate Sersic components: two compact 'bulge' components, plus an extended disc. We calculate the relative contribution of these three components within the inner 3' (to match our UVOT extraction aperture). We then co-add the 'bulge' and 'Sa' spectral templates presented by Kinney et al. (1996), scaled in the *V*-band according to the derived Sersic profile ratios. We apply *Synphot* (STScI Development Team 2018) to determine the host galaxy colours in the UVOT filters. Finally we apply the probabilistic flux variation gradient technique (Gianniotis et al. 2022), using all *Swift* variability data obtained since 2017, to estimate the host galaxy flux levels.

Short *Swift* observations were carried out during the *XMM* observations. However, for the LF data set, the contemporaneous UVOT observations are very faint; after subtracting our host galaxy model, we find negative residuals in the *V* and *B* bands. This suggests that we are slightly overestimating the host galaxy emission in *V* and *B*, and/or that these particular UVOT observations suffer flux calibration issues. To avoid biasing our UV modelling for the LF data set due to these negative residuals, we turn to non-contemporaneous data taken at similar X-ray flux levels. We select all observations for which the *Swift* XRT flux satisfies $3.8 \times 10^{-12} < F_{0.3-10} < 6.8 \times 10^{-12}$ erg cm^{-2} s^{-1} for the LF dataset, and $18.8 \times 10^{-12} < F_{0.3-10} < 24.7 \times 10^{-12}$ erg cm^{-2} s^{-1} for HF. This corresponds to the X-ray flux ranges spanned by each data set (Section 3.3.1). In each UVOT filter, we adopt the sample average flux of the flux-matched set, and use the 1σ sample scatter in measured fluxes as the uncertainty. This provides an indication of the typical UV–optical fluxes emitted for each X-ray flux regime (Fig. 13, green crosses). As this 'X-ray flux-matched' approach is non-standard, we also present the contemporaneous UVOT data for LF for comparison purposes.

4.2.2 UV–optical–X-ray modelling

We replace both the power-law continuum and the warm-Comptonized emission components in our distant reflection model (Section 3.3.3) with a single AGNSED (Kubota & Done 2018) component. The resulting model is defined in XSPEC as CONST×TBABS(AGNSED + PEXMON). We allow the constant offsets $C_{\rm inst}$ to differ for each X-ray detector, as before, but require $C_{\rm UVOT} \equiv 1$ as we account for observed UV–optical flux variability in the uncertainties. The AGNSED model assumes that accretion energy is dissipated radially according to the 'thin-disc' prediction, but that the energy release within a radius $R_{\rm hot}$ occurs as hot-Comptonized emission to produce the X-ray continuum. Thus, $R_{\rm hot}$ is effectively the size of the hot corona. For radii $R_{\rm hot} < R < R_{\rm warm}$, the energy is released as warm-Comptonized emission, while for $R_{\rm warm} < R < R_{\rm out}$, 'thin-disc' thermal emission is observed without any reprocessing. Thus, AGNSED calculates the emission from an inner corona, an intermediate warm-Comptonizing region, and an outer thin disc, in an energetically consistent way. The PEXMON component accounts for the distant reflection features, as before. We do not include any relativistic reflection component here, as it is not formally required by the X-ray data (Section 3.3.4). For this preliminary analysis of the optical–UV emission, we hold several AGNSED parameters constant at their default values, as we only aim to test whether warm Comptonization is in broad agreement with the observed spectral energy distribution shape. In particular, we adopt a disc inclination angle $i = 38^\circ$ as derived from our X-ray modelling, and assume zero black hole spin. We assume a black hole mass of 3.7×10^7 $M_\odot$ (Peterson et al. 2004). We use the PYXSPEC Monte Carlo Markov Chain implementation to explore the parameter space, with a chain length of 300,000, and optimize the model starting at the posterior median to obtain a final fit. As the UVOT photometry is obtained in imaging mode, we adopt χ^2 statistics for this process, rebinning our X-ray data to a minimum of 25 counts per bin.

4.2.3 SED modelling results

The LF data set has an accretion rate of around 0.9 per cent of the Eddington rate, while HF is accreting at around 3 per cent Eddington, according to the AGNSED model. We find $R_{\rm hot} \sim 100$ gravitational radii for all four data sets (LF, HF, J21, and F23). In terms of the assumed AGNSED geometry, this indicates that the inner accretion flow is hot and optically thin; the disc is heavily truncated. In a model-agnostic sense, it simply means that Mrk 590 has a relatively bright primary X-ray continuum compared to the UV, e.g. considering the ensemble UV versus X-ray luminosity relationship for AGN (Lusso & Risaliti 2016). Intriguingly, Krishnan et al. (2024) report a similarly large $R_{\rm hot}$ in the low-flux state of a flaring Seyfert AGN, accreting at ~ 4 per cent of the Eddington rate. They find a compact corona ($R_{\rm hot} \sim 20\ r_g$) for the same source in its high-flux state (~ 10 per cent Eddington). Compact $R_{\rm hot}$ are also reported for Mrk 110 (Porquet et al. 2024a) and ESO 141-G55 (Porquet et al. 2024b), both accreting at roughly 10 per cent of the Eddington rate. As Mrk 590 achieves only 3 per cent Eddington, even in the HF data, our findings are consistent with these results. It appears that the onset of inner-disc formation may occur at $\gtrsim$ 5–10 per cent Eddington; additional X-ray and UV data at higher flux levels are needed to test this explicitly for Mrk 590.

'Pure' warm-Comptonized emission (i.e. $R_{\rm warm} \equiv R_{\rm out}$) provides a better match to the UVOT data than models dominated by a cool outer disc. Because the disc is truncated to power the bright hard X-ray emission, the inner edge of the disc is at $\sim 100\ r_g$, and is thus cooler than a 'standard' disc extending to the innermost stable orbit. Without warm-Comptonized emission, this predicts a spectral turnover in the optical, contrary to our observations. Warm-Comptonized emission peaks in the extreme-UV, which is broadly consistent with the rather flat UVOT spectral energy distributions (Fig. 13). Thus, we suspect that Mrk 590 may lack a standard, unobscured 'thin-disc' component during our observations. We tabulate the best-fitting model parameters, for AGNSED with no cool outer disc, in Table 4. We demonstrate that alternative geometries, e.g. requiring a compact hot region with $R_{\rm hot} = 10$, or replacing the warm Comptonizing region with a standard 'thin disc', do not substantially improve the modelling (Appendix D). While a hybrid model including both warm-Comptonized and thin-disc emission can roughly match the UV flux levels (Appendix D), the best-fitting solutions are dominated by the warm-Comptonized emission at the energies probed590 during 2018. by UVOT.

The overall UV–optical fluxes are matched to first order by the AGNSED model for the HF, J21 and F23 data. Meanwhile, for the LF data set, the model underestimates the observed UV flux (Fig. 13, top left). While this does not exclude the warm-Comptonization scenario, it would mean that an additional source of UV emission is required in the low-flux state. It is unclear whether this represents the onset of a real physical change at the lowest flux levels, or is due to our use of non-contemporaneous UVOT data to construct the low-state SED. For comparison purposes, we present AGNSED modelling of LF based on contemporaneous UVOT data in Fig. 14. While the *V*- and

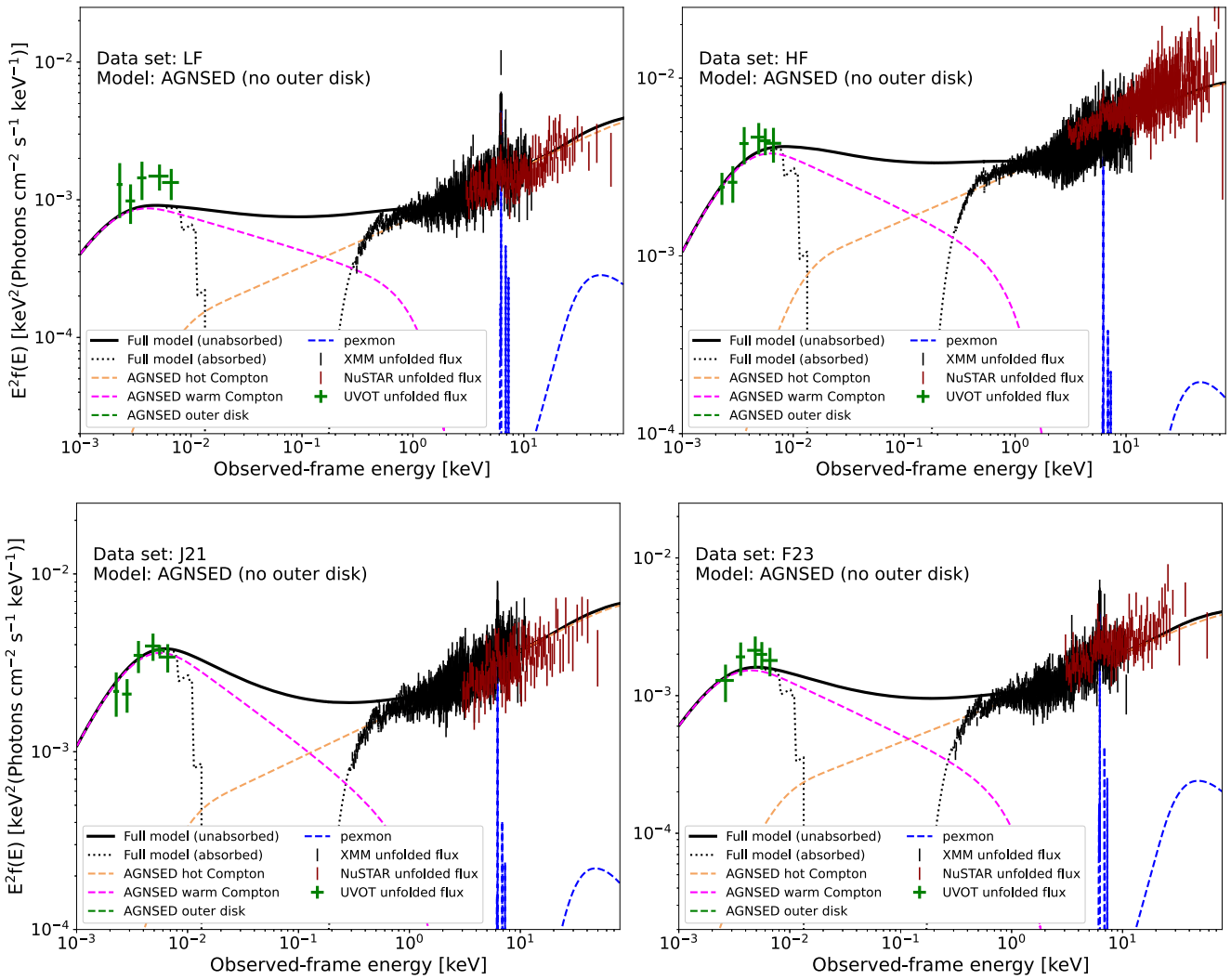

Figure 13. AGNSED models to the optical–UV–X-ray spectral energy distributions for the LF, HF, J21, and F23 data sets. The UVOT data points represent average flux levels for observations taken within the appropriate X-ray flux regime; see the main text (Section 4.2) for details. Here, we impose $R_{\rm warm} = R_{\rm out}$, such that no outer 'thin-disc' emission is produced. We note that the model curves in these figures (black curves) are normalized to the *XMM–Newton pn* spectra. As there are substantial flux offsets between *XMM–Newton* and *NuSTAR* in these combined data sets (Section 3.3.1), the *NuSTAR* spectra appear offset from the model curves in this unfolded presentation; these offsets are accounted for in the underlying modelling. We present alternative configurations of the AGNSED model (i.e. including a cool disc; excluding warm Comptonization; limiting the size of the hot corona; imposing a lower temperature for the hot corona) in Appendix D.

B-band upper limits (likely affected by host galaxy over-subtraction) cannot be reconciled with the AGNSED model, the UV bands are broadly consistent with it. An improved host galaxy model is needed to fully test the warm-Comptonization scenario for the LF data, as the SED modelling is more sensitive to over-subtraction issues at low AGN flux levels. We note that the F23 data set is successfully modelled by AGNSED with no outer disc (Fig. 13, bottom right). This suggests that warm Comptonization is the main UV–optical emission mechanism at X-ray flux levels down to at least $F_{0.3-10} \sim 6 \times 10^{-12}$ erg cm^{-2} s^{-1}.

The AGNSED modelling yields softer photon indices for the warm-Comptonized emission ($\Gamma_{\rm warm} \sim 2.3$), compared to our X-ray analysis ($\Gamma_{\rm warm} \sim 1.9$). This distinction is important, as $\Gamma_{\rm warm} \lesssim 2$ likely requires both a non-dissipative underlying disc, and a patchy, low covering fraction atmosphere (Petrucci et al. 2018). However, we cannot fully exclude $\Gamma_{\rm warm} < 2$ based on our UVOT data, given the substantial uncertainties (Table 4). We will present additional spectroscopic observations, to robustly test this and alternative scenarios, in upcoming work (Lawther et al., in preparation).

4.3 Is the X-ray reflector Compton-thin?

An exponential cut-off in the primary continuum is warranted for all four joint data sets according to our model comparison (3.3). However, we find that replacing the cut-off power law with a NTHCOMP component is strongly disfavoured in terms of Bayes factors (Appendix B3). This is unexpected if the observed continuum is indeed due to a hot Comptonizing 'corona' region, as typically assumed. Also, the cut-off power law does not fully capture the spectral curvature at 30–50 keV for the LF data (Fig. 9). An alternative explanation is that the assumption of Compton-thick

Table 4. Best-fitting parameters for the optical–UV–X-ray model, AGNSED.

Row	Parameter	LF	HF	J21	F23
(1)	$N_{\rm H,Gal}$	2.77×10^{20}	2.77×10^{20}	2.77×10^{20}	2.77×10^{20}
(2)	Z	1	1	1	1
(3)	$A_{\rm Fe}$	$6.9^{+9.0}_{-3.3}$	6.9	6.9	6.9
(4)	z	0.026385	0.026385	0.026385	0.026385
	AGNSED				
(5)	$M_{\rm BH}$	3.7×10^{7}	3.7×10^{7}	3.7×10^{7}	3.7×10^{7}
(6)	D	112	112	112	112
(7)	$\log(\dot{m})$	-2.05 ± 0.06	-1.57 ± 0.01	-1.72 ± 0.02	-1.99 ± 0.04
(8)	a_*	0	0	0	0
(9)	$\cos(i)$	0.788	0.788	0.788	0.788
(10)	$kT_{\rm hot}$	300	300	300	300
(11)	$kT_{\rm warm}$	0.25 ± 0.02	0.25 ± 0.03	0.30 ± 0.03	0.26 ± 0.03
(12)	$\Gamma_{\rm hot}$	1.65 ± 0.06	1.73 ± 0.03	1.70 ± 0.03	1.68 ± 0.09
(13)	$\Gamma_{\rm warm}$	2.23 ± 0.32	2.29 ± 0.39	2.45 ± 0.16	2.38 ± 0.30
(14)	$R_{\rm hot}$	168 ± 35	124 ± 47	104 ± 8	127 ± 24
(15)	$R_{\rm warm}$	$4.7(\pm2.8)\times10^{4}$	$5.7(\pm2.6)\times10^{4}$	$4.3(\pm2.9)\times10^{4}$	$6.0(\pm2.8)\times10^{4}$
(16)	$\log R_{\rm out}$	$\equiv R_{\rm warm}$	$\equiv R_{\rm warm}$	$\equiv R_{\rm warm}$	$\equiv R_{\rm warm}$
(17)	$h_{\rm max}$	10	10	10	10
	PEXMON				
(18)	$\rm N_{cont}$	$3.4(\pm1.0)\times10^{-4}$	$4.2(\pm4.0)\times10^{-4}$	$(5.5\pm1.1)\times10^{-4}$	$(3.8^{+8.2}_{-3.8})\times10^{-4}$
	Instrumental				
(19)	$C_{\rm MOS1}$	1.03 ± 0.01	1.05 ± 0.01	0.99 ± 0.01	1.01 ± 0.01
(20)	$C_{\rm MOS2}$	1.04 ± 0.01	1.03 ± 0.01	0.99 ± 0.01	1.03 ± 0.01
(21)	$C_{\rm FPMA}$	0.89 ± 0.04	1.18 ± 0.06	0.84 ± 0.01	1.14 ± 0.01
(22)	$C_{\rm FPMB}$	0.90 ± 0.03	1.20 ± 0.03	0.87 ± 0.01	1.17 ± 0.01
(23)	$C_{\rm UVOT}$	1	1	1	1

Note. Best-fitting parameters for our optical–UV–X-ray model based on AGNSED (Section 4.2), for the low-flux (LF) and high-flux (HF) data sets. The uncertainties correspond to 1σ intervals derived from the Markov chain Monte Carlo posterior distributions. Parameters listed in grey are held constant during the model fit procedure. (1) Column density for Galactic absorption, units of $\rm cm^{-2}$. (2) Metallicity relative to Solar. (3) Iron abundance relative to Solar. (4) Source redshift. (5) Black hole mass in units of Solar mass, as estimated via reverberation mapping (Peterson et al. 2004). (6) Co-moving distance in Mpc; as the redshift is small ($z = 0.026385$) we set this to the luminosity distance. (7) Mass accretion rate, scaled by the Eddington accretion rate. (8) Black hole rotation parameter. (9) Inclination angle; here, we constrain the AGNSED and PEXMON inclinations to the best-fitting value from our X-ray analysis. (10) Electron temperature in the hot Comptonizing region, units of keV. (11) Electron temperature in the warm Comptonizing region. (12) Photon index for hot Comptonized emission. (13) Photon index for warm Comptonized emission. (14) Radius of the hot Comptonization region, in units of the gravitational radius r_g. (15) Radius of the warm Comptonization region. (16) Outer radius; for this model we do not include an outer disc, so it is equal to $R_{\rm warm}$. (19) Height above the disc of the 'lamp-post' X-ray source that irradiates the disc. We set this to 10 r_g, as for the disc reflection model in our X-ray analysis. (18) Incident continuum normalization for the distant reflection component. For the optical–UV–X-ray modelling, as we are mainly interested in the overall spectral energy distribution, we set the PEXMON reflection strength to $R = -1$ and use $N_{\rm cont}$ to scale the reflection spectrum. (19–23) Instrumental scaling factors relative to *XMM–Newton pn*. We set $C_{\rm UVOT} \equiv 1$, as we are testing whether the overall UV flux level can be reproduced by the soft excess model; allowing for UV to X-ray flux offsets would defeat this purpose. Instead, our use of averaged UVOT photometry should minimize the influence of luminosity variability.

reflection might be incorrect. In that case, our preferred models would over-predict the Compton hump (for a given reflection factor R). This could then be ameliorated to first order by inclusion of a high-energy cut-off, even if the true continuum is power law-like over the observed energy range. To test this, we replace the PEXMON component with a BORUS02 component (Baloković et al. 2018), which approximates a torus geometry, and includes the column density of the reflection region as an additional parameter. We include this variant in our Bayesian comparison (Appendix B); it is acceptable for three data sets (LF, HF and J21). It is disfavoured for F23, but this may be due to signal-to-noise issues: F23 has the least total X-ray counts. Using the BORUS02 model, we find column densities of order 10^{23} $\rm cm^{-2}$, which indeed produces a weaker Compton hump than does a Compton-thick reflector (Fig. 15). We find this interpretation plausible, given that a cut-off power-law spectrum is not physically motivated. Diaz et al. (2023) find a weak trend for low-luminosity AGN to display Compton-thin reflection, perhaps because they tend to be more gas-starved, as explored below. Alternatively, additional reflection from Compton-thin BLR clouds would produce substantial iron line emission while only contributing weakly to the Compton hump (Patrick et al. 2012). Assuming Keplerian rotation, the narrow Fe K width implies a radius of at least three light-days for the distant reflector (Section 3.2). This is fully consistent with reflection in the BLR: Mandal et al. (2021) estimate a BLR size of ~ 20 d for Mrk 590 during 2018.

4.4 Hints of a gas-starved nucleus

Denney et al. (2014) reported a negligible level of intrinsic absorption upon their discovery of the initial 'turn-off' event. Our model comparison confirms that the X-ray source in Mrk 590 is largely

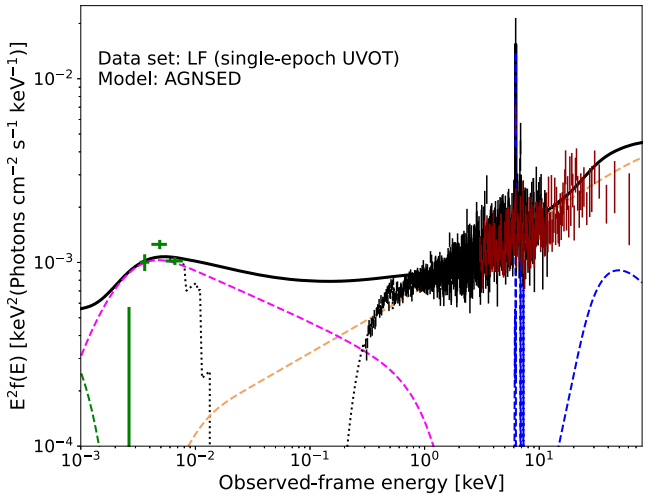

Figure 14. An alternative spectral energy distribution for the LF data set, using a 2 ks contemporaneous UVOT observation. Unfortunately, our host galaxy model oversubtracts the *B*- and *V*-band flux: here, we show 3σ statistical upper limits, which are inconsistent with the best-fitting warm Comptonization component. However, the *U* and far-UV bands are well-modelled by warm Comptonization. An improved host galaxy model is required to fully test the warm-Comptonization scenario at the lowest observed flux levels; we will address this in future work.

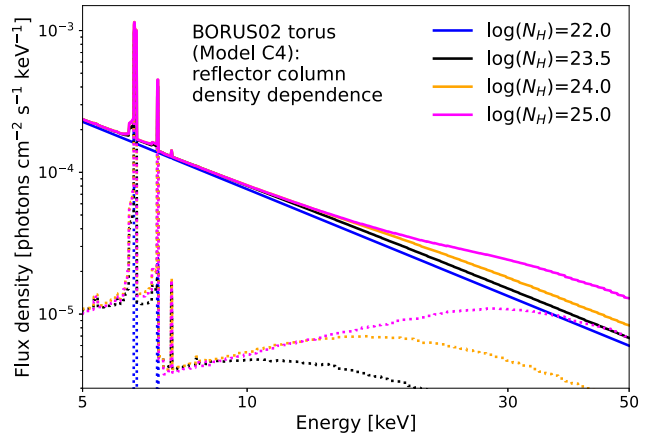

Figure 15. Dependence of a model including variable-density torus reflection component (BORUS02), on the column density of the reflecting material. The solid lines illustrate the full model; dotted lines correspond to the reflection component only. For $\log(N_{\rm H}) \leq 23$, the hard X-ray Compton reflection hump is negligible. This is one possible explanation for the rather weak Compton reflection feature seen for Mrk 590, where models with a Compton-thick reflection component overestimate the hard X-ray flux (e.g. Fig. B1).

unabsorbed, at all observed continuum flux levels, over ~ 20 yr of *XMM–Newton* observations. To constrain how much intrinsic absorption might still be present, we fit a model including an intrinsic neutral absorber to the HF and LF data sets. We find an intrinsic column density of 7.9 ($\pm$9.1) $\times$ 10^{19} cm^{-2}) for HF and 1.1 ($\pm$0.9) $\times$ 10^{20} cm^{-2}) for LF. Thus, Mrk 590 can essentially be classified as a 'bare' AGN, defined by Nandi et al. (2023) as sources with intrinsic column densities below 10^{20} cm^{-2}.

While these constraints only directly apply to measurements along our line-of-sight, we note a few other indications that the central engine of Mrk 590 may be gas poor. (1) Mrk 590 displays an unusually strong (for AGN) UV response to X-ray variability (Paper 1); this suggests unobscured sight-lines between the X-ray continuum and the reprocessor. (2) While we see clear evidence of X-ray reflection, the reflector may be Compton-thin (Section 4.3). (3) Molecular gas is not detected in the inner ~ 100 pc nucleus of Mrk 590, although the derived upper limit is 10^5 $M_\odot$, in principle sufficient to power the AGN for thousands of years (Koay et al. 2016). While inconclusive, our findings are *consistent* with a scenario where the nucleus is gas-poor compared to typical Seyfert AGN. Ricci et al. (2022) posit an evolutionary scenario where young AGN reside in gas-rich nuclei, displaying strong absorption along any line of sight. They then enter a'blow-out' phase at high Eddington ratios, becoming bright, unabsorbed sources (unless the line of sight goes through the accretion flow, in which case a Type 2 AGN is observed). The later stage of the AGN lifetime is then gas-starved; the continuum luminosity dims due to reduced accretion rate, and the accretion flow itself becomes Compton-thin. Our findings so far are consistent with such a scenario.

4.5 The inner accretion flow of Mrk 590

We find warm-Comptonized emission in Mrk 590 in both the low- and high-flux states (Section 3.3), and demonstrate that this emission component may be responsible for most or all of the UV–optical flux (Section 4.2). Meanwhile, any inner-disc reflection is fairly weak, and (if present) occurs in a highly ionized reflective region. Here, we explore a scenario originally suggested by Petrucci et al. (2013), for the Type 1 AGN Mrk 509, that can potentially explain these observables. In this scenario, the thin accretion disc is covered by an optically thick 'atmosphere' (Haardt & Maraschi 1993; Janiuk, Czerny & Madejski 2001; O'Brien et al. 2001), and some of the accretion energy is dissipated directly into the atmosphere (Petrucci et al. 2020; Ballantyne et al. 2024; Palit et al. 2024). The underlying disc is both irradiated by the atmosphere, and provides a source of seed photons. The energy balance of this disc–atmosphere system is likely accretion rate-dependent. In particular, if magnetic fields support the disc, an increasing fraction of the accretion energy is dissipated in the atmosphere at lower accretion rates (Begelman et al. 2015). In that case, a largely passive disc with a dissipative atmosphere occurs at low-intermediate accretion rates. A full transition into a 'puffed-up', radiatively inefficient advective state is predicted if the accretion slows further. We speculate that Mrk 590 may be in just such an intermediate state during our observations.

For a plane-parallel 'sandwich' geometry of a warm-Comptonizing atmosphere above and below a thermal disc, the photon index $\Gamma_{\rm warm}$ and electron temperature kT_e serve as diagnostics of the disc–atmosphere energy balance. In particular, $\Gamma_{\rm warm} \sim 2$ indicates a passive underlying disc (Petrucci et al. 2020). While we find $\Gamma_{\rm warm} \sim 1.9 \pm 0.2$ for the LF data set, considering only the X-ray observations, we find $\Gamma_{\rm warm} \sim 2.3 \pm 0.3$ when we include the UVOT data (Section 4.2). Although both measurements are consistent with $\Gamma_{\rm warm} \sim 2$ given their substantial uncertainties, the optical–UV–X-ray data sets are more sensitive to the overall shape of the warm-Comptonized emission. Thus, we cannot strongly constrain the dissipative balance of the disc.

Any relativistic reflection from a warm-Comptonizing disc atmosphere would be highly ionized, with $\log(\xi) \sim 3$ (Janiuk et al. 2001), in agreement with our dual reflection region model fits (Section 3.3). Also, the $\sim$ 3-day delayed UV response to X-ray flares (Paper 1) may be compatible with this scenario: an optically thick atmosphere with $kT \sim 0.3$ keV would presumably partially obscure

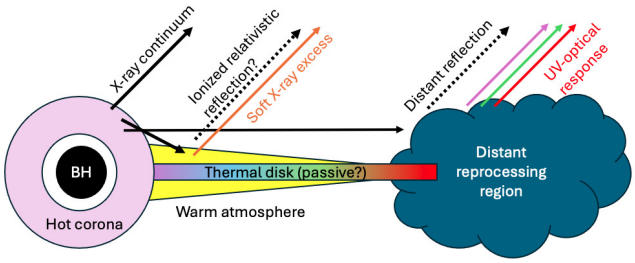

Figure 16. Possible arrangement of the emission regions in Mrk 590 during the flaring episodes since 2017, inspired by the 'passive disc' scenarios invoked by Petrucci et al. (2018, 2020), Ballantyne et al. (2024), and Palit et al. (2024). For Mrk 590, the bright X-ray emission (relative to the UV) requires that a substantial fraction of the accretion energy is released in the form of hot-Comptonized emission, here represented by a hot corona extending to $\sim 100 r_g$ (based on the energetic assumptions of the AGNSED model, Section 4.2). The warm-Comptonized emission is then produced in an extended, optically thick disc atmosphere, which reprocesses seed photons form an underlying thermal disc. As the thermal disc is obscured by this optically thick atmosphere out to $\sim 10^5 r_g$ (Section 4.2), and/or truncated at the inner edge due to the large corona, it does not produce a prompt UV response to X-ray illumination. Instead, the UV response may be dominated by a 'pure reprocessing' component emitted at larger radii. This may explain both the 3-d X-ray to UV delay (Paper 1), and the unusually (for AGN) coherent UV response to X-ray variability. We note that our analyses do not constrain the shape, size or orientation of the distant reprocessor. Nor do they demand that the hot corona be spherically symmetric, as opposed to, e.g. a 'lamp-post' geometry, perhaps related to jet processes.

the underlying disc from X-ray illumination, and in any case would alter its wavelength-dependent response. Much of the observed UV response might then occur in surrounding dense gas, such as a heavily truncated outer disc (if present), broad line-emitting region, or the inner edge of the larger-scale accretion flow. We illustrate one possible 'toy model' geometry in Fig. 16, but note that the nature of the putative distant reprocessor is highly speculative. We aim to address these issues in future work, harnessing both improved optical–UV wavelength coverage and high-cadence timing data.

4.6 The diverse X-ray behaviours of CLAGN

Mrk 590 displays no intrinsic absorption (Section 4.4); its changing-look behaviour must therefore be due to intrinsic variability. Here, we compare its observed X-ray behaviour with other 'changing-state' sources. We note that the observations presented here capture Mrk 590 in epochs with and without optical broad emission lines (Denney et al. 2014; Raimundo et al. 2019; Lawther et al. in preparation), thus probing both 'turned-off' and 'turned-on' states. It is remarkable that the overall X-ray spectral shape does not vary strongly. The 6.4 keV emission lines do display a smaller equivalent width at high luminosities, as expected for flaring activity, given their origin in distant reprocessing material (Section 3.3.2). However, the overall spectral shape varies only mildly, as evidenced by the linear $F_{0.3-10}$–$F_{\rm BB}$ relationship and the weak dependence of Γ on $F_{0.3-10}$ (Section 3.2). To investigate the long-term evolution, we highlight measurements derived from the *XMM–Newton* observations in 2002 and 2004 (blue squares in Figs 4–7). These measurements largely follow the overall observed trends. Thus, Mrk 590 displayed similar X-ray behaviour even before the first discovered 'turn-off' event. A similarly constant X-ray spectral shape is observed in the CLAGN LEDA 1 154 204 (Saha et al. 2023) and IRAS 23226–3843 (Kollatschny et al. 2023), despite X-ray variability by factors of ~ 17 and ~ 10, respectively.

This is a marked contrast to the changing-look AGN 1ES 1927 + 654, for which the X-ray continuum disappears in low-luminosity states, with only the soft excess remaining (Ricci et al. 2020). Those authors attribute the apparent disappearance of the continuum to a rapid cooling of the hot X-ray corona. Conversely, Noda & Done (2018) report the disappearance of the soft excess component (but not the hard continuum) in the CLAGN Mrk 1018 as it enters the 'turn-off' state. They interpret this as evidence for a transition of the accretion flow into an ADAF state; Veronese et al. (2024) suggest that this transition is linked to a disturbance in the inner disc, with subsequent jet production. Clearly, some individual CLAGN undergo drastic X-ray evolution, which is not seen in Mrk 590. We note that UV–optical CLAGN are essentially defined by the *response* of the broad-line region to changes in the ionizing continuum. The variety of X-ray behaviours observed for different CLAGN suggests that several distinct physical mechanisms in the innermost regions can lead to UV–optical changing look events.

5 CONCLUSION

The CLAGN Mrk 590 displayed repeating strong X-ray flares during 2017–2024. We capture the X-ray spectrum several times during this flaring behaviour, and supplement these data with archival X-ray observations (2002–2016) to build a comprehensive record of its X-ray behaviour. We analyse these data both as individual 'snapshots' and as combined, multi-instrument data sets. Our findings are as follows.

(i) Soft X-ray excess is detected at all flux levels. This component displays a tight correlation with both the X-ray and the UV continuum emission from the AGN. Warm Comptonization of UV seed photons is strongly favoured over inner-disc reflection as the source of the soft excess. We confirm that a warm Comptonizing region covering most of the accretion flow, out to $\sim 10^5 r_g$, is broadly consistent with the observed optical–UV emission.

(ii) Iron K emission lines are present at both low and high continuum flux levels, although their fluxes cannot be constrained in some individual 'snapshot' observations due to poor statistics. The iron emission is dominated by distant reprocessing. Some relativistic reflection may be present, but is not formally required. The relativistic reflecting medium, if present, must be highly ionized.

(iii) Mrk 590 displays very little obscuration in any of our observations. It may harbour a Compton-thin outer accretion flow, as supported by the faintness of the observed high-energy reflection hump. Furthermore, the outer accretion flow is likely directly irradiated by the X-ray continuum, given the strong and delayed UV response (Paper 1), which suggests a lack of absorbing material in the central engine. Considering also the intermittent accretion activity, we speculate that the nucleus may be gas starved to some degree.

(iv) The X-ray spectral shape appears roughly constant as a function of continuum flux. Mrk 590 displays neither a disappearing soft excess (as observed for the CLAGN Mrk 1018) or hard continuum (as for the CLAGN 1ES 1927 + 654). The variety of X-ray behaviours observed among known CLAGN suggests that several distinct physical mechanisms may produce the observed UV–optical CLAGN phenomenon.

(v) The optical–UV data are broadly consistent with a warm-Comptonized emission component, with no direct emission from a thermal 'thin-disc' required by the data. Due to host galaxy subtraction issues, this result is less robust at the lowest flux levels observed; however, as our X-ray model comparison strongly favours

a warm-Comptonized component at all flux levels, it is likely present in all our data. We suggest a scenario where much of the accretion energy is dissipated in a warm, optically thick disc atmosphere. The seed photons for the Comptonized emission would then be produced in an underlying disc, which may be largely passive, heated radiatively by its atmosphere. This is compatible with our finding of weak inner-disc reflection from a highly ionized medium. It also explains the ∼3-d delayed X-ray to UV response observed during recent flaring episodes: if the inner disc is obscured by an optically thick plasma, the strongest UV response to X-ray illumination may occur in more distant reprocessing regions.

In future work, we will explore these scenarios by way of (i) an in-depth study of the evolution of the optical–UV–X-ray spectral energy distribution since 2012, (ii) further timing experiments, currently in-progress, to determine the geometry of the inner regions of Mrk 590.

ACKNOWLEDGEMENTS

We thank the referee for a thoughtful and useful report that improved the quality of this work; in particular for their suggestions regarding inclusion of the UV data. We are grateful to Giovanni Minuitti and coworkers for granting us early access to the *XMM–Newton* spectra observed during 2020–2021, and for guidance on our observing strategy for subsequent observations. We thank Thomas Dauser for guidance regarding the various RELXILL model variants, and Aya Kubota for feedback on AGNSED parameter limits. Much of the analysis presented in this paper relies on the HEASOFT, FTOOLS, and XSPEC software packages and related online resources. Daniel Lawther acknowledges financial support from the National Aeronautics and Spasce Administration (NASA) through Guest Observer proposals 8233/21-NUSTAR21-0025, 6238/19-NUSTAR19-0028, 5252/18-NUSTAR18-0042, and 5167/21-NICER21-0015. Sandra Raimundo acknowledges support from the Science and Technology Facilities Council (STFC) of the UK Research and Innovation via grant reference ST/Y002644/1. This work was supported by the Independent Research Fund Denmark via grants DFF-4002-00275 and DFF-8021-0013 and the Carlsberg Foundation via grant CF21-0649.

DATA AVAILABILITY

The astronomical observations studied here are available from NASA's HEASArc archive; the tools used to process and analyse the data, as described in the text, are all freely available. Ancillary code used to produce figures, etc., is available from DL on request.

REFERENCES

Antonucci R., 2015, preprint (arXiv:1501.02001)
Arnaud K. A., 1996, in Jacoby G. H., Barnes J., eds, ASP Conf. Ser.Vol. 101, Astronomical Data Analysis Software and Systems V. Astron. Soc. Pac., San Francisco, p. 17
Ballantyne D. R. et al., 2024, MNRAS, 530, 1603
Baloković M. et al., 2018, ApJ, 854, 42
Barr P., Mushotzky R. F., 1986, Nature, 320, 421
Barua S., Adegoke O. K., Misra R., Pawar P., Jithesh V., Medhi B. J., 2023, ApJ, 958, 46
Begelman M. C., Armitage P. J., Reynolds C. S., 2015, ApJ, 809, 118
Bentz M. C., Peterson B. M., Netzer H., Pogge R. W., Vestergaard M., 2009, ApJ, 697, 160
Bhayani S., Nandra K., 2011, MNRAS, 416, 629
Bianchi S., Guainazzi M., Matt G., Fonseca Bonilla N., Ponti G., 2009, A&A, 495, 421
Buchner J., 2016, Stat. Comput., 26, 383
Buchner J., 2019, PASP, 131, 108005
Buchner J., Boorman P., 2023, C. Bambi A. Santangelo, Handbook of X-ray and Gamma-ray Astrophysics, Springer Singapore
Buchner J. et al., 2014, A&A, 564, A125
Burrows D. N. et al., 2005, Space Sci. Rev., 120, 165
Cackett E. M., Horne K., Winkler H., 2007, MNRAS, 380, 669
Cash W., 1979, ApJ, 228, 939
Chalise S., Lohfink A. M., Chauhan J., Russell T. D., Buisson D. J. K., Mallick L., 2022, MNRAS, 517, 4788
Chanchaiworawit K., Sarajedini V., 2024, ApJ, 969, 131
Crummy J., Fabian A. C., Gallo L., Ross R. R., 2006, MNRAS, 365, 1067
Czerny B., Elvis M., 1987, ApJ, 321, 305
Dauser T., Garcia J., Parker M. L., Fabian A. C., Wilms J., 2014, MNRAS, 444, L100
Dauser T., García J. A., Joyce A., Lickleder S., Connors R. M. T., Ingram A., Reynolds C. S., Wilms J., 2022, MNRAS, 514, 3965
Denney K. D. et al., 2014, ApJ, 796, 134
Diaz Y. et al., 2023, A&A, 669, A114
Done C., Davis S. W., Jin C., Blaes O., Ward M., 2012, MNRAS, 420, 1848
Edelson R. et al., 2019, ApJ, 870, 123
Elvis M. et al., 1994, ApJS, 95, 1
Fabian A. C., Rees M. J., Stella L., White N. E., 1989, MNRAS, 238, 729
Fabian A. C. et al., 2009, Nature, 459, 540
Fabian A. C., Lohfink A., Kara E., Parker M. L., Vasudevan R., Reynolds C. S., 2015, MNRAS, 451, 4375
García J. et al., 2014, ApJ, 782, 76
García J. A., Steiner J. F., McClintock J. E., Remillard R. A., Grinberg V., Dauser T., 2015, ApJ, 813, 84
García J. A., Kallman T. R., Bautista M., Mendoza C., Deprince J., Palmeri P., Quinet P., 2018, in Workshop on Astrophysical Opacities, ASP Conference Series, Vol. 515. p. 282
García J. A. et al., 2019, ApJ, 871, 88
Gendreau K. C. et al., 2016, in den Herder J.-W. A., Takahashi T., Bautz M., eds, Proc. SPIE Conf. Ser.Vol. 9905, Space Telescopes and Instrumentation 2016: Ultraviolet to Gamma Ray. SPIE, Bellingham, p.99051H
Ghosh R., Laha S., Deshmukh K., Bhalerao V., Dewangan G. C., Chatterjee R., 2022, ApJ, 937, 31
Gianniotis N., Pozo Nuñez F., Polsterer K. L., 2022, A&A, 657, A126
Gianolli V. E. et al., 2023, MNRAS, 523, 4468
Grupe D., Beuermann K., Thomas H. C., Mannheim K., Fink H. H., 1998, A&A, 330, 25
Guilbert P. W., Fabian A. C., Rees M. J., 1983, MNRAS, 205, 593
Gunderson S. J., Huenemoerder D. P., 2025, AJ, 169, 2
Guo H., Barth A. J., Wang S., 2022, ApJ, 940, 20
HI4PI Collaboration et al., 2016, A&A, 594, A116
Haardt F., Maraschi L., 1993, ApJ, 413, 507
Hagen S., Done C., 2023, MNRAS, 521, 251
Harrison F. A. et al., 2013, ApJ, 770, 103
Harrison F. A. et al., 2016, ApJ, 831, 185
Humphrey P. J., Liu W., Buote D. A., 2009, ApJ, 693, 822
Ingram A. et al., 2023, MNRAS, 525, 5437
Iwasawa K., Taniguchi Y., 1993, ApJ, 413, L15
Janiuk A., Czerny B., Madejski G. M., 2001, ApJ, 557, 408
Jiang Y.-F., Blaes O., 2020, ApJ 900 1, id.25
Jiang J. et al., 2018, MNRAS, 477, 3711
Kaastra J. S., 2017, A&A, 605, A51
Kara E. et al., 2015, MNRAS, 449, 234
Kass R. E., Raftery A. E., 1995, Journal of the American Statistical Association, 90, 773
Kelly B. C., Bechtold J., Siemiginowska A., 2009, ApJ, 698, 895
Kinney A. L., Calzetti D., Bohlin R. C., McQuade K., Storchi-Bergmann T., Schmitt H. R., 1996, ApJ, 467, 38
Koay J. Y., Vestergaard M., Casasola V., Lawther D., Peterson B. M., 2016, MNRAS, 455, 2745
Kollatschny W. et al., 2023, A&A, 670, A103

Krishnan S. et al., 2024, A&A, 691, A102
Kubota A., Done C., 2018, MNRAS, 480, 1247
LaMassa S. M. et al., 2015, ApJ, 800, 144
LaMassa S. M., Yaqoob T., Kilgard R., 2017, ApJ, 840, 11
Laor A., Fiore F., Elvis M., Wilkes B. J., McDowell J. C., 1997, ApJ, 477, 93
Lawrence A., 2018, Nat. Astron., 2, 102
Lawther D., Vestergaard M., Raimundo S., Koay J. Y., Peterson B. M., Fan X., Grupe D., Mathur S., 2023, MNRAS, 519, 3903(Paper I)
Leighly K. M., 1999, ApJS, 125, 317
Lusso E., Risaliti G., 2016, ApJ, 819, 154
MacLeod C. L. et al., 2016, MNRAS, 457, 389
MacLeod C. L. et al., 2019, ApJ, 874, 8
Madathil-Pottayil A. et al., 2024, MNRAS, 534, 608
Magdziarz P., Zdziarski A. A., 1995, MNRAS, 273, 837
Magdziarz P., Blaes O. M., Zdziarski A. A., Johnson W. N., Smith D. A., 1998, MNRAS, 301, 179
Malkan M. A., 1983, ApJ, 268, 582
Malkan M. A., Sargent W. L. W., 1982, ApJ, 254, 22
Mallick L. et al., 2022, MNRAS, 513, 4361
Mandal A. K. et al., 2021, MNRAS, 508, 5296
Marin F., 2016, MNRAS, 460, 3679
Markwardt C., Arzoumanian Z., Gendreau K., Hare J., 2024, in AAS High Energy Astrophysics Division meeting #21, Bulletin of the American Astronomical Society, vol. 56,id . 105.36
Mason K. O. et al., 2003, ApJ, 582, 95
Mathur S. et al., 2018, ApJ, 866, 123
Mehdipour M. et al., 2015, A&A, 575, A22
Mehdipour M., Kriss G. A., Kaastra J. S., Costantini E., Mao J., 2023, ApJ, 952, L5
Meyer-Hofmeister E., Meyer F., 2011, A&A, 527, A127
Middei R. et al., 2020, A&A, 640, A99
Miller J. M., 2007, ARA&A, 45, 441
Mukherjee P., Parkinson D., Liddle A. R., 2006, ApJ, 638, L51
Mundo S. A. et al., 2020, MNRAS, 496, 2922
Nandi P., Chatterjee A., Jana A., Chakrabarti S. K., Naik S., Safi-Harb S., Chang H.-K., Heyl J., 2023, ApJS, 269, 15
Nandra K., George I. M., Mushotzky R. F., Turner T. J., Yaqoob T., 1997, ApJ, 488, L91
Nandra K., O'Neill P. M., George I. M., Reeves J. N., 2007, MNRAS, 382, 194
Narayan R., Yi I., 1994, ApJ, 428, L13
Noda H., Done C., 2018, MNRAS, 480, 3898
D. Novikov I., S. Thorne K., 1973, in Black Holes (Les Astres Occlus). p.343, DeWitt and B. DeWitt C., Gordon and Breach, N.Y.
O'Brien P. T. et al., 2001, A&A, 365, L122
Pal M., Dewangan G. C., Misra R., Pawar P. K., 2016, MNRAS, 457, 875
Palit B. et al., 2024, A&A 690, id.A308
Patrick A. R., Reeves J. N., Porquet D., Markowitz A. G., Braito V., Lobban A. P., 2012, MNRAS, 426, 2522
Penston M. V., Perez E., 1984, MNRAS, 211, 33P
Peterson B. M. et al., 2004, ApJ, 613, 682
Petrucci P. O. et al., 2004, Nuclear Physics B Proceedings Supplements, 132, 213
Petrucci P. O. et al., 2013, A&A, 549, A73
Petrucci P. O., Ursini F., De Rosa A., Bianchi S., Cappi M., Matt G., Dadina M., Malzac J., 2018, A&A, 611, A59
Petrucci P. O. et al., 2020, A&A, 634, A85
Porquet D., Reeves J. N., 2003, A&A, 408, 119
Porquet D., Hagen S., Grosso N., Lobban A., Reeves J. N., Braito V., Done C., 2024a, A&A, 681, A40
Porquet D., Reeves J. N., Hagen S., Lobban A., Braito V., Grosso N., Marin F., 2024b, A&A, 689, A336
Raimundo S. I., Vestergaard M., Koay J. Y., Lawther D., Casasola V., Peterson B. M., 2019, MNRAS, 486, 123
Reeves J., Done C., Pounds K., Terashima Y., Hayashida K., Anabuki N., Uchino M., Turner M., 2008, MNRAS, 385, L108
Remillard R. A. et al., 2022, AJ, 163, 130
Reynolds C. S., 1999, in Poutanen J., Svensson R., eds, ASP Conf. Ser.Vol. 161, High Energy Processes in Accreting Black Holes. Astron. Soc. Pac., San Francisco, p. 178
Reynolds C. S., Brenneman L. W., Lohfink A. M., Trippe M. L., Miller J. M., Fabian A. C., Nowak M. A., 2012, ApJ, 755, 88
Ricci C., Trakhtenbrot B., 2023, Nat. Astron., 7, 1282
Ricci C., Ueda Y., Paltani S., Ichikawa K., Gandhi P., Awaki H., 2014, MNRAS, 441, 3622
Ricci C. et al., 2020, ApJ, 898, L1
Ricci C. et al., 2022, ApJ, 938, 67
Richards G. T. et al., 2006, ApJS, 166, 470
Ross R. R., Fabian A. C., 2005, MNRAS, 358, 211
Rumbaugh N. et al., 2018, ApJ, 854, 160
Runnoe J. C. et al., 2016, MNRAS, 455, 1691
STScI Development Team, 2018, Astrophysics Source Code Library, record-ascl:1811.001
Saha T. et al., 2023, preprint (arXiv:2309.08956)
Sanders D. B., Phinney E. S., Neugebauer G., Soifer B. T., Matthews K., 1989, ApJ, 347, 29
Scott A. E., Stewart G. C., 2014, MNRAS, 438, 2253
Shakura N. I., Sunyaev R. A., 1973, A&A, 24, 337
Shappee B. J. et al., 2014, ApJ, 788, 48
Shields G. A., 1978, Nature, 272, 706
Siemiginowska A., Kuhn O., Elvis M., Fiore F., McDowell J., Wilkes B. J., 1995, ApJ, 454, 77
Storchi-Bergmann T., Schnorr-Müller A., 2019, Nat. Astron., 3, 48
Strüder L. et al., 2001, A&A, 365, L18
Sunyaev R. A., Titarchuk L. G., 1980, A&A, 86, 121
Tanaka Y. et al., 1995, Nature, 375, 659
Tortosa A., Bianchi S., Marinucci A., Matt G., Petrucci P. O., 2018, A&A, 614, A37
Trotta R., 2007, MNRAS, 378, 72
Tsujimoto M. et al., 2011, A&A, 525, A25
Turner M. J. L. et al., 2001, A&A, 365, L27
Turner T. J. et al., 2002, ApJ, 574, L123
Vanden Berk D. E. et al., 2004, ApJ, 601, 692
Veronese S., Vignali C., Severgnini P., Matzeu G. A., Cignoni M., 2024, A&A, 683, A131
Waddell S. G. H. et al., 2023, A&A 690, id.A132
Walton D. J., Nardini E., Fabian A. C., Gallo L. C., Reis R. C., 2013, MNRAS, 428, 2901
Wu X.-B., Han J. L., 2001, ApJ, 561, L59
Xu Y., García J. A., Walton D. J., Connors R. M. T., Madsen K., Harrison F. A., 2021, ApJ, 913, 13
Yu Z., Jiang J., Bambi C., Gallo L. C., Grupe D., Fabian A. C., Reynolds C. S., Brandt W. N., 2023, MNRAS, 522, 5456
Yuan F., Narayan R., 2014, ARA&A, 52, 529
Zdziarski A. A., Fabian A. C., Nandra K., Celotti A., Rees M. J., Done C., Coppi P. S., Madejski G. M., 1994, MNRAS, 269, L55
Zdziarski A. A., Johnson W. N., Done C., Smith D., McNaron-Brown K., 1995, ApJ, 438, L63
Zdziarski A. A., Johnson W. N., Magdziarz P., 1996, MNRAS, 283, 193
Życki P. T., Done C., Smith D. A., 1999, MNRAS, 309, 561

APPENDIX A: INDIVIDUAL X-RAY SPECTRA

See Figs A1 and A2.

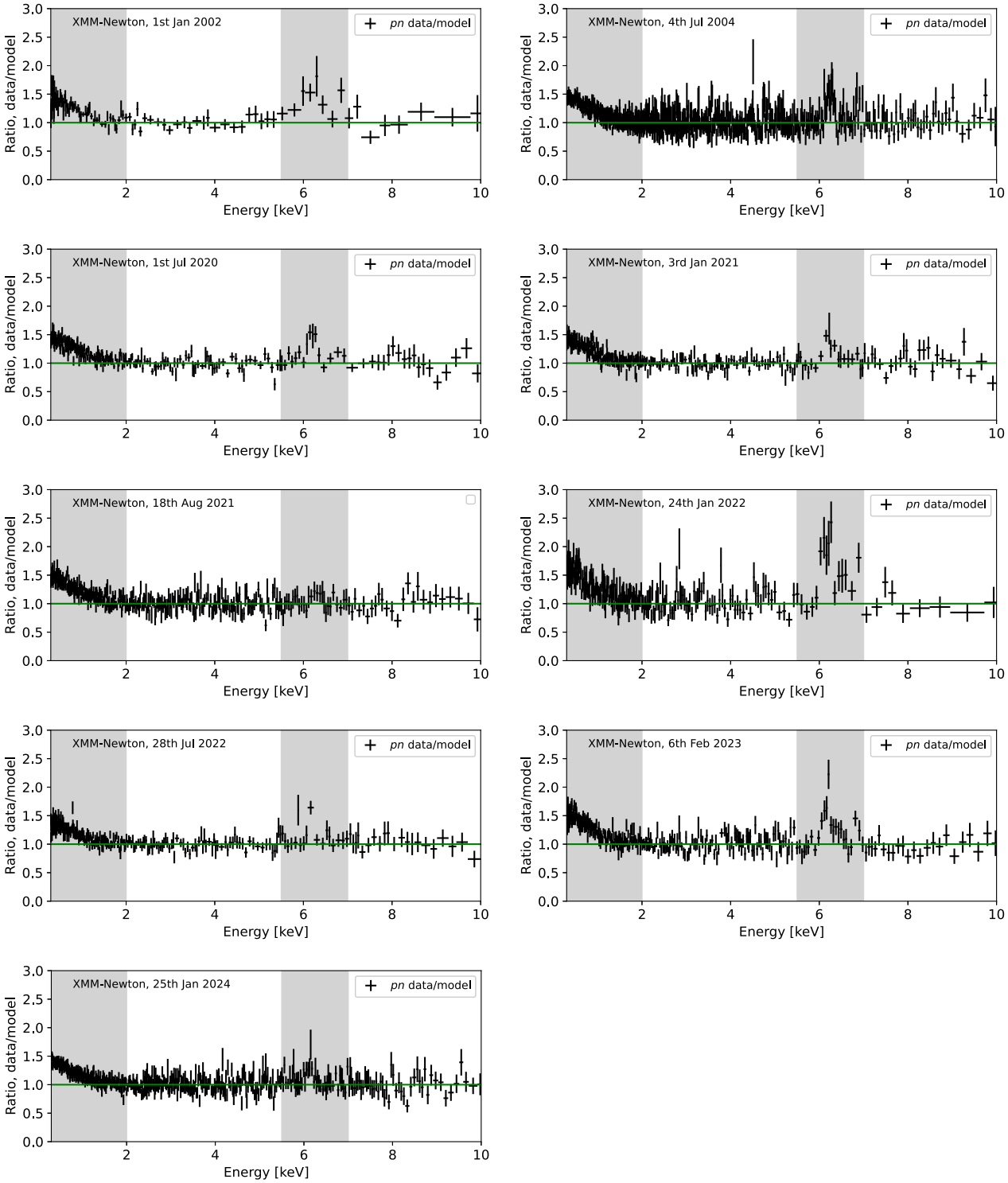

Figure A1. Data-to-model ratios, against a power law model, for individual *XMM–Newton* observations. All energies are given in the observed frame. The grey regions indicate spectral regions excluded from the model fit (Section 3.1). A substantial soft excess above the extrapolated power law model is seen in all spectra. Excess emission near 6.4 keV is robustly detected in most cases, but appears rather weak for 2021 August and 2022 July.

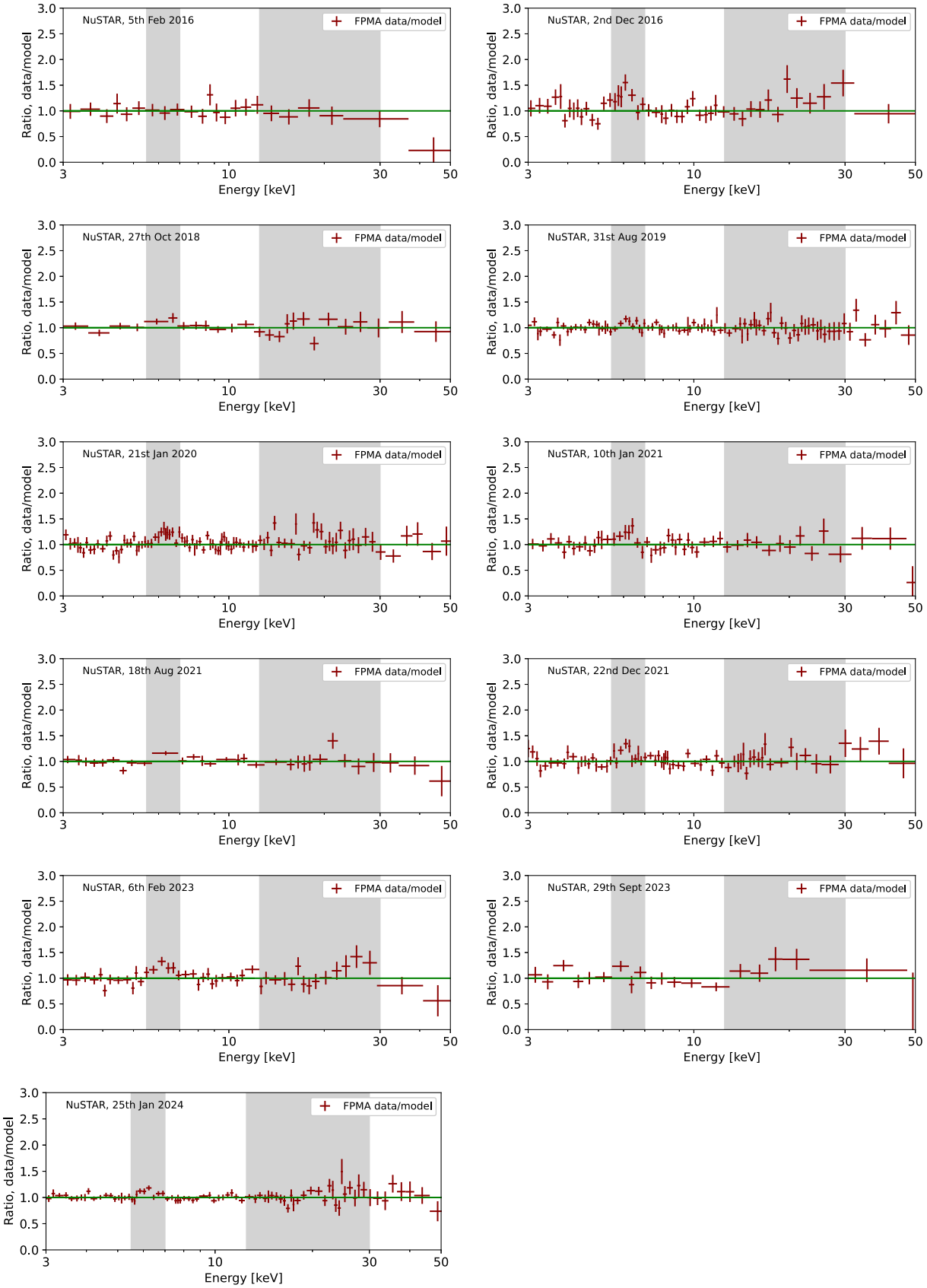

Figure A2. Data-to-model ratios, against a power law model, for individual *NuSTAR* observations. All energies are given in the observed frame. The grey regions indicate spectral regions excluded from the model fit.

APPENDIX B: BAYESIAN MODEL COMPARISON

Here, we detail the model comparison procedure used to arrive at the most suitable models for the HF, LF, J21 and F23 joint data sets (Section 3.3).

B1 Procedure for Bayesian X-ray Analysis

To estimate the evidence Z for each model, we use the Bayesian X-ray Analysis package (BXA, Buchner et al. 2014; Buchner 2019), which runs the *UltraNest* algorithm (Buchner 2016) to sample the full parameter space. BXA calculates the evidence $Z = \int \pi(\boldsymbol{\theta}) \exp(-\frac{1}{2}C(\boldsymbol{\theta}))\mathrm{d}\boldsymbol{\theta}$, where $C(\boldsymbol{\theta})$ is the Cash statistic for a given parameter vector $\boldsymbol{\theta}$, and $\pi(\boldsymbol{\theta})$ is the prior weighting of those particular parameters. $C(\boldsymbol{\theta})$ is calculated via an XSPEC model call. We adopt log-uniform priors for normalization constants and column densities, which may vary over several orders of magnitude, and uniform priors for all other parameters. Thus, $\pi(\boldsymbol{\theta})$ is fully determined by our choice of parameter bounds. We run BXA once per data set for each model, using 400 live points, and using the standard nested sampling routine (i.e. the BXA parameter *speed* = *'safe'*).

As our data sets have between $\sim 10^5$ (F23) and $\sim 4 \times 10^5$ (HF) total photon counts, each XSPEC model call is fairly computationally expensive. BXA runs with more than six or seven free parameters are therefore not feasible for these data, as the number of XSPEC model calls required to map out $C(\boldsymbol{\theta})$ over the parameter space increases geometrically. We set certain model parameters to constant values, to limit the dimensionality of the BXA analysis; we discuss these choices in detail in our model definitions (Appendix B3). For all models, we set the cross-normalization terms $C_{\rm inst}$ to their best-fitting values for Model C1. We verify via preliminary model fits that the $C_{\rm inst}$ terms for a given data set are consistent to within 2 per cent, irrespective of which model is used.

B2 Defining a threshold for acceptable models

While the model with the highest evidence $Z_{\rm best}$ is in a sense the 'best' model of those tested, the numerical values of the unnormalized evidences Z_i for individual models are not otherwise particularly meaningful. The Bayes factors (i.e. evidence ratios Z_i/Z_j) between models i and j are the useful quantitative results for model comparison. As is typical in Bayesian model comparison, we work with the logarithms of the evidences, and express our results in terms of the Bayes factor between each model and the 'best' (highest evidence) model tested. Thus, we express the logarithmic Bayes factor between a given model and the 'best' model as $\Delta\log(Z) = \log(Z_{\rm best}) - \log(Z_{\rm model})$.

A Bayes factor of $\Delta\log(Z) > 2$ is traditionally interpreted as 'decisive' evidence for the better model in the broader statistical literature (e.g. Kass & Raftery 1995). Recently, Waddell et al. (2023) investigated this interpretation empirically using a statistical sample of simulated AGN X-ray observations. These authors measure the frequency with which BXA returns higher evidence for an incorrect model, and determine a 'purity' threshold for $\Delta\log(Z)$ based thereon. They find that a threshold of $\Delta\log(Z) = 2.6$ is required to ensure a false positive rate below 2.5 per cent when testing for the presence of soft X-ray excess. However, in general the appropriate threshold will depend on the details of both the models and the observations (e.g. exposure times, instrumental response matrices, and wavelength-dependent sensitivities). It is prohibitively computationally expensive to perform similar simulations for our deep, multi-instrument data sets. We therefore instead adopt a conservative threshold for our model selection, requiring $\Delta\log(Z) > 3$ to formally prefer one model over the other. This criterion is used to select our 'preferred' models (Section 3.3.3), which correspond to Models C2 and G as defined below. Reassuringly, these preferred models (which include warm Comptonization components) display Bayes factors of $\Delta\log(Z) > 10$ compared to any models that lack warm Comptonization. This is also true for models lacking distant reflection components; in fact, those models are suppressed by even larger Bayes factors, $\Delta\log(Z) > 29$. Thus, our main findings (that warm Comptonization and distant reflection are required; Section 3.3.2) are robust to any reasonable choice of $\Delta\log(Z)$ threshold.

B3 Model definitions

We define models A–G (roughly in order of increasing complexity) below. All models include a CONST term representing the per-detector calibration factors $C_{\rm inst}$, and a TBABS term representing Galactic absorption with $N_{\rm H} = 2.77 \times 10^{20}$ cm^{-2} (HI4PI Collaboration et al. 2016). We present the parameter bounds for each model in Table B1. In cases where different model components have parameters with the same physical meaning (e.g. $E_{\rm cut}$ for Model C2 should be roughly equivalent to $3kT_e$ for Model C3), we apply consistent parameter bounds; this avoids spurious differences in Z due to choices of prior. We present the logarithmic Bayes factors $\Delta\log(Z)$ for each model, compared to the 'best' model, in Table B2. We illustrate models C1 through H as C-stat optimized fits to the LF and HF data sets in Figs B1 through B16. For Model G, we include 'corner plots' of the BXA posterior distributions, to illustrate the parameter degeneracies at play when using two reflection regions (Figs B17 and B18).

Model A: continuum only

XSPEC model definition: CONST×TBABS×POWERLAW

We begin our model comparison with a simple power law, with two free parameters: the normalization $N_{\rm cont}$ and photon index Γ. This model is clearly inadequate; we include it to quantify the improvement in evidence for the more complex Models B–H.

Model B: warm Comptonization

CONST×TBABS(POWERLAW + NTHCOMP)

We add a Comptonization component to model the soft excess, represented by the NTHCOMP model (Zdziarski et al. 1996; Życki et al. 1999). This model is characterized by a photon index $\Gamma_{\rm warm}$, which depends physically on the optical depth and scattering geometry. For the BXA runs, we set a constant $\Gamma_{\rm warm} \equiv 2.5$, as typically found for Seyfert galaxies (Petrucci et al. 2018). For the seed photons we set a constant energy of 10 eV (i.e. UV seed photons). The resulting model has two additional free parameters relative to model A: the soft excess temperature kT_e, and normalization $N_{\rm warm}$. For all four data sets (LF, HF, J21 and F23) we see a substantial increase in evidence for Model B relative to Model A.

Models C1–C4 (preferred!): warm Comptonization plus distant reflection

C1: CONST×TBABS(POWERLAW+NTHCOMP + PEXMON)
C2: CONST×TBABS(ZCUTOFFPL+NTHCOMP + PEXMON)
C3: CONST×TBABS(NTHCOMP$_1$ + NTHCOMP$_2$ + PEXMON)
C4: CONST×TBABS(POWERLAW + NTHCOMP
+ ATABLE{BORUS02_V170323C.FITS})

We now add a non-relativistic reflection component. The PEXMON component (Nandra et al. 1997) combines Compton reflection (Magdziarz & Zdziarski 1995) with energetically consistent Iron and Nickel K-shell emission lines. The strength of the reflection features is parameterized by R, where $R = -1$ is the expected

Table B1. Model parameter ranges used for BXA runs.

Col.	Parameter	Model A	B	C, C2, C3, C4	D_n, D_i	E	F	G	H
(1)	$N_{\rm H,Gal}$	2.77×10^{20}	2.77×10^{20}	2.77×10^{20}	2.77×10^{20}	2.77×10^{20}	2.77×10^{20}	2.77×10^{20}	2.77×10^{20}
(2)	$N_{\rm cont}$	10^{-5}, 10^{-2}	10^{-5}, 10^{-2}	10^{-5}, 10^{-2}	10^{-5}, 10^{-2}	10^{-7}, 10^{-4}	10^{-5}, 10^{-2}	10^{-5}, 10^{-2}	10^{-5}, 10^{-2}
(3)	Γ	1.1, 2.4	1.1, 2.4	1.1, 2.4	1.1, 2.4	1.1, 2.4	1.1, 2.4	1.1, 2.4	1.1, 2.4
(4)	$N_{\rm warm}$		10^{-6}, 10^{-2}	10^{-6}, 10^{-2}	10^{-6}, 10^{-2}		10^{-6}, 10^{-2}	10^{-6}, 10^{-2}	
(5)	$\Gamma_{\rm warm}$		2.5	2.5	2.5		2.5	2.5	
(6)	kT_e		0.05, 1	0.05, 1	0.05, 1		0.05, 1	0.05, 1	
(7)	$E_{\rm cut}$			20, 300				20, 300	20, 300
(8)	$kT_{e,\rm hot}$			6, 100				$\equiv E_{\rm cut}/3$	$\equiv E_{\rm cut}/3$
(9)	i			30°	30°	30°	30°	30°	30°
(10)	Z			1	1	1	1	1	1
(11)	$A_{\rm Fe}$			5	5	5	5	5	5
(12)	R			-5, -0.05	-5, -0.05			-5, -0.05	-5, -0.05
(13)	$N_{\rm H,int}$				10^{20}, 10^{24}				
(14)	$\xi_{\rm abs}$				10^{-3}, 10^{5}				
(15)	$z_{\rm abs}$				-0.48, 0.52				
(16)	CF				1, $\frac{2}{3}$, $\frac{1}{3}$				
(17)	$n_{\rm rel}$					10^{15}, 10^{20}	10^{15}, 10^{20}	10^{15}	10^{15}, 10^{20}
(18)	$\log(\xi)_{\rm rel}$					0,1,2,3,4	0,1,2,3,4	0,1,2,3,4	0,1,2,3,4
(19)	$a_{*,\rm rel}$					0, 0.998	0, 0.998	0, 0.998	0, 0.998
(20)	$R_{\rm rel}$					-5, -0.05	-5, -0.05	1	1
(21)	$h_{\rm rel}$					10	10	10	10
(22)	$\beta_{\rm rel}$					0	0	0	0

Notes. Allowed parameter ranges for the different models tested in our BXA analysis (3.3). Parameters that are held constant during our BXA runs are listed in grey. Parameters that are 'stepped through' (i.e. we perform multiple BXA runs with different constant values of that parameter) appear as comma-separated lists . For parameters that range over several orders of magnitude we adopt a log-uniform prior . For all other parameters we adopt a uniform prior between the lower and upper limits listed. We note that some parameters are held constant or 'stepped through' here, but instead treated as free parameters in our final analysis (Section 3.3.4). This is due to the high computational demands of the BXA runs.
Remarks on individual parameters: (1) Galactic column density in $\rm cm^{-2}$. (2) The normalization of the primary continuum component. For POWERLAW or ZCUTOFFPL continua, this is given as photons $\rm keV^{-1}$ $\rm cm^{-2}$ measured at 1 keV. For RELXILL models the normalization is as defined by Dauser et al. (2022). (3) The photon index of the primary (observed) continuum; for reflection models we tie this to the Γ of the incident continuum. (4) The normalization of the warm Comptonization (NTHCOMP) component. (5) The photon index of the warm Comptonization component. (6) The electron temperature of the warm Comptonization component, in keV. (7) The cut-off energy for ZCUTOFFPL components, in keV. (8) The electron temperature of the hot Comptonization component, in keV. This is treated as a free parameter for Model C3 only. (9) The reflection plane inclination, where $i = 0$ corresponds to face-on, is held constant for all reflection models. (10) The metallicity, assumed Solar for all reflection models. (11) The Iron abundance, set to five times Solar for all reflection models, for reasons discussed in Appendix B3. (12) The reflection factor for PEXMON components. (13) The column density of intrinsic absorption components (neural or ionized), in $\rm cm^{-2}$. (14) The ionization parameter of an ionized absorber. (15) The in- or outflow velocity of an ionized absorber, expressed as a redshift. (16) The covering fraction of an ionized absorber, where $CF = 1$ denotes full coverage of the continuum source. (17) The disc particle density for RELXILLCPLP models, in $\rm cm^{-3}$. (18) The ionization parameter of RELXILLLP or RELXILLCPLP components, parameterized at the innermost stable circular orbit. (19) The black hole spin parameter, for RELXILLLP or RELXILLCPLP components. (20) The reflection strength of relativistic reflection, as defined by Dauser et al. (2022). (21) The height of the X-ray continuum source above the disc, in gravitational radii. (22) The velocity of the continuum source relative to the disc.

reflection from an infinite slab of neutral, Compton-thick gas.[7] We allow the reflection strength to vary between $-0.1 > R > -5$; here, $R = -0.1$ is barely detectable in typical observing situations. We tie the PEXMON incident continuum normalization and photon index to that of the POWERLAW component.

The reflected spectrum depends on the inclination i of the line-of-sight to the reflecting surface (where $i = 0°$ is face-on). We impose $i \equiv 30°$ for all reflection components (Models C1 through H). This is a typical estimate for the accretion plane of Type 1 AGN (e.g. Wu & Han 2001; Marin 2016), and is consistent with the estimate $i = 47^{+38}_{-47}°$ made by Bhayani & Nandra (2011) for Mrk 590 specifically.

[7]The negative sign causes the PEXMON component to only return the reflected spectrum, such that the continuum can be modelled separately. We use negative R in all PEXMON modelling, as this allows us to test different continuum models, e.g. Model C3.

The elemental abundance Z and Iron abundance $A_{\rm Fe}$ affect the shape of the reflected spectrum in non-trivial ways (e.g. García et al. 2014). To ensure that the parameter space is of manageable size, we keep Z and $A_{\rm Fe}$ constant during the BXA runs. After some initial experimentation, we set $A_{\rm Fe} \equiv 5$; we find this is necessary to match the observed 6.4 keV line strength. We discuss the issue of super-Solar iron abundance further in Section 3.3.4, where we include $A_{\rm Fe}$ as a free parameter in our preferred models.

In all cases, the evidence for Model C1 is higher than for Model B. However, Model C1 over-predicts the X-ray flux above ~ 30 keV, especially for the LF data set (Fig. B1). We therefore test whether there is evidence for a high-energy cut-off of the X-ray continuum. For Model C2, we include an ad-hoc exponential cut-off in the continuum at energy $E_{\rm cut}$. For Model C3, we replace the power-law continuum with a physically motivated hot Comptonization (NTHCOMP) component (e.g. Życki et al. 1999), for which the high-energy curvature is parameterized by the electron temperature $kT_{e,\rm hot}$. For all four data sets, Model C2 is preferred over C1 and C3. Thus,

Table B2. Model comparison for joint data sets.

Model	Variant	LF $\Delta\log(Z)$	HF $\Delta\log(Z)$	J21 $\Delta\log(Z)$	F23 $\Delta\log(Z)$	LF *C*/DOF	HF *C*/DOF	J21 *C*/DOF	F23 *C*/DOF
(1)	(2)	(3)	(4)	(5)	(6)	(7)	(8)	(9)	(10)
A		608.8	1309.6	160.4	268.4	5936/4674	8266/5764	3019/2593	3056/2671
B		158.8	75.2	62.7	89.6	5247/4672	6372/5762	2747/2591	2776/2669
C		12.8	3.3	14.5	13.6	4948/4671	6218/5761	2640/2590	2619/2668
C2	Cut-off PL	**1.9**	**0.6**	★	★	4935/4670	6215/5760	2610/2589	2589/2667
C3	NTHCOMP cont.	9.8	10.8	4.1	7.9	4936/4670	6231/5760	2609/2589	2596/2667
C4	Torus	**2.6**	**0.4**	**2.4**	5.0	4942/4669	6197/5759	2622/2588	2600/2666
D_n		13.9	18.0	12.9	10.8	4933/4670	6278/5760	2631/2589	2604/2667
D_i	CF = 1	31.9	36.4	15.2	17.7	4985/4669	6245/5759	2693/2588	2641/2666
D_i	CF = 0.66	31.9	25.2	12.6	17.7	4985/4669	6444/5759	2751/2588	2634/2666
D_i	CF = 0.33	4.9	35.4	11.6	**0.1**	4998/4669	6438/5759	2656/2588	2637/2666
E	$\log\xi = 0, a_* = 0$	100.4	208.5	46.1	58.6	5192/4672	6680/5761	2719/2590	2695/2668
E	$\log\xi = 1, a_* = 0$	99.2	202.0	43.6	55.8	5129/4672	6656/5761	2702/2590	2691/2668
E	$\log\xi = 2, a_* = 0$	89.0	188.0	41.6	52.6	5105/4672	7759/5671	2702/2590	2685/2668
E	$\log\xi = 3, a_* = 0$	83.6	194.4	40.4	55.1	5094/4672	6618/5761	2690/2590	2680/2668
E	$\log\xi = 4, a_* = 0$	116.8	200.2	51.4	75.3	5164/4672	6751/5761	2708/2590	2700/2668
E	$\log\xi = 0, a_* = 0.98$	101.8	208.4	47.0	59.4	5154/4672	6850/5761	2741/2590	2710/2668
F	$\log\xi = 0, a_* = 0$	52.8	52.8	39.6	40.1	5016/4670	6261/5760	2664/2589	2642/2667
F	$\log\xi = 1, a_* = 0$	55.7	29.1	38.5	40.9	5022/4670	6266/5760	2664/2589	2643/2667
F	$\log\xi = 2, a_* = 0$	59.2	39.7	38.8	43.6	5026/4670	6286/5760	2662/2589	2653/2667
F	$\log\xi = 3, a_* = 0$	80.5	29.5	43.4	57.3	5055/4670	6266/5670	2674/2589	2672/2667
F	$\log\xi = 4, a_* = 0$	114.1	33.2	37.8	56.7	5141/4670	6283/5760	2695/2589	2689/2667
F	$\log\xi = 0, a_* = 0.98$	56.6	31.2	41.0	42.7	5023/4670	6269/5760	2666/2589	2645/2667
F	$\log\xi = 3, a_* = 0.98$	81.8	33.0	43.9	57.8	5055/4570	6272/5760	2675/2589	2672/2667
G	$\log\xi = 0, a_* = 0$	**3.0**	★	12.7	8.6	4918/4668	6209/5759	2610/2588	2586/2666
G	$\log\xi = 1, a_* = 0$	22.9	39.9	7.1	9.2	4923/4668	6210/5759	2610/2588	2586/2666
G	$\log\xi = 2, a_* = 0$	14.2	38.4	4.7	6.3	4918/4668	6210/5759	2608/2588	2584/2666
G	$\log\xi = 3, a_* = 0$	**0.9**	7.3	**2.5**	**2.9**	4913/4668	6206/5759	2608/2588	2585/2666
G	$\log\xi = 4, a_* = 0$	16.8	39.9	23.2	6.9	4921/4668	6209/5759	2610/2588	2586/2666
G	$\log\xi = 0, a_* = 0.98$	21.0	39.7	7.4	9.4	4921/4668	6210/5759	2611/2588	2586/2666
G	$\log\xi = 1, a_* = 0.98$	23.3	40.8	7.4	9.7	4923/4668	6210/5759	2610/2588	2585/2666
G	$\log\xi = 2, a_* = 0.98$	15.2	38.7	4.9	6.4	4919/4668	6211/5759	2609/2588	2584/2666
G	$\log\xi = 3, a_* = 0.98$	★	9.2	**2.2**	**2.6**	4912/4668	6207/5759	2608/2588	2585/2666
G	$\log\xi = 4, a_* = 0.98$	17.1	40.1	6.6	6.8	4921/4668	6209/5759	2610/2588	2586/2666
H	$\log\xi = 0, a_* = 0$	79.8	182.4	27.4	38.3	5254/4670	7302/5760	2758/2589	2792/2667
H	$\log\xi = 1, a_* = 0$	74.0	208.9	29.8	40.5	5037/4670	6666/5760	2670/2589	2637/2667
H	$\log\xi = 2, a_* = 0$	57.9	208.1	24.3	36.2	5046/4670	6618/5760	2679/2589	2633/2667
H	$\log\xi = 3, a_* = 0$	52.7	201.7	19.2	36.0	4994/4670	6603/5760	2659/2589	2633/2667
H	$\log\xi = 4, a_* = 0$	75.6	307.9	29.0	48.0	5021/4670	6776/5760	2681/2589	2652/2667

Note. Comparison of Bayesian evidence Z (columns 3–6) for different models (column 1) fitted to our joint data sets (3.3). Models A through H are described in Appendix B3. For models where we 'step through' discrete values of certain parameters, the relevant values are listed in column (2). The evidence (i.e. the marginal likelihood) is calculated using the BXA software (Buchner et al. 2014), over the parameter space defined by the bounds in Table B1. The model with the highest evidence, for a given data set, is indicated with a star symbol (★). For all other models, we tabulate the *difference* in log-evidence, $\Delta\log(Z) = \log(Z_{\rm best}) - \log(Z_{\rm model})$, between that model and the best (★) model. Models with the difference in log-evidence listed in **bold text** have $\Delta\log(Z) < 3$; adopting a rather conservative threshold (Section 3.3.2), we do not consider such models to be decisively disfavoured compared to the best model. We also tabulate the Cash statistic and degrees of freedom (*C*/DOF, columns 7–10) for an XSPEC C-stat optimization, initiated at the posterior peak-likelihood parameter values obtained during the relevant BXA run, to provide an idea of the goodness of fit for that model.

while our data require some additional spectral curvature, its detailed shape is *not* particularly well-described by the high-energy peak of a hot Comptonization component.

Motivated by this finding, we experiment with a Compton-thin reflection component. This would drive down the flux near 30 keV by producing a weaker Compton reflection hump. For Model C4, we replace PEXMON with the BORUS02 torus-geometry model (Baloković et al. 2018), which includes a torus opening angle i_t and column density $N_{H,t}$ as additional parameters. We limit the torus opening angle to $i_t > 30^\circ$ (i.e. the line of sight, $i \equiv 30^\circ$, is not obscured by the torus). For the LF, HF and J21 data sets, the evidence for Model C4 is roughly equal to that of C2, while for F23, Model C2 is preferred. In summary, either a high-energy cut-off or a Compton-thin reflector are required; we use an exponential cut-off in Models E through H.

Models D_n and D_i: intrinsic absorption

D_n: CONST×TBABS×ZTBABS(POWERLAW + NTHCOMP + PEXMON)

D_i: CONST×TBABS×ZXIPCF(POWERLAW + NTHCOMP + PEXMON)

To test for any strong intrinsic absorption, we firstly add a neutral absorber component at the systemic redshift (Model D_n). Model C1 is preferred over Model D_n for all data sets. Thus, the intrinsic neutral absorption is negligible for Mrk 590 in both low- and high-flux states.

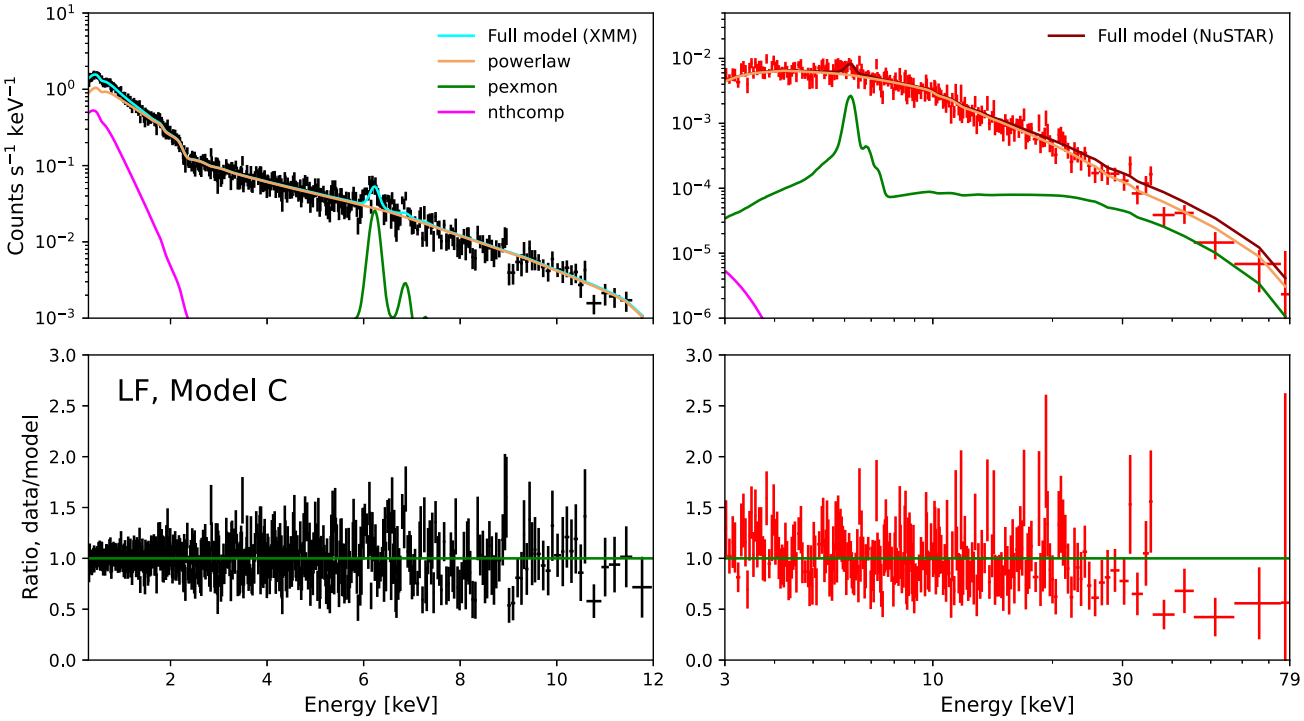

Figure B1. Model C (warm Comptonization and distant reflection) fitted to the LF data set. The upper panel shows the count rate spectrum, while the lower panel shows the data/model ratio. Photon energies are provided in the observed frame. The cyan curve (*XMM–Newton pn*) and red-brown curve (*NuSTAR*) indicate the composite models, including Galactic absorption and instrumental scaling factors. The orange (POWERLAW), green (PEXMON), and magenta (soft Comptonization NTHCOMP) curves indicate the predicted count rates for the individual additive model components.

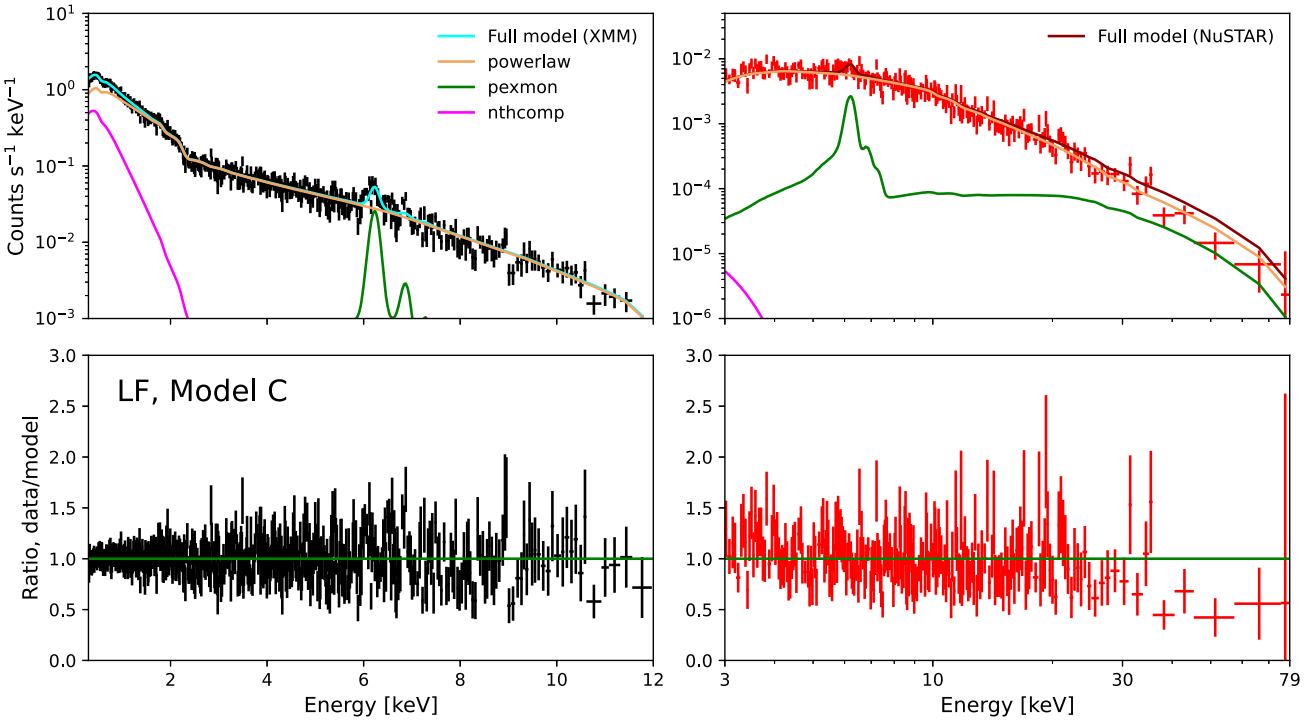

Figure B2. As Fig. B1 but for the HF data set.

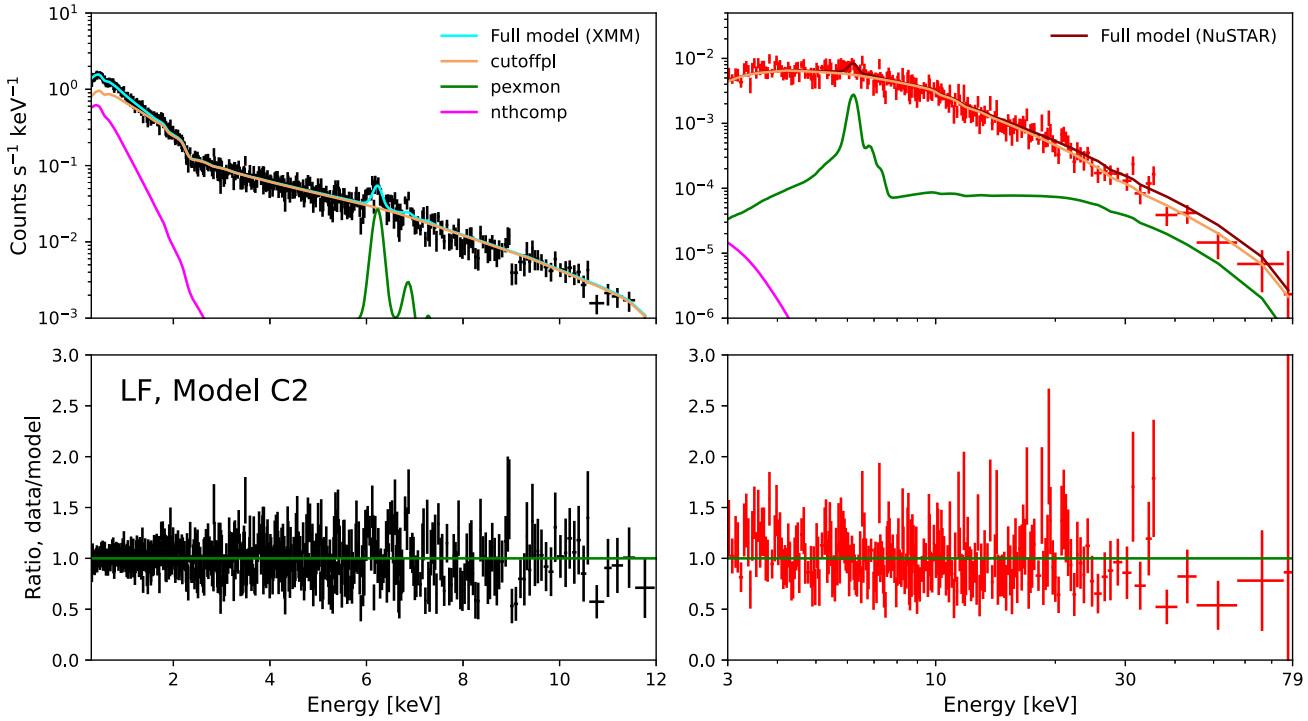

Figure B3. As Fig. B1 but for Model C2, for the LF data set.

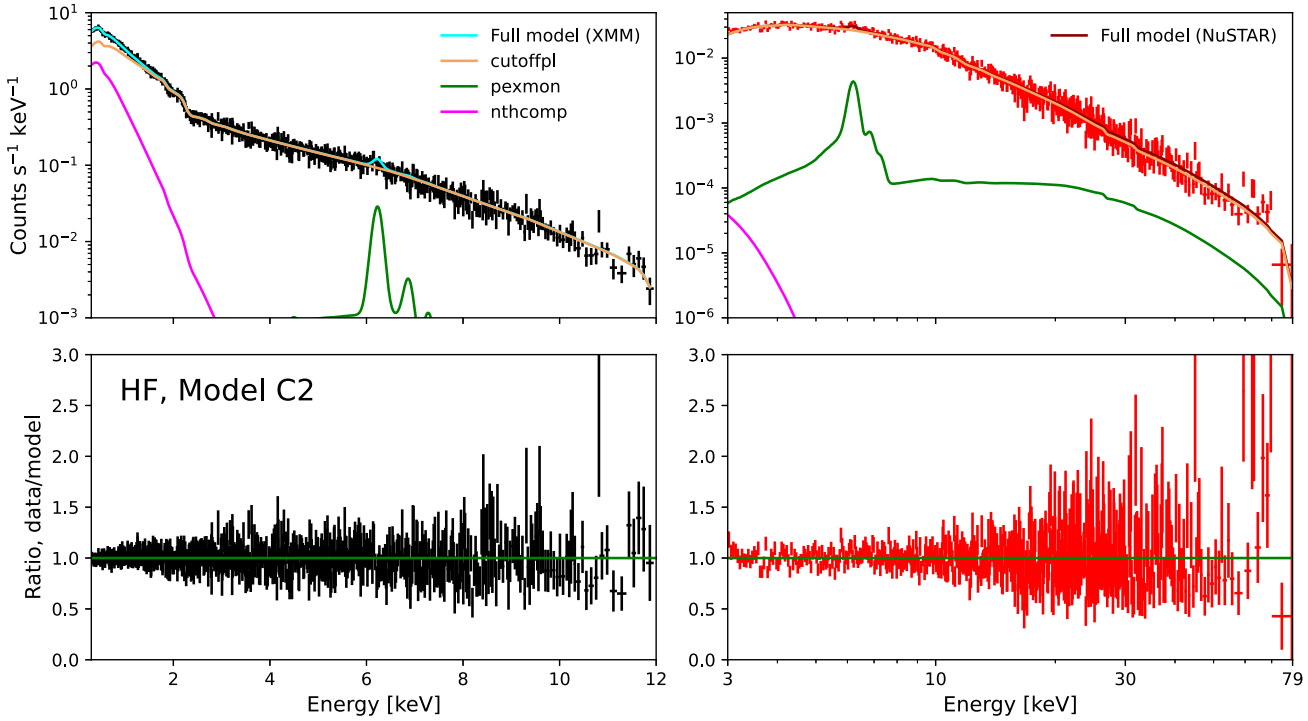

Figure B4. As Fig. B1 but for Model C2, for the HF data set.

We also test for ionized and/or partially covering absorption using the ZXIPCF component (Reeves et al. 2008) (Model D_i), which includes the ionization strength ξ and the absorber covering fraction CF as additional parameters. For the BXA analysis, we set the ZXIPCF redshift to the systemic redshift. We test covering fractions of 1, 2/3, and 1/3, where a fraction $CF - 1$ of the source flux bypasses the absorber entirely. For all data sets, Model C1 is preferred over D_i. Finally, we test whether an ionized absorber is in- or outflowing at a

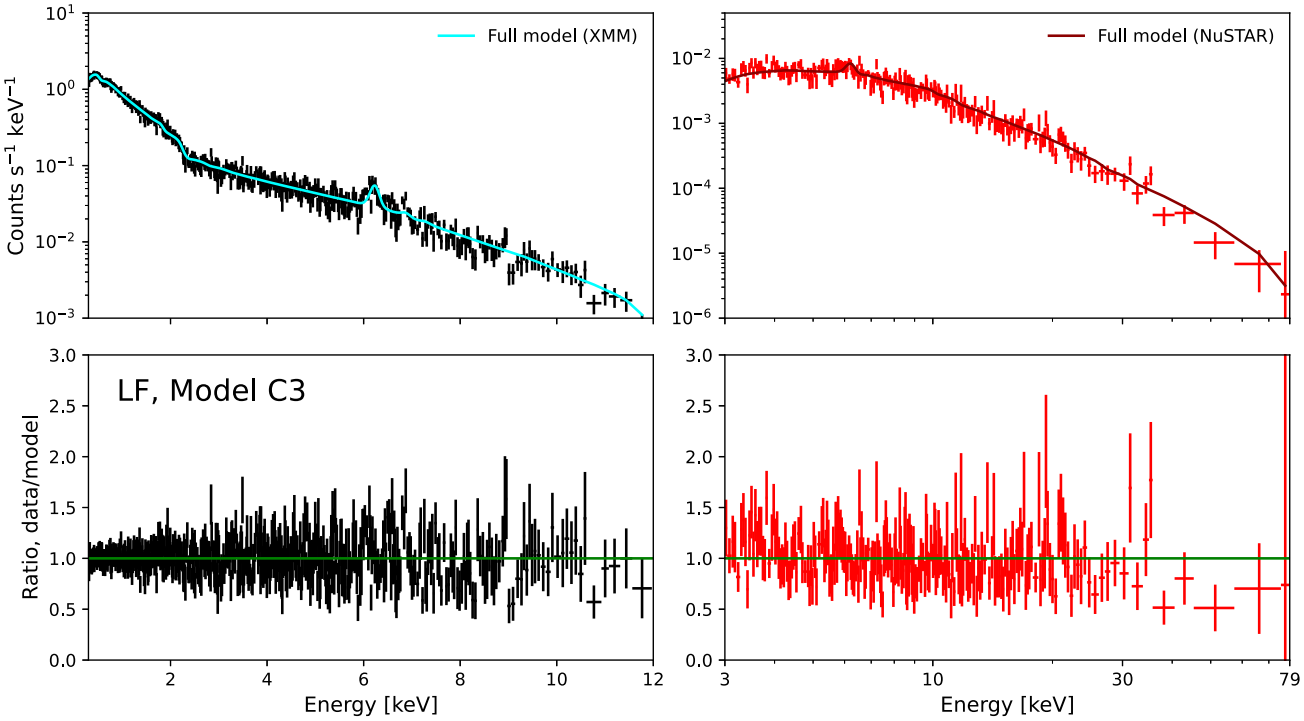

Figure B5. As Fig. B1 but for Model C3 for the LF data set.

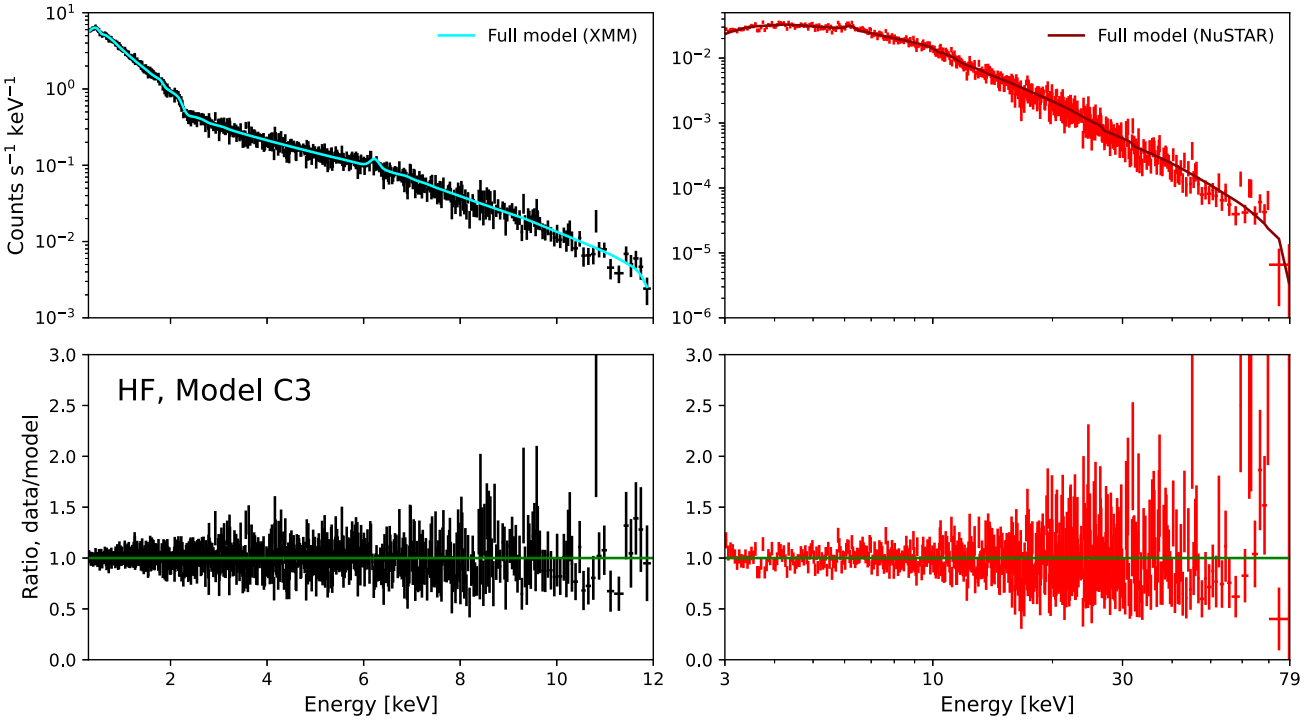

Figure B6. As Fig. B1 but for Model C3, for the HF data set.

relativistic velocity, which would produce a shift in the energies of the absorption troughs. To avoid a large computational burden, we turn to *C-stat* minimization for this test. We allow $0.33 < CF < 1$, and allow the absorber redshift to vary from the systemic by up to $\Delta v = \pm 0.5$c. We find that the column density $N_{\rm H,int}$ converges at its lower limit of 10^{20} cm^{-2}, while both the absorber redshift and ξ are very poorly constrained. This confirms the lack of strong intrinsic absorption in our data.

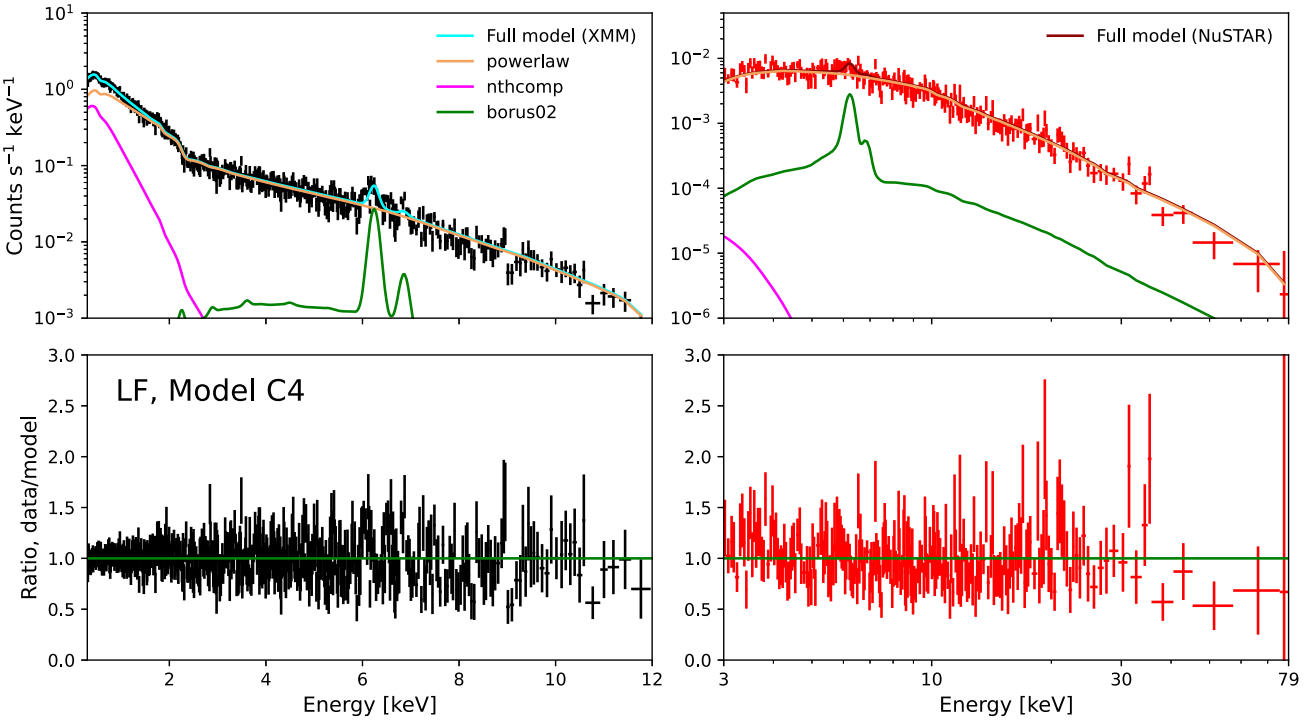

Figure B7. As Fig. B1 but for Model C4, for the LF data set.

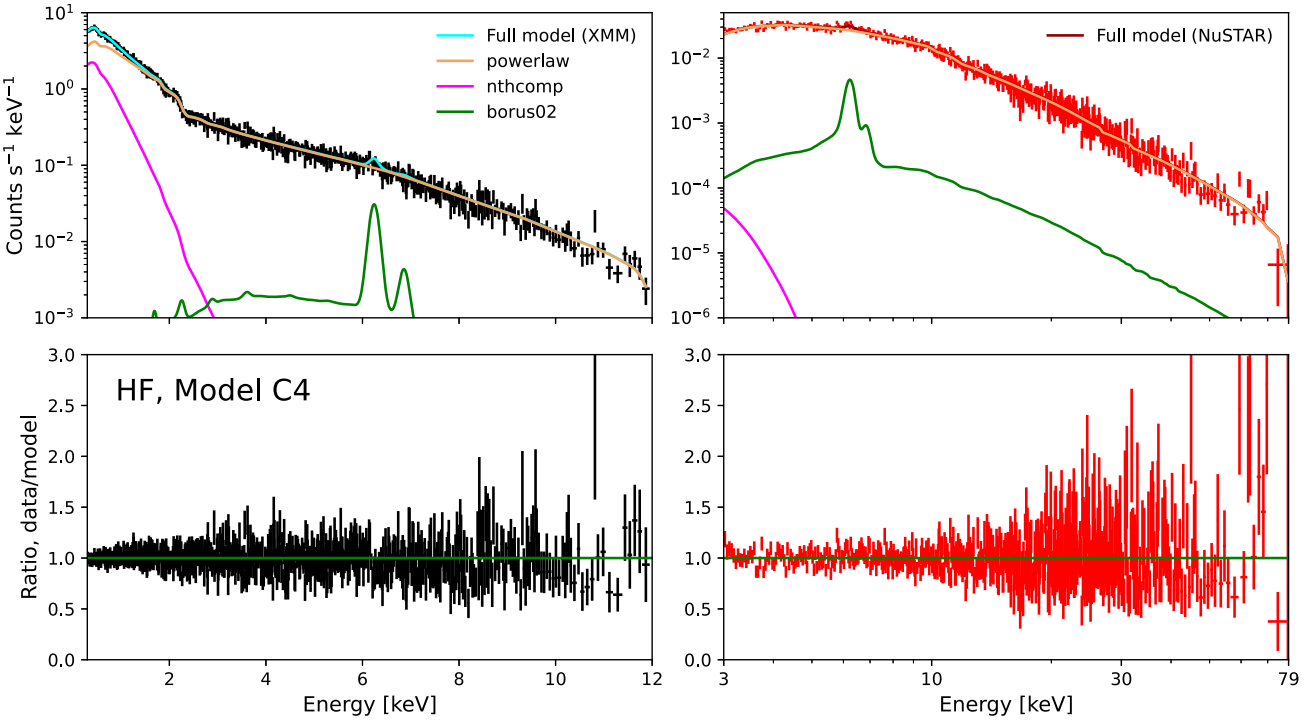

Figure B8. As Fig. B1 but for Model C4, for the HF data set.

Model E: relativistic reflection only

CONST×TBABS(POWERLAW + RELXILLLPCP)

Reflection in an optically thick accretion disc, commonly invoked to explain broad Fe K emission lines (e.g. Nandra et al. 2007; Fabian et al. 2009), can also produce a soft excess due to relativistically blurred atomic transitions (e.g. Crummy et al. 2006; Fabian et al. 2009; Mundo et al. 2020; Xu et al. 2021). We use the RELXILL suite of models (Dauser et al. 2014; García et al. 2014; Dauser

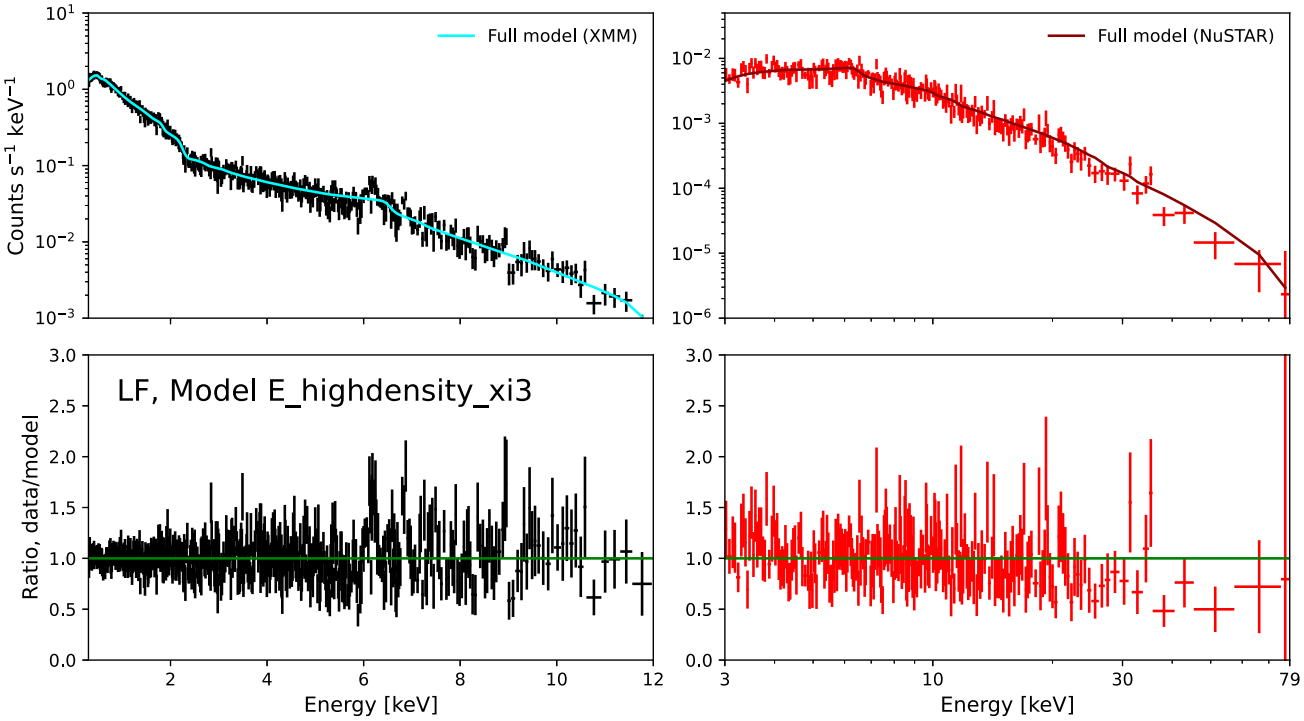

Figure B9. As Fig. B1 but for Model E, for the LF data set.

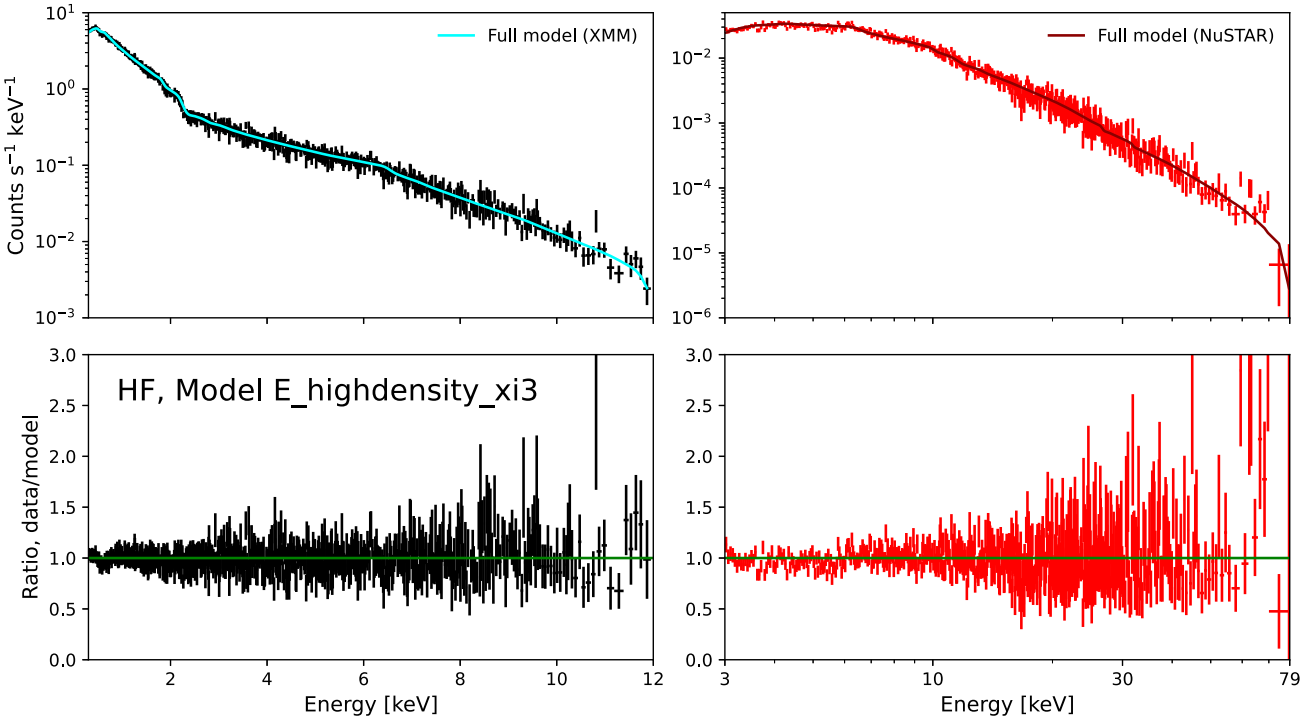

Figure B10. As Fig. B1 but for Model E, for the LF data set.

et al. 2022) to explore whether the observed soft excess features can be fully explained by accretion disc reflection. Of the available RELXILL variants, we found that only the variable-density model RELXILLLPCP generates sufficient blurred soft reflection to roughly match the observed soft X-ray flux. This is broadly consistent with the findings of Mallick et al. (2022) and Yu et al. (2023) for low-mass AGN. The geometry of this model is a 'lamp-post' irradiating source above and below the disc. The reflection

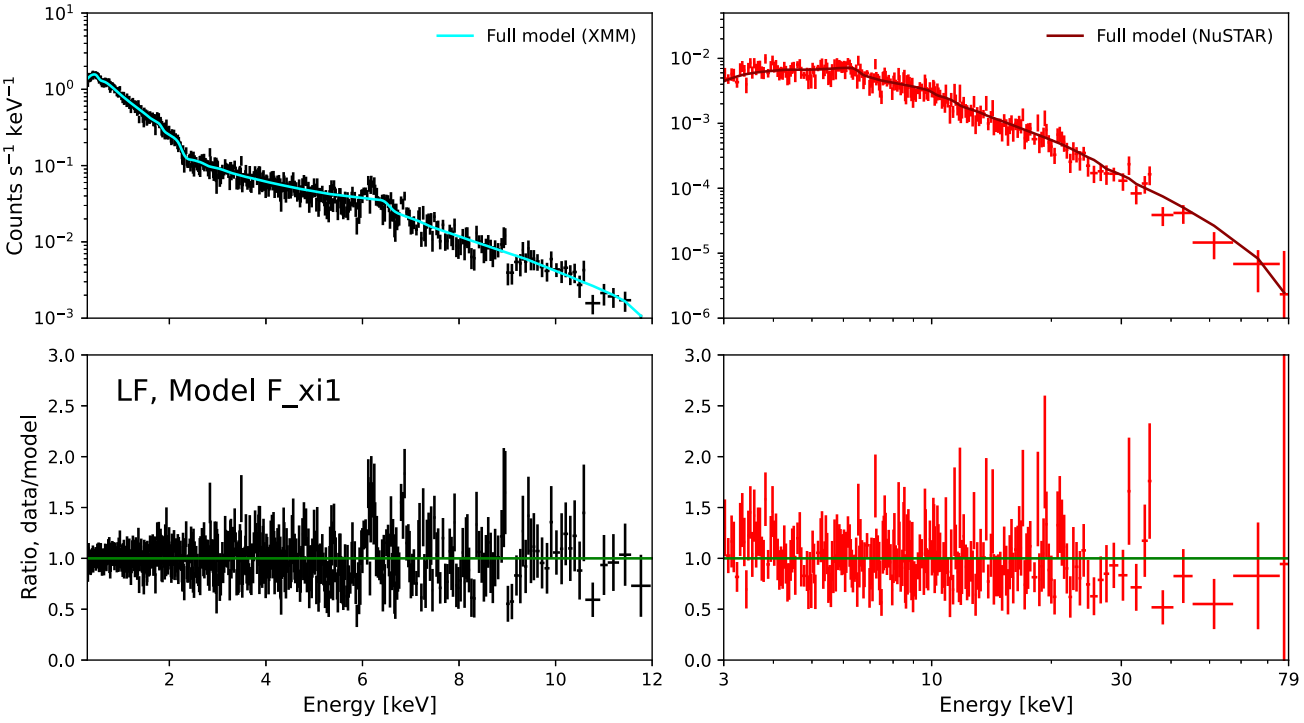

Figure B11. As Fig. B1 but for Model F, for the LF data set.

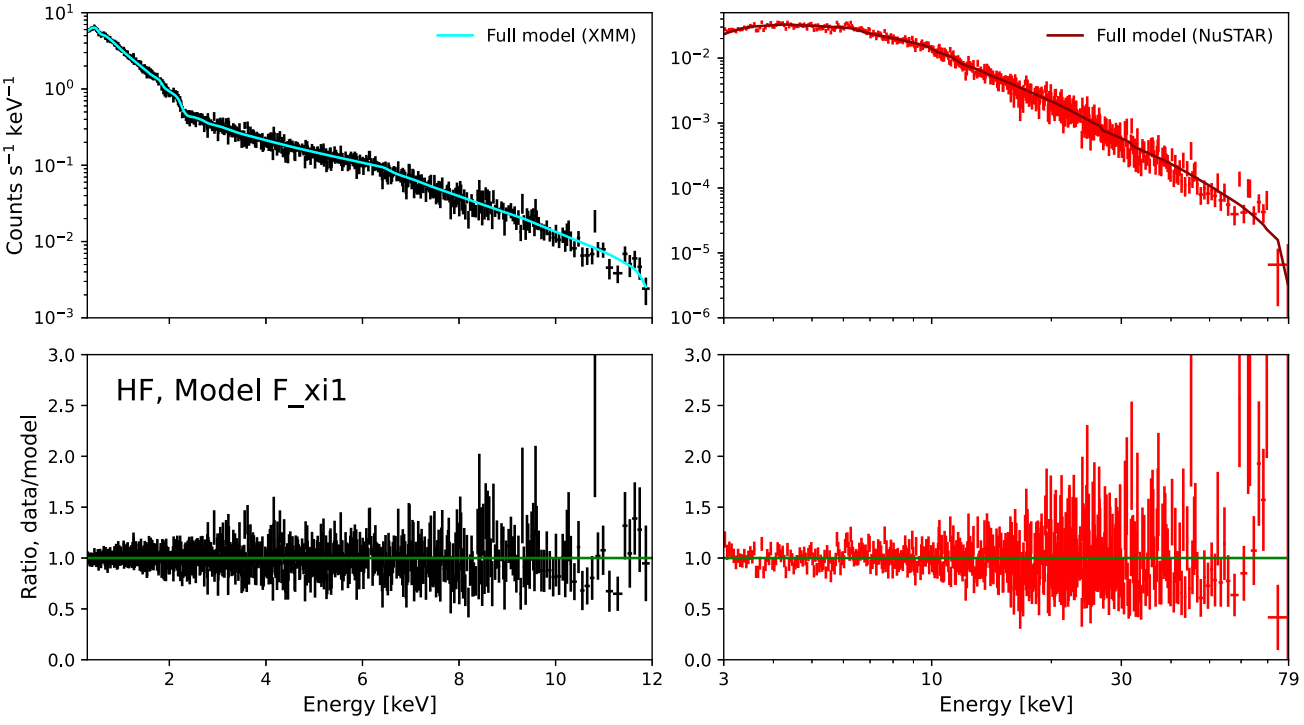

Figure B12. As Fig. B1 but for Model F, for the HF data set.

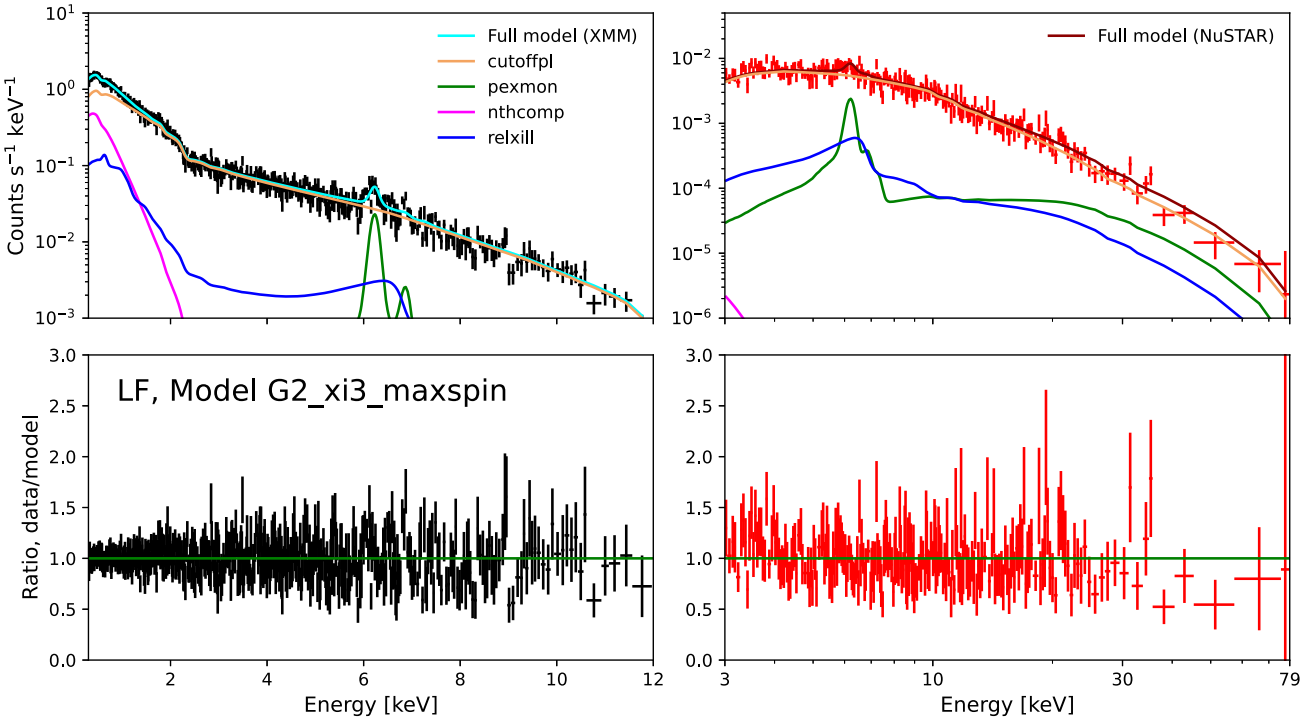

Figure B13. As Fig. B1 but for Model G, for the LF data set.

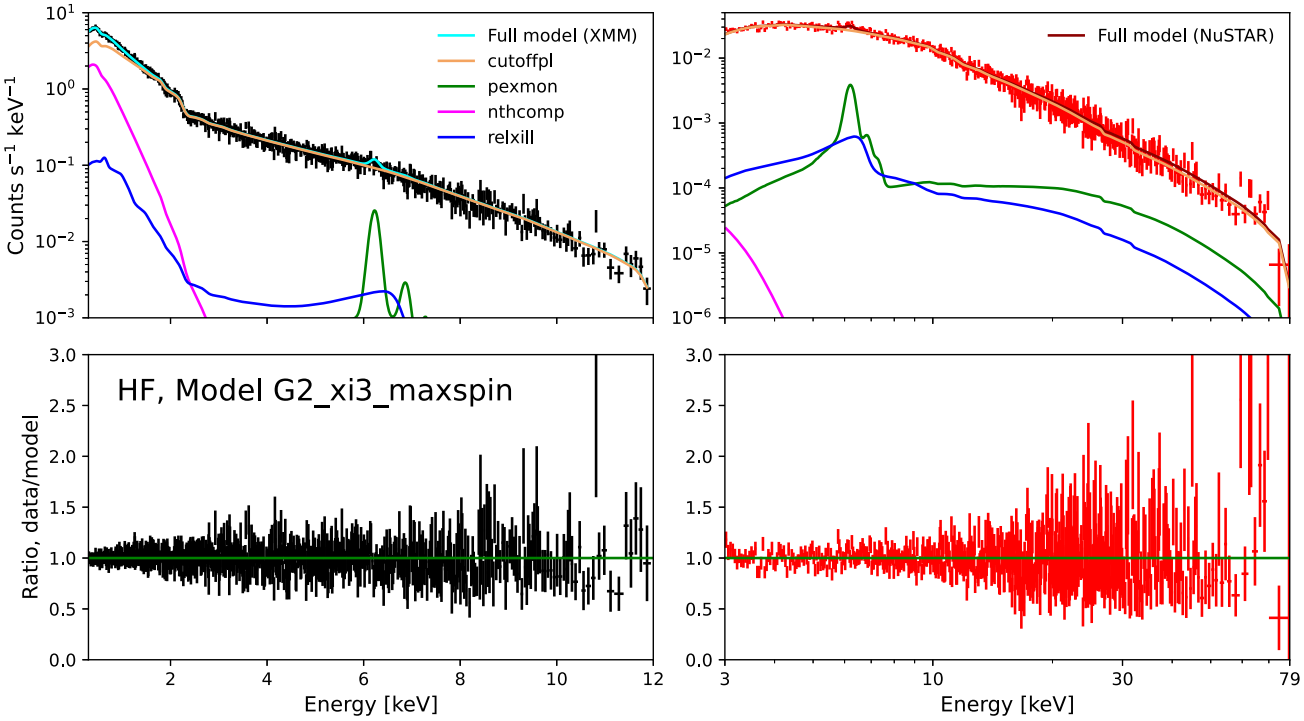

Figure B14. As Fig. B1 but for Model G, for the HF data set.

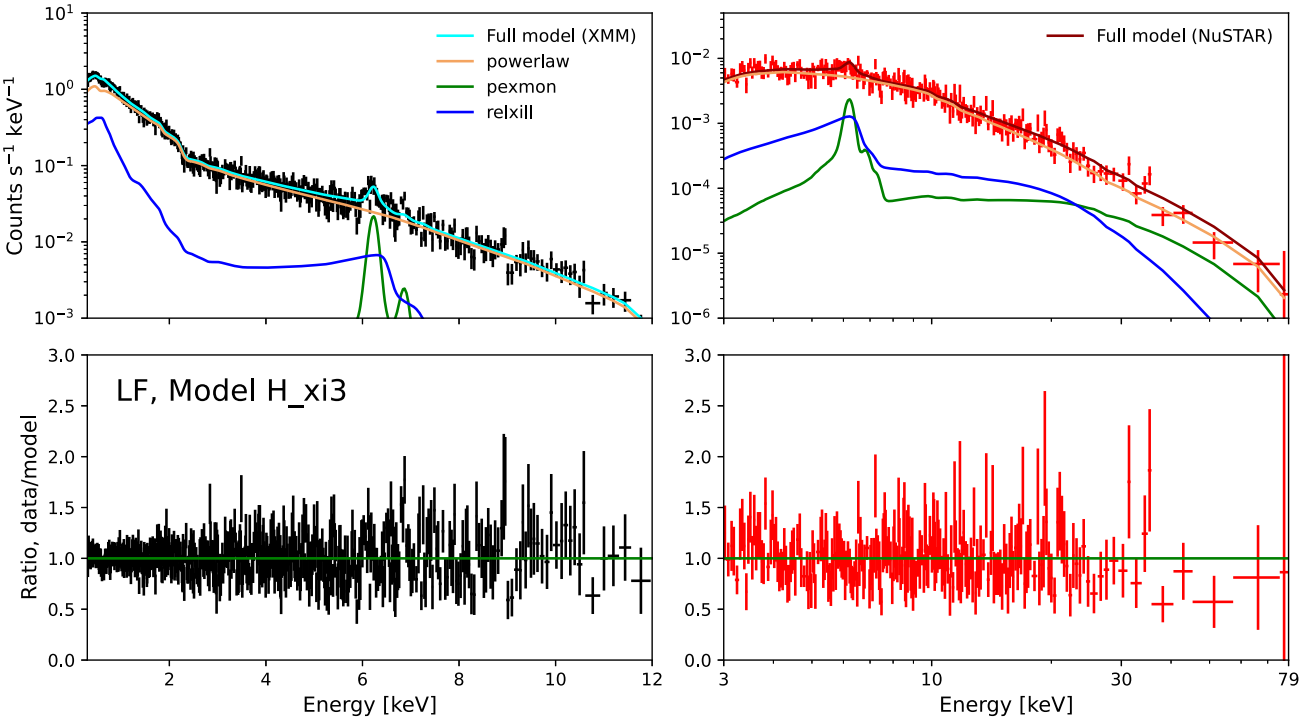

Figure B15. As Fig. B1 but for Model H, for the LF data set.

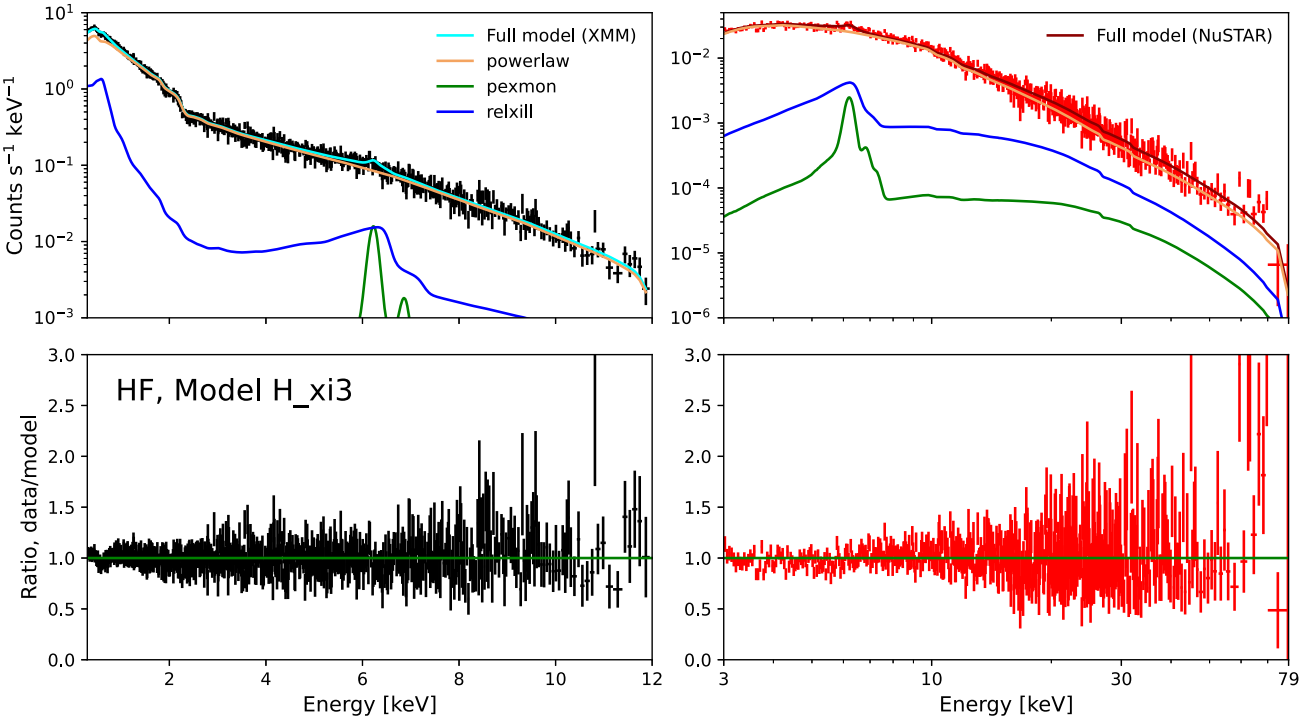

Figure B16. As Fig. B1 but for Model H, for the HF data set.

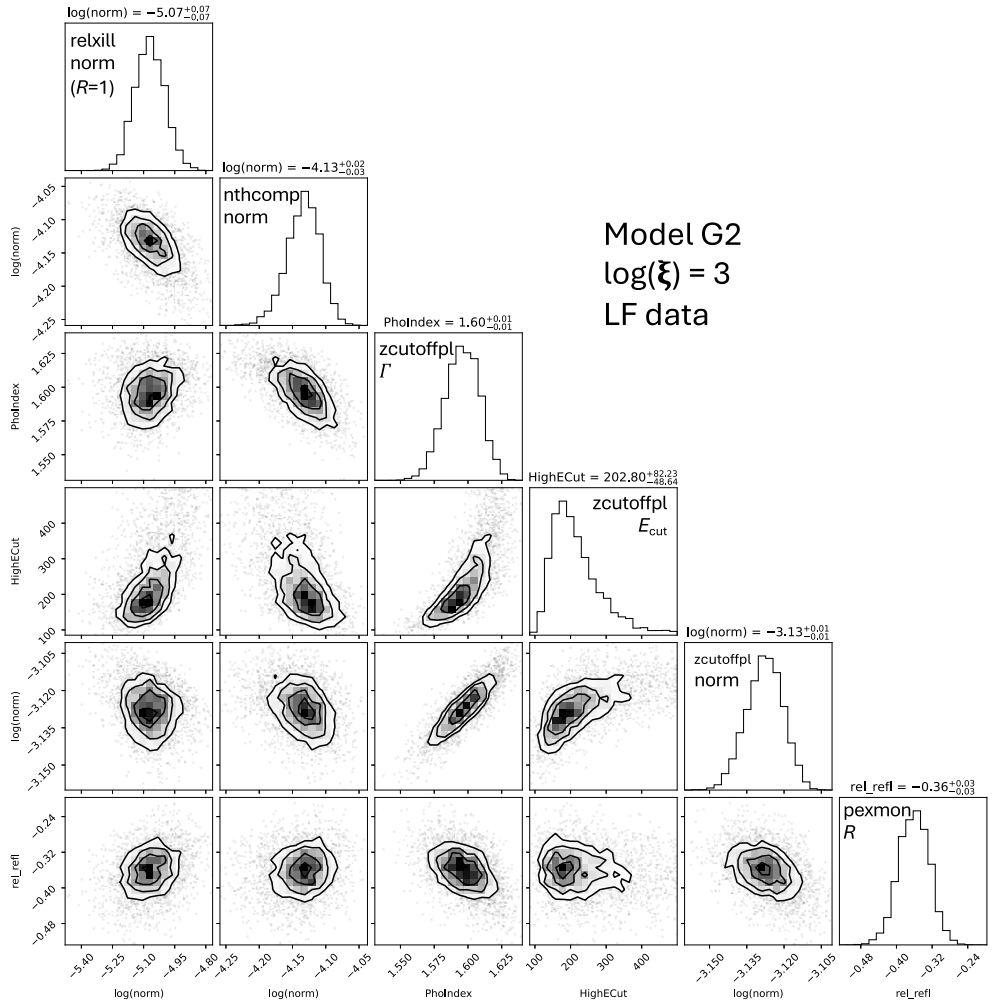

Figure B17. 'Corner plot' for the posterior distribution of our BXA run for Model G with $\log(\xi) = 3$ to the LF data set. The continuum spectral index Γ is somewhat degenerate with both the continuum normalization and the cut-off energy $E_{\rm cut}$. The PEXMON R parameter denotes the strength of the distant reflection component. It shows no strong degeneracy with the normalization of the relativistic reflection (or any other model parameters tested), and is rather weak: we find a posterior median $R = -0.36 \pm 0.03$, where $R = -1$ corresponds to a slab geometry extending to infinity.

strength[8] for RELXILL models is parameterized by $R_{\rm rel}$, where $R_{\rm rel} = -1$ is the theoretically predicted strength for disc reflection. The local ionization level of the reflecting material is radially stratified according to the thin-disc prediction, and is parameterized by its level $\xi_{\rm rel}$ at the innermost stable circular orbit. Typically, higher ionization produces a more featureless reflection spectrum (e.g. García et al. 2014). We keep $\xi_{\rm rel}$ constant in our individual BXA runs, but 'step through' five different values: $\log(\xi) = (0; 1; 2; 3; 4)$. The black hole spin parameter a_* affects the reflection fraction largely by changing the radius of the inner disc. We test variants with a non-spinning ($a_* = 0$) and maximally spinning ($a_* = 0.998$) black hole. Qualitatively, RELXILLLPCP can produce sufficient soft X-rays to roughly match the data, but lacks the required strong narrow 6.4 keV line to match the LF data set (Fig. B9). We conclude that some contribution from distant reflection is necessary. In all cases, the evidence for model E is lower than for Model C.

[8]Subtle differences in the definitions of the reflection strengths between RELXILL and PEXMON are discussed by Dauser et al. (2022).

Model F: warm Comptonization and relativistic reflection

CONST×TBABS(POWERLAW+NTHCOMP + RELXILLLPCP)

For completeness, we test a model including both warm Comptonization and relativistic reflection, but without distant reflection. Similarly to Model E, this fails to produce sufficient narrow Iron emission to match the data, and is disfavoured relative to models including a distant reflection component.

Model G (preferred!): warm Comptonization, distant reflection, and relativistic reflection

CONST×TBABS(ZCUTOFFPL + NTHCOMP
+PEXMON + RELXILLLPCP)

If Mrk 590 indeed harbours a standard 'thin disc' extending to the innermost stable orbit, we would expect some contribution from relativistic reflection. To explore this, we now include both distant and relativistic reflection components. We tie the incident photon indices Γ and high-energy cut-offs $E_{\rm cut}$ of the two reflection components to that of the power-law continuum, but allow them to have different reflection contributions. For this dual-reflection model, we fix the relativistic component reflection strength to $R_{\rm rel} \equiv -1$ and allow the RELXILLLPCP overall normalization to vary. While not strictly consistent (as the *pexmon* reflecting geometry is a uniform

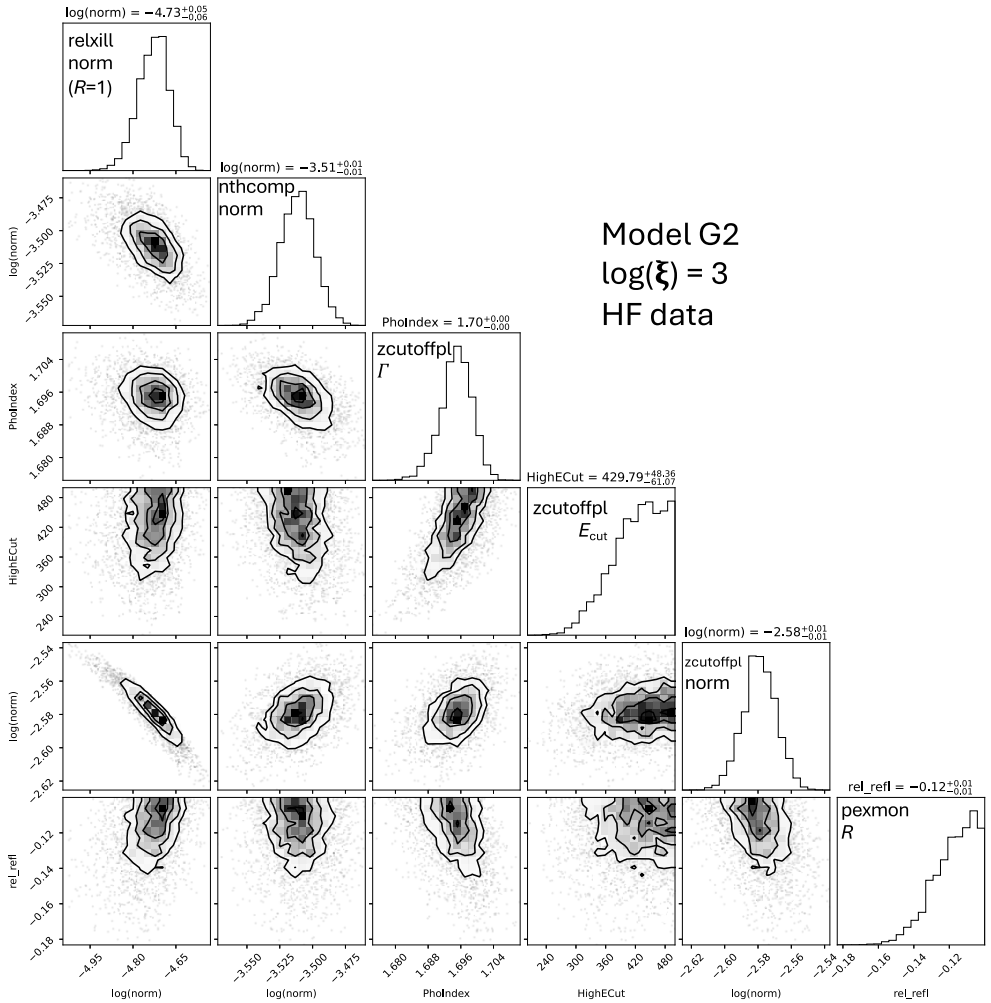

Figure B18. As Fig. B17, but for the HF data set. Here, the distant reflection is significantly weaker than in the low-flux state, with a posterior median reflection factor $R = -0.10^{+0.02}_{-0.01}$ for the PEXMON component.

plane, thus 'double-counting' the reflection at small radii), this model provides an estimate of the relative contributions of relativistic and distant reflection. As for Model E, we step through a range of ionization parameters for the disc reflection component, and test both non-rotating and maximally rotating black holes. For the LF, HF, and J21 data sets, model G is marginally preferred over C2. Thus, we cannot exclude a contribution from relativistic reflection at both high and low flux levels.

Model H: distant and relativistic reflection only.

H: CONST×TBABS (ZCUTOFFPL+PEXMON + RELXILLLPCP)

Finally, to investigate whether a separate warm Comptonization region is *required* in addition to two reflection components, we remove the NTHCOMP component from Model G. The soft excess is then entirely due to the disc reflection component, while the distant component contributes to the narrow 6.4 keV line. This scenario is in all cases strongly disfavoured relative to models including a warm Comptonization region.

B4 On model comparison methodology

Several authors have compared the blurred reflection and warm Comptonization scenarios for individual AGN. Typically, both models produce similar quality fits to the observed data, based on the reduced-χ^2 fit statistic (e.g. Pal et al. 2016; García et al. 2019; Xu et al. 2021; Chalise et al. 2022; Yu et al. 2023; Madathil-Pottayil et al. 2024). As we are working with minimally binned data, we do not use the χ^2 statistic in our analyses. We can instead consider the statistic C/DOF, i.e. the ratio of the Cash statistic C (Cash 1979) to the model-fit degrees of freedom. For our minimal binning scheme (Section 3.1), the expected value of this statistic (assuming that the model is correct and the uncertainties are accurate) is $C/\mathrm{DOF} = 1.01$ (Kaastra 2017, their equation 11). Thus, in analogy to the reduced χ^2 statistic, a value near 1 is consistent with a satisfactory model fit, given the uncertainties. Similar to other model comparison studies, we indeed only find small differences in C/DOF between models with warm Comptonization and models with relativistic reflection (Table B2). This illustrates the difference between the Bayesian approach we apply, which displays a clear preference for warm Comptonization models, and selection strategies that compare optimized ('best-fitting') models.

However, we note that the 'best-fitting' models including warm Comptonization do perform *slightly* better in terms of C/DOF for our data. For LF, the best Model G variant has $C/\mathrm{DOF}= 1.05$, while the best Model H variant (i.e. distant and relativistic reflection, but no Comptonization) displays $C/\mathrm{DOF}= 1.07$. For HF, the best-performing Model G variant yields $C/\mathrm{DOF} = 1.08$, while we obtain

$C/\mathrm{DOF} = 1.15$ for Model H. Thus, the models including warm Comptonization do yield a 'better fit' in the traditional sense.

APPENDIX C: COMPARISON BETWEEN NEAR-CONTEMPORANEOUS *SWIFT* XRT AND *XMM–NEWTON* SPECTRA

We consistently detect a soft X-ray excess in our *XMM–Newton* observations (Section 3.2), even at the lowest observed continuum flux levels. In fact, after accounting for the X-ray continuum flux dependence of the soft excess, we see no indication that the soft excess behaviour changed after the 2010s changing-look event, compared to archival spectra observed 2002–2004. This is at odds with the findings of Ghosh et al. (2022), who analyse *Swift* XRT data and report a disappearance of the soft excess at low flux levels during 2016–2022. To investigate this discrepancy, we retrieve the 2021 January 10 XRT observation of Mrk 590 (obsid: 00095662033), which is the longest-duration (10 ks) XRT pointing occurring within a few days of a *XMM–Newton* observations. We firstly confirm that the XRT data are consistent with no soft excess by fitting our phenomenological model (Section 3.2) using XSPEC; the blackbody normalization for this model fit is consistent with zero within its 90 per cent confidence interval. Thus, we obtain the same qualitative results as Ghosh et al. (2022) when modelling the XRT data.

While it is in principle possible that the soft excess component weakened significantly between the *XMM–Newton* and XRT observations, this seems unlikely given its tight correlation with continuum flux (Fig. 3). Assuming that the soft excess strength *relative to the continuum flux* does not vary between the observations, we generate a simulated XRT spectrum based on the best-fitting phenomenological model for the third January *XMM–Newton* data. We apply a flux scaling term (CONST) to the best-fitting model, such that its integrated 2–10 keV flux is equal to that of the XRT data (measured between 2 and 10 keV using a simple power-law model). We use the XSPEC task *'fakeit'* to generate the simulated data, applying the appropriate ARF and RMF files for the XRT detector. The resulting simulated data (red lines, Fig. C1) display a significantly higher count rate below ~ 1 keV than do the observed XRT data (black crosses). The integrated count rate of the simulated spectrum between 0.3 and 1 keV is 0.11 counts keV^{-1} s^{-1}, while the XRT observation displays 0.08 counts keV^{-1} s^{-1}. Based on the naive assumption of a constant soft excess contribution, it appears that the sensitivities of *XMM–Newton* and *Swift* XRT may differ by ~ 27 per cent below 1 keV. Alternatively, it is possible that the 10 ks XRT observation was too short to detect the soft excess at this flux level, and the offsets we are seeing are purely due to statistical fluctuations. We cannot make any definitive conclusions regarding instrumental sensitivity based on a single comparison spectrum, especially as the observations are not fully contemporaneous. However, we note that Hagen & Done (2023) report a similar ∼30 per cent deficit of X-ray counts below 1 keV for XRT observations of the AGN Fairall 9, compared to their *XMM–Newton pn* spectra; see their Appendix D for details.

Given this significant count-rate offset, our results regarding the soft excess in Mrk 590 will depend strongly on whether we base our work on *XMM–Newton* or *Swift* XRT data. We choose to rely on *XMM–Newton* for our spectral modelling in this work, due to its higher sensitivity, the longer exposure times of the available *XMM–Newton* observations of Mrk 590, and that *XMM–Newton* is more commonly used for soft X-ray excess studies.

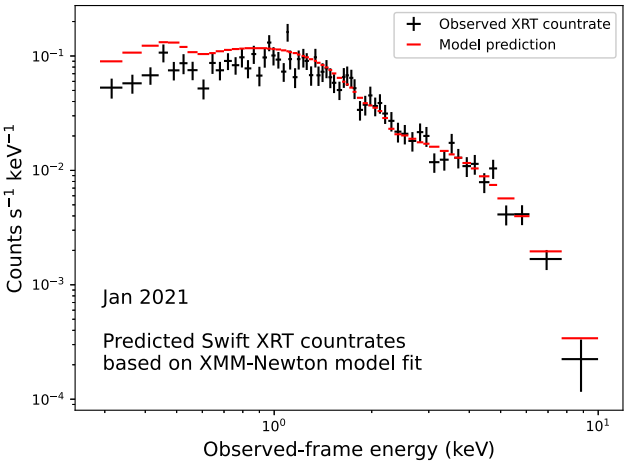

Figure C1. The predicted *Swift* XRT count rates (red lines), based on folding the best-fitting phenomenological model (Section 3.2 for the third January 2021 *XMM–Newton* observation with the XRT instrumental response, is significantly higher in soft X-rays than the observed XRT data (black crosses; 2021 January 10). The predicted data are rescaled in flux to match the 2–10 keV flux level measured by XRT. Thus, either the source spectral index varied significantly between 2021 January 3 and 10, or XRT was less sensitive to soft X-rays than *XMM–Newton* during these observations.

APPENDIX D: ALTERNATIVE CONFIGURATIONS OF THE THREE-COMPONENT AGNSED MODEL

Extending our preferred interpretation of the X-ray data (i.e. a substantial contribution from warm Comptonized emission) into the UV–optical regime, we find a reasonable overall match to the observed *Swift* photometry using the AGNSED (Kubota & Done 2018) model with no thermal emission from an outer 'thin disc' (Section 4.2). We also find a large inner truncation for the warm Comptonizing region, with $R_{\rm hot} \sim 100\, r_g$. In this Appendix, we present modelling results for alternative configurations of the AGNSED model, which support our choice of the variant with no outer 'thin disc' for the main analysis. We test four variants: (1) a model with an upper parameter bound $R_{\rm WARM} < 10^3\, r_g$ such that at least some outer disc is present, (2) a model with $R_{\rm hot} \equiv 10\, r_g$ (i.e. a compact X-ray continuum source), (3) a model where no warm-Comptonized emission is present, and (4) a model with the hot corona temperature $kT_{e,\rm hot} = 50$ keV, with a corresponding reduction in the energy emitted as hard X-rays. We show model fits of these variants, for each joint data set, in Figs D2 through D4.

The thin-disc contribution appears negligible. While the 'hybrid' (i.e. $R_{\rm warm} < 10^3\, r_g$) variant produces a reasonable match to the UV photometry, it typically does so by pegging $R_{\rm WARM}$ at its upper limit, such that the outer disc emission is minimized. For the LF data set, AGNSED cannot fully account for the observed UV–optical emission, as discussed in Section 4.2. It appears too bright to be solely due to the Comptonized flux component, and too blue to be attributed to a truncated outer disc. We defer further investigation of this issue to future work, as additional spectroscopic data will help distinguish between broadband SED models, and provide additional constraints on the all-important host galaxy stellar contribution. For the HF data set (Fig. D2, top left), even the small contribution from the outer disc with $R_{\rm WARM} = 10^3\, r_g$ overestimates the flux in the optical bands.

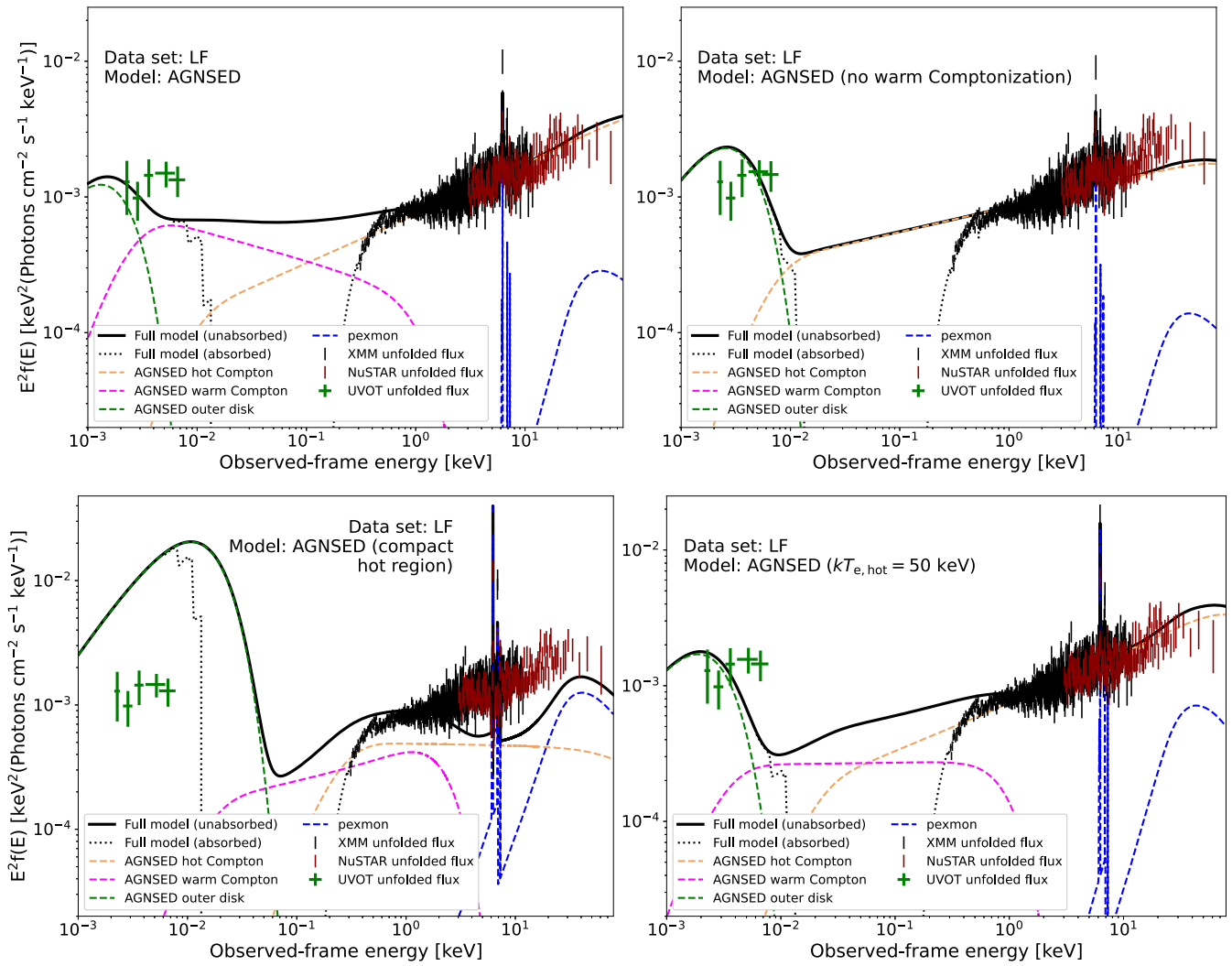

Figure D1. Alternative AGNSED + PEXMON model configurations for the LF data set. Here, we include the median-combined and host galaxy starlight-subtracted UVOT photometry; see text of Section 4.2 for details. We display the unfolded *Swift* UVOT, *XMM–Newton pn*, and *NuSTAR* FPMA spectra; data from *XMM–Newton* MOS and *NuSTAR* FPMB are included in the modelling but not shown. *Top left:* We include both an outer disc, warm Comptonization region, and hot Comptonization region, requiring only that $R_{warm} < 10^3\ r_g$. *Top right:* Here, we apply a two-component AGNSED model, with no warm Comptonization region. *Bottom left:* Here, we constrain the hot Comptonization region to a compact size, with $R_{hot} \equiv 10 r_g$. This yields a very poor fit even to the X-ray spectra, due to the trade-off between matching the UV and the X-ray flux levels while diverting only a small fraction of the accretion energy into the hot corona. *Bottom right:* Here, we set the hot region of AGNSED to an electron temperature of 50 keV, as opposed to 300 keV in the other cases. We note that the LF UV-optical data are not satisfactorily modelled by any AGNSED variant; however, the UV flux level is high enough to allow a strong contribution from the warm-Comptonized emission component identified in our X-ray modelling.

Removing the cool outer disc entirely provides a better match to observations.

Models without warm-Comptonized emission predict a too-red UV–optical slope. While the 'no warm-Comptonized emission' model can very roughly match the overall UV-optical brightness, it fails to predict the shape of the optical–UV spectral slope (Figs D2 through D4, top right panels). This can, in a sense, be attributed to the requirement of energetic consistency in AGNSED, as follows. Firstly, R_{hot} must be large, in order to produce sufficient X-ray continuum emission to match the data. Then, due to the large R_{hot}, the inner edge of any 'thin disc' is distant from the central black hole; it is therefore cooler than a non-truncated disc, for a given black hole mass. The intrinsically cool disc emission must therefore be reprocessed by a warm Comptonization region to produce a sufficiently blue continuum to match our observations.

Compact-corona variants produce insufficient X-rays at a given UV flux level. The $R_{hot} \equiv 10\ r_g$ variant significantly over-predicts the optical–UV flux levels, resulting in obviously poor model fits (Figs D2 through D4, bottom left panels). In practice, this is due to the X-ray data having more 'weight' in our modelling procedure: because we have very deep X-ray observations, a better fit statistic is obtained by matching the X-ray flux at the expense of the UV, rather than vice versa. A more physically meaningful inference is that, if the accretion energy really is dissipated according to the thin-disc prescription as a function of radius (as assumed by AGNSED), the

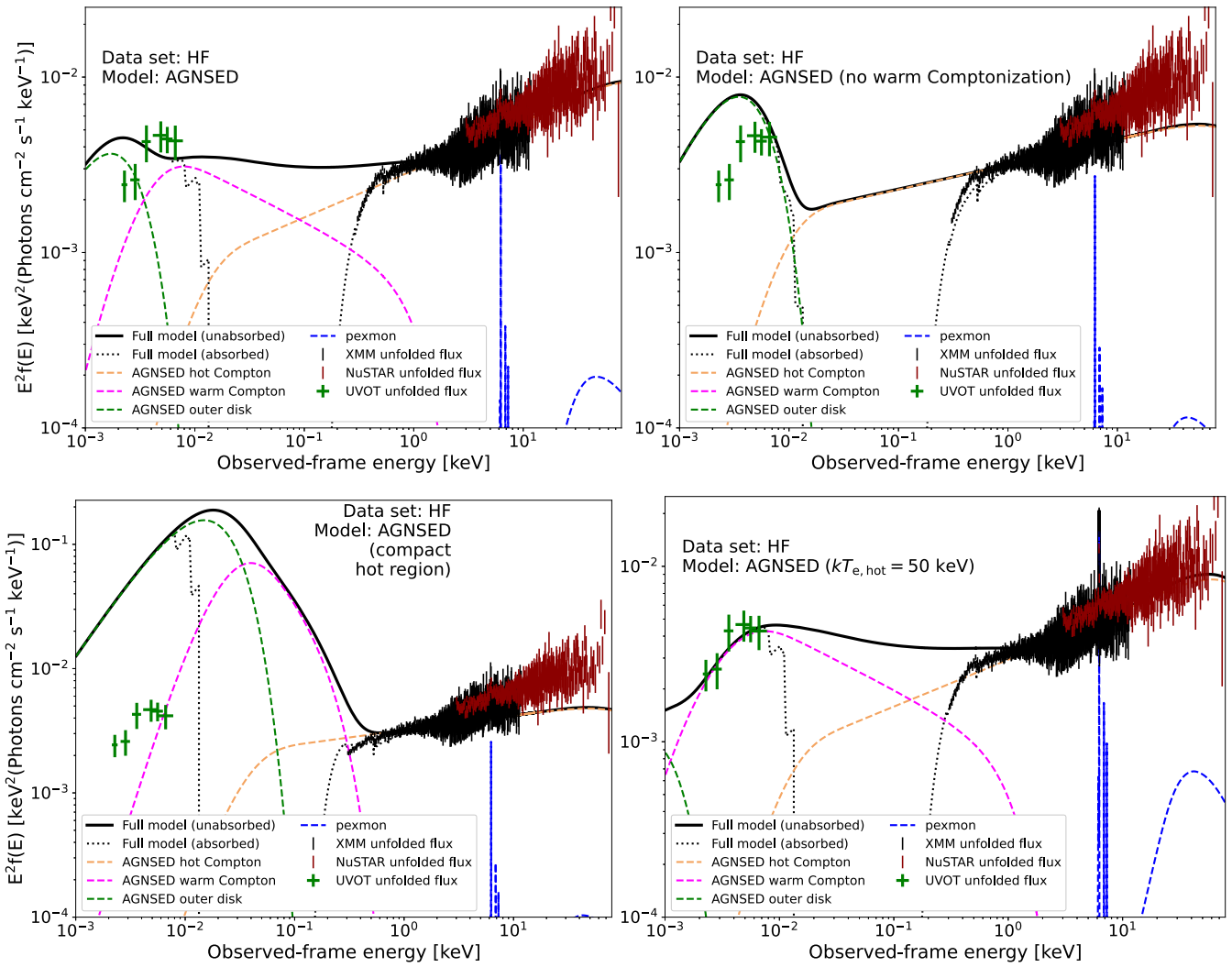

Figure D2. Alternative AGNSED + PEXMON model configurations for the HF data set. The model variants are defined as in Fig. D1. For the model variant with $kT_{e,\mathrm{hot}} = 50$ keV, the cool outer disc component is minimized in the fit, yielding very similar overall results to the 'no cool disc' model presented in the main text (Section 4.2). We note that the 'Full Model' spectra in these figures (black curves) are normalized relative to the *XMM–Newton* spectrum. Because the *NuSTAR* combined spectrum in the HF data set has a ~ 20 per cent higher overall flux level compared to the *XMM–Newton* spectrum, an offset is visible between *NuSTAR* and *XMM–Newton*. As discussed in Section 3.3, we account for flux offsets via multiplicative scaling constants in our modelling.

corona must have a much larger radius, $R_{\mathrm{hot}} \sim 100\ r_g$, to produce the observed UV to X-ray slope.

Lowering the hot coronal temperature does not significantly alter the energy budget. By reducing the temperature of the hot corona such that the high-energy cut-off is lowered, we can reduce the amount of energy emitted as X-ray continuum, for a given 10 keV brightness. As AGNSED is an energy-conserving model, this corresponds to a smaller fraction of the overall accretion energy being deposited in the corona. In the context of the assumed AGNSED geometry, this should lead to a smaller R_{hot} at lower coronal temperatures $kT_{e,\mathrm{hot}}$. To test to what degree this would affect our qualitative results, we fit an AGNSED model with $kT_{e,\mathrm{hot}} \equiv 50$ keV. We choose this value as the high-energy cut-off in the X-ray spectra is in all cases 150 keV or higher (Section 3.3.4); the high-energy cut-off is thought to be roughly 2–3 times the Comptonization temperature (Życki et al. 1999), thus 50 keV is the lowest temperature warranted by our *NuSTAR* data. Inspection of the best-fitting models with $kT_{e,\mathrm{hot}} \equiv 50$ keV reveals that the overall picture is unchanged: the warm-Comptonized emission is the dominant contribution to the UV. We find that the best-fitting R_{hot} values are indeed ~ 20 per cent smaller for these models. However, they are still of order 100 r_g, and the difference is not highly significant given the substantial uncertainties on R_{hot} for the best-fitting AGNSED models. Neither do we see significantly reduced R_{warm} values, despite the reduction in R_{hot}. We conclude that this effect is too subtle to accurately measure for the data presented in this work, and that it does not affect our qualitative result that the UV spectral energy distribution is more consistent with warm-Comptonized emission.

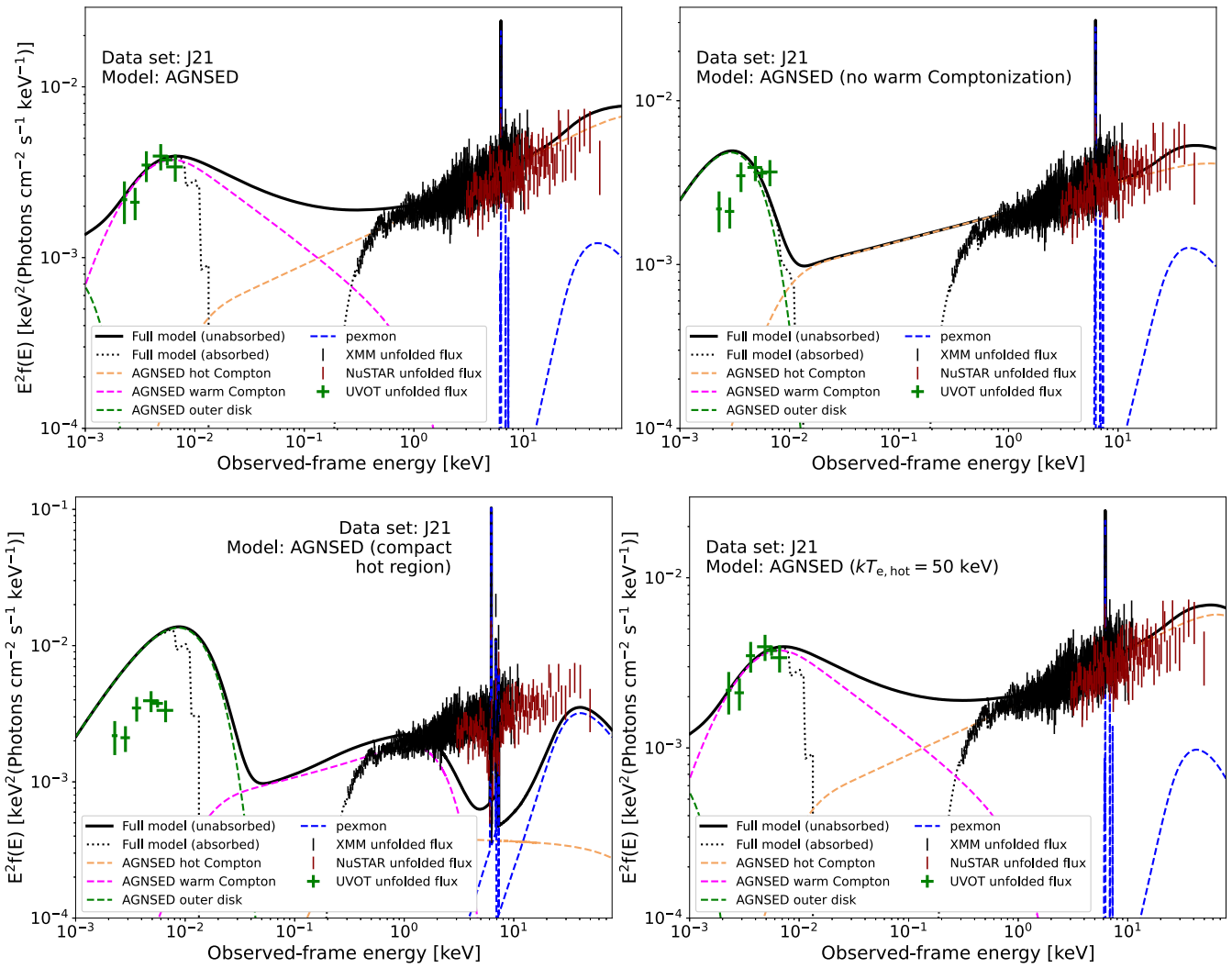

Figure D3. Alternative AGNSED + PEXMON model configurations for the J21 data set. The model variants are defined as in Fig. D1.

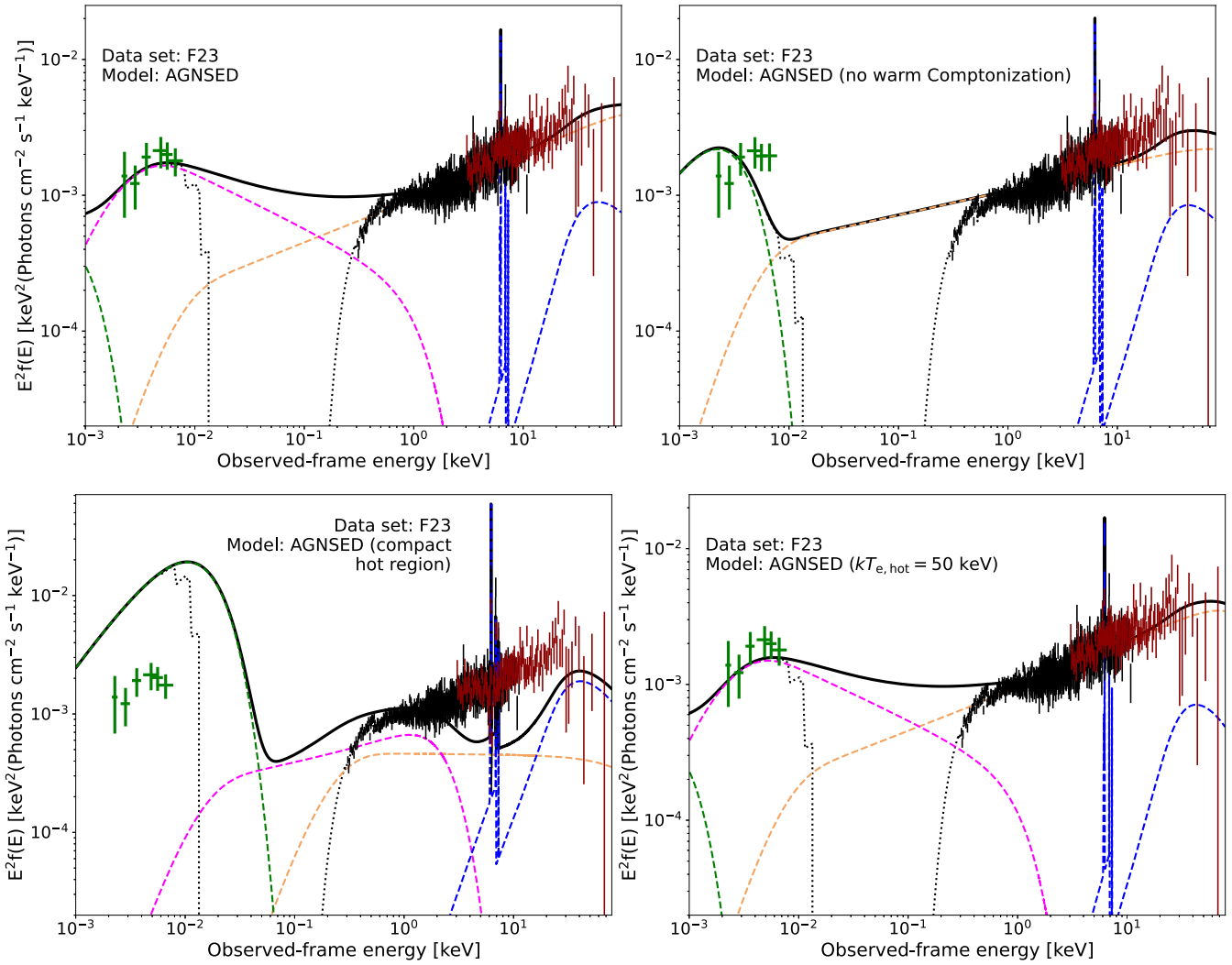

Figure D4. Alternative AGNSED + PEXMON model configurations for the F23 data set. The model variants are defined as in Fig. D1.

This paper has been typeset from a TEX/LATEX file prepared by the author.